VŠB – Technical University of Ostrava
Faculty of Electrical Engineering and Computer Science
Department of Telecommunications

Měření vybraných parametrů optických svazků pro atmosférické optické spoje

Measurement of Optical Beams Selected Parameters for Atmospheric Optical Links

2013 **Bc. Tomáš David**

VŠB - Technical University of Ostrava
Faculty of Electrical Engineering and Computer Science
Department of Telecommunications

Diploma Thesis Assignment

Student: **Bc. Tomáš David**

Study Programme: N2647 Information and Communication Technology

Study Branch: 2601T013 Telecommunication Technology

Title: Měření vybraných parametrů optických svazků pro atmosférické optické spoje
Measurement of Optical Beams Selected Parameters for Atmospheric Optical Links

Description:

The task of a student will be to study the problematic of relation between atmospheric phenomena and the atmospheric optical links transmission. In the diploma work the student will be looking into the relationship between the optical beam geometry and the most appropriate parameters reflecting the influence of the atmospheric transmission environment on the transmission itself. This diploma work is associated with grant projects solved at the Department of Telecommunications and collaborations with companies from practice.

1. Describe the critical parameters of the atmospheric optical links.
2. Assemble the experimental workplace for the simulation of the effects of external atmospheric phenomena on the optical link and measurement of the optical beam geometry of atmospheric optical links.
3. Simulate the external atmospheric conditions for the atmospheric optical links with the use of software application OPTIWAVE.
4. Compare and evaluate the values obtained by influence of external atmospheric phenomena on the optical link with the simulated data.

References:

[1] SALEH, B. E. A. *Základy fotoniky*. Praha: Matfyzpress, 1995. ISBN 80-85863-00-6
[2] WILFERT, O., KOLKA, Z. *Statistical model of free-space optical data link* . In: Proc. of The International Symposium on Optical Science and Technology. Conference 5550. Denver: SPIE. 2004, p. 203-213.
[3] KOMRSKA, J. *Vlnová optika. Část Difrakce světla. Vlnová optika. Část Difrakce světla*. Brno: CERM, s.r.o. Brno, 2004. s. 1-160. ISBN: 80-214-2822- 8.
[4] SVĚTLÍK, J. Simple Methods for the Measurement of Laser Beam Parameters. *Applied Optics*. June 1974, vol. 13, no. 6, p. 1276 - 1278.
[5] WILFERT, O. *Optoelektronika*. Elektronické skriptum. Brno: FEKT VUT v Brně, 2008.
[6] ANDREWS, L., PHILLIPS, R., HOPEN, C. *Laser Beam Scintillation with Applications.* Washington: SPIE Press, 2001.
[7] SHIRAI, T.; DOGARIU, A.; WOLF, E. *Directionality of some model beams propagating in atmospheric turbulence.* Optics Letters, 2003, Vol. 28, No. 8, pp. 610-612. ISSN 0146-9592.
[8]HENNIGER, H.; WILFERT, O. *An Introduction to Free-space Optical Communications.* Radioengineering. 2011, Vol. 19, No. 2, pp. 203-212. ISSN 1210-2512.
[9] ANDREWS, L., C.; PHILLIPS, R., L.; HOPEN, C., Y.; ALHABASH, M., A. *Theory of optical scintillation.* Journal of the Optical Society of America A. 1999, Vol. 16, No. 6, p. 1417 – 1429. ISSN

0740-3232.
[10] RICKLIN, J., C.; DAVIDSON, F., M. *Atmospheric turbulence effects on a partially coherent Gaussian beam: Implications for free-space laser communication.* Journal of the Optical Society of America A: Optics and Image Science, and Vision, 2002, Vol. 19, No 9, pp. 1794-1802. ISSN 1084-7529.

Extent and terms of a thesis are specified in directions for its elaboration that are opened to the public on the web sites of the faculty.

Supervisor: **Ing. Jan Látal**

Date of issue: 16.11.2012

Date of submission: 07.05.2013

prof. RNDr. Vladimír Vašinek, CSc.
Head of Department

prof. RNDr. Václav Snášel, CSc.
Dean of Faculty

Declaration Made by the Student

I hereby declare that this master's thesis was written by myself. I have quoted all the references I have drawn upon.

On *1.5.2013*

……

Student signature

Acknowledgment

At this point I would like to thank especially to my thesis supervisor MSc. Jan Látal for all his help and support during the development of this work. I would like to thank also for his professional approach and the time he devoted to my work. Also I would like to thank to prof. Dr. Vladimír Vašinek and MSc. Jan Vitásek for their valuable advices. Furthermore I would like to thank to my sister Věra Davidová, my brother Josef David and Martina Tionová for help with proofreading of this work. I would to thank to my parents and Denisa Minářová for all their support.

Abstrakt

Tato diplomová práce pojednává o problematice bezvláknových optických spojů. Teoretická část práce obsahuje rozbor klíčových parametrů těchto spojů a popisuje atmosférické vlivy přenosového prostředí na tyto spoje. Praktická část práce je zaměřena zejména na vytvoření vhodného experimentálního pracoviště pro simulování atmosférických vlivů a následné měření těchto vlivů. To zahrnovalo také návrh simulačního boxu pro vytvoření atmosférických vlivů. Simulační část práce byla zaměřena na softwarovou simulaci atmosférických vlivů naměřených v měřicí části práce. Vyhodnocení nejdůležitějších výsledků je uvedeno v závěru práce.

Klíčová slova

Atmosférický optický spoj, přenosové prostředí, extinkce, fluktuace, turbulence, mlha, simulační box, měření, útlum, regrese, simulace.

Abstract

This thesis deals with problematic of free space optics links. The theoretical part contains an analysis of key parameters and describes the effects of atmospheric transmission environment for these connections. The practical part is focused on the creation of an appropriate experimental workplace for simulating atmospheric effects and subsequent measurement of these effects. This included designing of simulation box for simulating atmospheric environment. Simulation part of the thesis was focused on software simulations of atmospheric effects measured in the measuring part. Evaluation of the most important results is contained in the conclusion.

Key Words

Atmospheric optical link, transmission environment, extinction, fluctuations, turbulence, fog, simulation box, measurement, attenuation, regression, simulation

Contents

1 Introduction

Information and communication became more and more important these days. We have been constantly developing and improving technologies to have faster, safer and more reliable way of data transmission. One of many technologies used for data transmission is optical fiber communication where optical fiber is used as medium. Optical fiber technologies are widely used for its speed, low attenuation and reachable distance. Due to these characteristics, optical fiber technologies are widespread in backbone networks around the world.

This diploma thesis deals with less expanded technology - free space optics (FSO). The principle is very similar to optical communications throughout fiber but the transmission medium is an atmospheric environment. There are some advantages and disadvantages compared to fiber links. Free space optical communication is considered to be one of the key technologies in the aerospace communications. The wireless aspect of free space optics has cardinal advantage in small networks (for example in cities) where laying of fiber optic cables is complicated and expensive. Application of FSO is not limited only between buildings near the ground. FSO is also represented in the communication in space. This diploma thesis deals with problematic of communication using free space optics in various atmospheric conditions.

First part of thesis contains basic description of an optical link without fiber, including theoretical description of critical parameters, affecting the quality of FSO links. Various possibilities of FSO link design (optical sources, detectors, modulation types etc.) are discussed. This part mainly focuses on the theoretical description of the factors affecting FSO link as a fluctuations or extinctions of optical power.

Second part of this thesis has been focused on the measuring of critical parameters mentioned in the first part. That includes assembling of experimental workplace for simulation of the effects of external atmospherical phenomena. A special box for measuring had to be created, which allows simulating external conditions, such as fog or turbulences. Also measuring applications created in the previous work of the author has been improved for better measurement stability, automation and for faster measuring. After assembling of the experimental workplace, measurements of laser optical beam influenced by atmospheric conditions were made. The resulting data were appropriately processed by the software applications.

Next part of thesis is about simulation in software environment Optiwave OptiSystem 11. In this software, simulation conditions that were measured in second part were simulated. Thanks to this, assumptions obtained by measurement were verified. In conclusion, all achieved results are evaluated. Results of the thesis allows better understanding of the optical beam affected by atmospheric conditions.

2 Composition of FSO Link

In a simplified way, FSO provides communication between two points using optical signal. Broadcasted data are modulated on the frequency, intensity or phase. In practice, we can found two variants of FSO link. The conventional FSO link (in Figure 2.1) is composed of two optical heads, which both operate in duplex mode and information can be exchanged simultaneously between heads in both directions. That means transmitter is also a receiver at the same time.

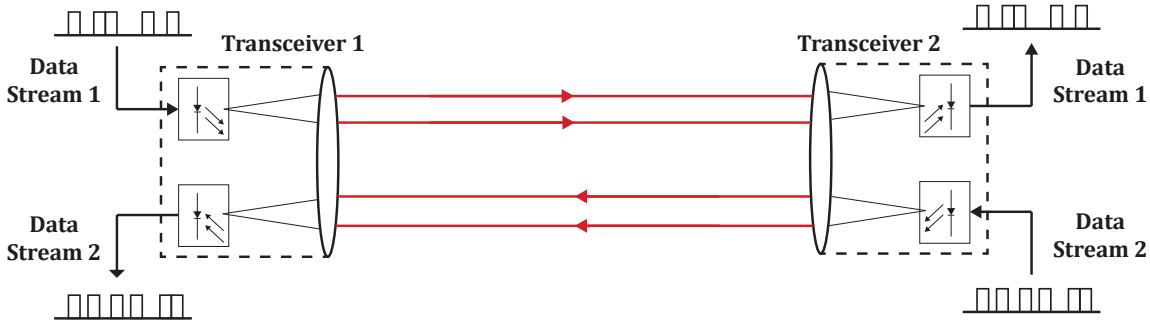

Figure 2.1: Conventional FSO system diagram [1].

The second and less used variant of FSO link uses modulated retro-reflector (MRR). This type of link is composed of two different terminals (Figure 2.2). The interrogator produces the continuous wave (CW) and transmits it to the other side of the link. Then retro-reflector modulates the CW wave with input data stream. Modulated beam is reflected back to the interrogator. This system permits simplex communication only. This thesis will be focused on first type of FSO link - conventional FSO [1].

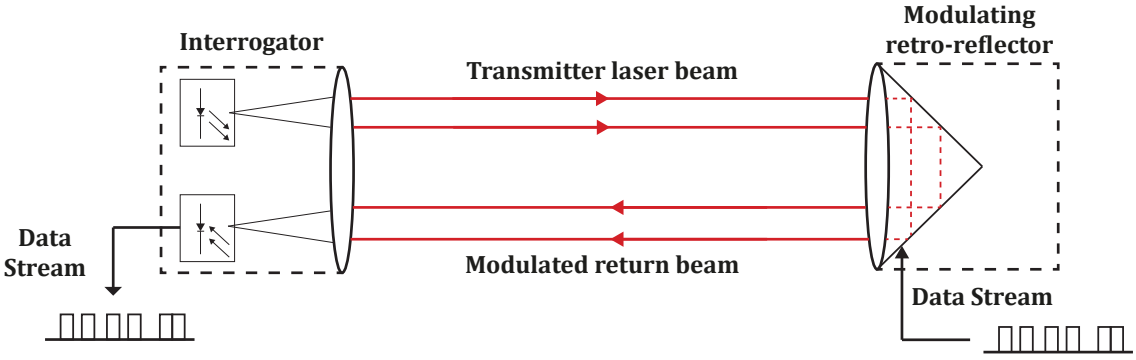

Figure 2.2: Diagram of FSO system based on modulated retro-reflector [1].

FSO heads has to be directed against each other and also in line of sight. Usually they are placed in building roofs but also can be placed also in windows. Between optical heads, there is a transmission medium (air, fog, windows etc.), which is the most problematic part of FSO links. In FSO systems can be also used radio technologies as a backup during inappropriate weather. (in Figure 2.3)

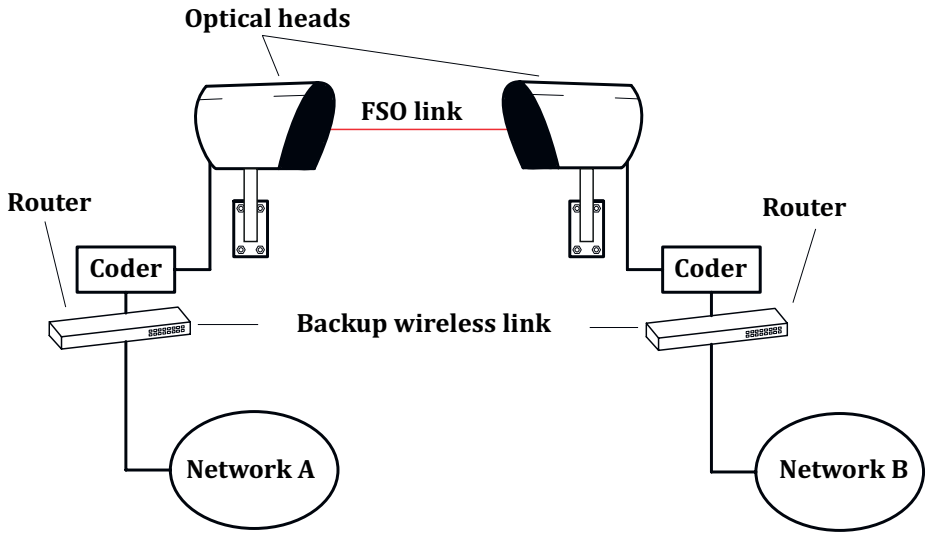

Figure 2.3: Composition of free space optics link.

2.1 Advantages of FSO

FSO has many advantages compared with some other technologies, including:

- High data rate (currently up to 10 Gbit·s^{-1}).
- Easy and quick installation comparing to optical fiber link.
- Narrow beam size.
- Human health safety.
- Using of unlicensed spectrum.
- Relatively cheap.
- Independent of modulation and protocol formats.

2.2 Disadvantages of FSO

Main disadvantages of FSO are:

- Dependence on weather – fog, rain, clouds, storms, snow, wind, etc.
- Other adverse effects – atmospheric turbulence, fluctuations, scintillation, over flights of birds.
- Small transmission distance (up to 6 km) compared to fiber optics links.
- Need for direct line of sight between connected optical heads.

3 Optical Head for FSO Link

This chapter focuses on FSO head and main parts will be analyzed. In Figure 3.1 we can see an example of the optical head using optics only (without electric media convertor).

FSO heads can be divided into two groups:

- Where the received optical signal has to be transferred into the electric signal.
- Where the received optical signal is used as it is and we do not have to transfer it.

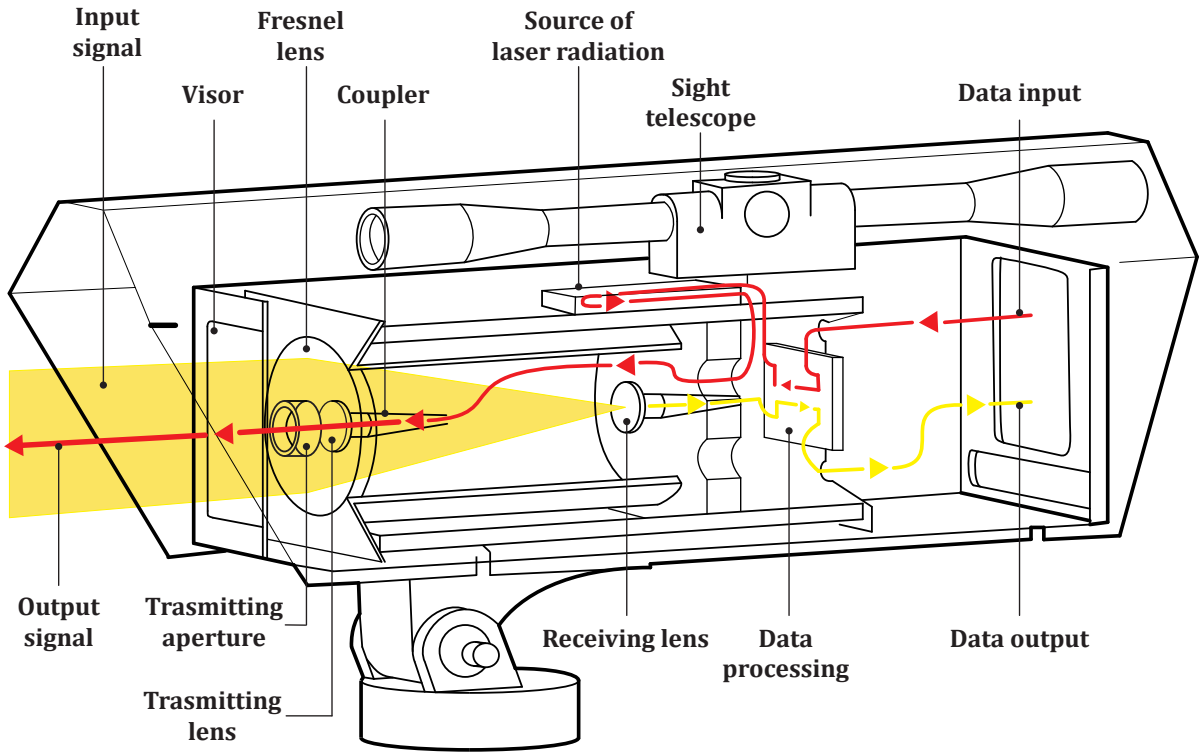

Figure 3.1: Cross-section of optical head [4].

Signal transmits through optical or metallic interface to the optical head. After that, signal is being processed (from optical to electrical or vice versa) or sent directly to the modulator, where is appropriately modulated. Multiple sources of radiation (usually 2-3) are used in modern heads. Because of this, we are using component called Coupler that is able to split signal traveling in one fiber into the multiple fibers. Then optical beam is radiated through the lens and cover glass out from the head.

For initial alignment of direction, telescope is usually part of head. The final focus is done by sight system. For perfect functionality both heads have to be precisely facing each other.

The receiving part of the head receives beam coming from the other side of the link. Input signal goes through the lens (eg. Fresnel) centered to the radiation detector where it is being processed. Signal is usually transferred to an electrical signal and demodulated.

3.1 Radiation Sources

Source of radiation is used to convert electrical signal to optical signal (as we need it for transmitting). LED or laser diode (LD) are used as a source of radiation. It is necessary to choose a suitable source to correspond with link distance. Laser diodes are primarily used for longer distance because of very high divergence of LED sources. In addition to low divergence, laser diode has advantages in more narrow spectral characteristics (in Figure 3.2), greater performance, and modulation speed. Diode can be used at a frequency of 1 GHz or more, compared to the LED sources at frequencies of about 100 – 300 MHz only. The most common wavelengths used in the FSO links are 850 nm and 1550 nm where transmission windows are located.

First working laser (an acronym standing for Light Amplification by Stimulated Emission of Radiation) was introduced in 1960. The base of the laser function is process of stimulated emission. For proper functionality of laser, 4 conditions have to be complied - mentioned stimulated emission, inversion of population, power supply and positive feedback by resonator.

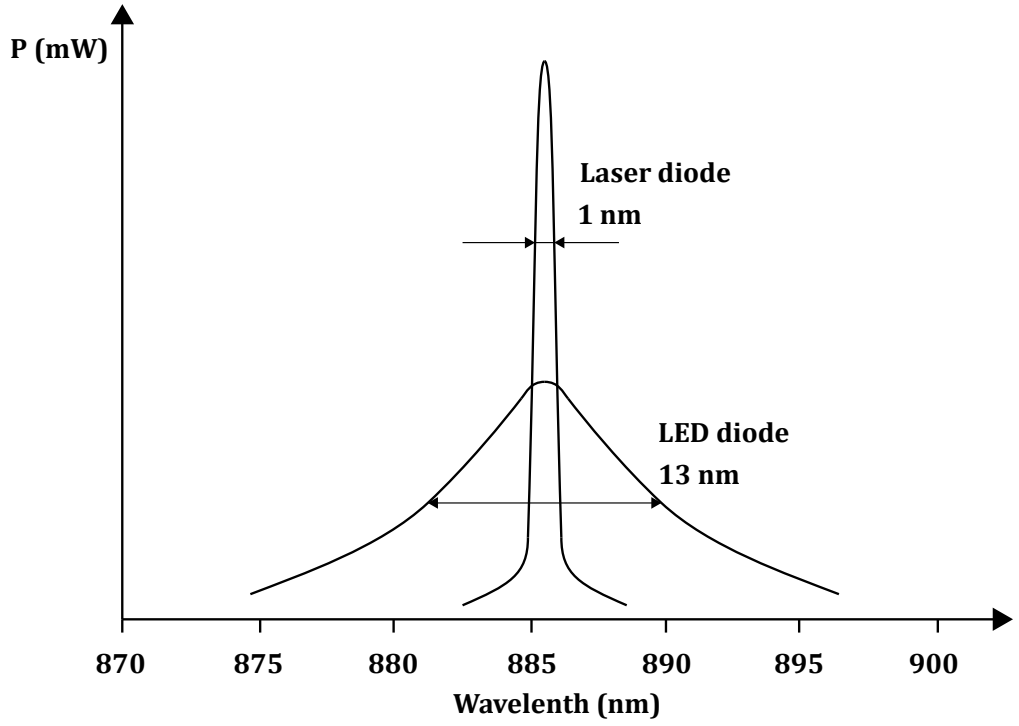

Figure 3.2: Spectral characteristics of sources for FSO links.

3.1.1 Types of modulation

The choice of modulation technique should be in balance between power efficiency, simplicity and bandwidth efficiency. Dominant type of modulation in FSO is OOK (on/off keying), because of simplicity of its implementation. With NRZ variant of OOK is signal transmitted when keying signal is exactly 1, which is very easily implemented, and no synchronization is needed. But performance of this type with the fixed threshold level OOK is not optimal. OOK modulation is most widely used for terrestrial FSO links at this time [1].

PPM (Pulse Position Modulation) uses the same width and amplitude of pulse. Modulation is formed by time shift from a basic time position. Principle of PPM and difference from OOK is shown in Figure 3.3. The main advantage is the superior energy efficiency in comparison to OOK. The low crest factor (peak-to-average) power requirement makes PPM most widely used modulation for optical communication in the deep space. The biggest disadvantage of this type of modulation is that this modulation needs perfect synchronization of clock between transmitter and receiver. Another disadvantage is low bandwidth and tighter slot, which makes this modulation not very usable in commercial terrestrial FSO systems at this moment [1], [11].

Another type of modulation used in FSO is subcarrier intensity modulation (SIM) based on BPSK modulation. This modulation can offer high throughput but has a disadvantage in complex of implementation compared to OOK modulation [18].

Detailed comparison of modulation used in FSO can be found in Table 3.1.

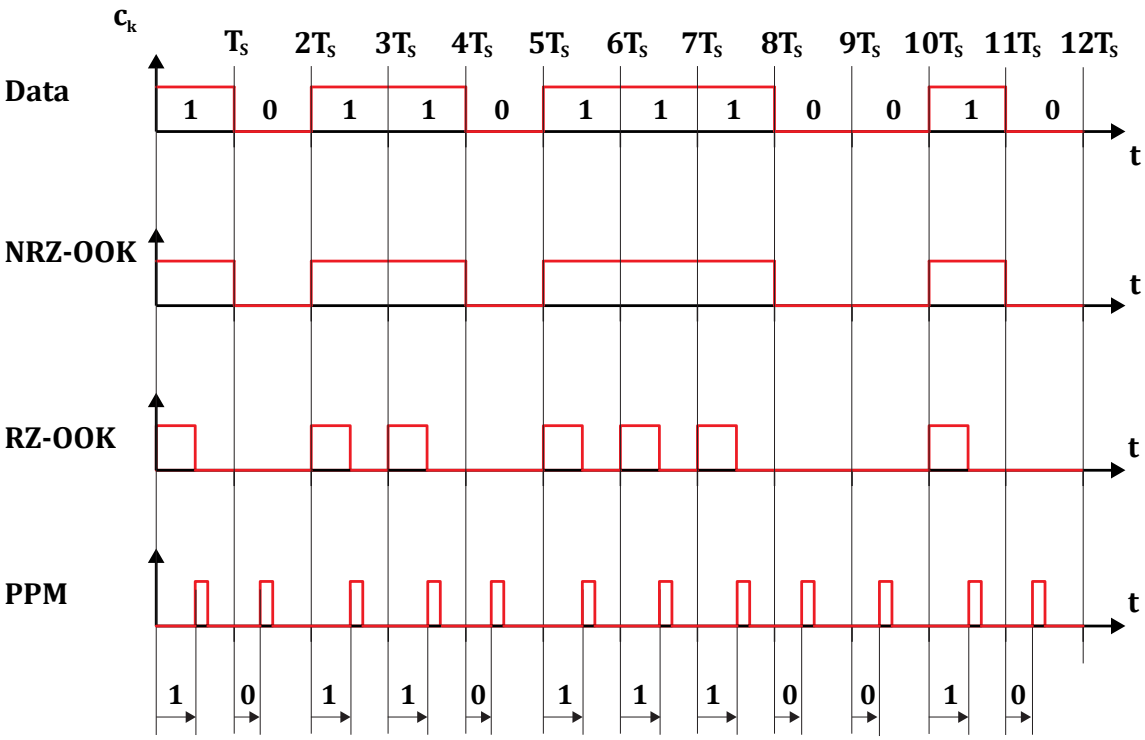

Figure 3.3: Types of modulation for FSO links [1], [11].

Table 3.1: Comparison of FSO modulation techniques [1].

On-Off Keying	**Pulse Position Modulation**	**Subcarrier Intensity Modulation**
Simple to implement	Power efficient	Power inefficient
Synchronization not required	Synchronization required	Higher throughput
Adaptive threshold required in fading channels	Adaptive threshold not required in fading channels	Adaptive threshold not required in fading channels
Component nonlinearity not an issue	Component nonlinearity not an issue	Component nonlinearity an issue with multiple subcarrier
Suboptimal with fixed threshold	High bandwidth requirement	Benefits from advances in digital signal processing and matured RF components

3.2 Photo detectors

After beam transmission, receiver must process this beam of light - convert optical signal to an electric signal. Received light beam is directed to the lens, which focuses it to the small area of the detector. Detectors are almost without exception made with PN junction technology. The most types of detectors used are PIN and APD (Avalanche Photodiode). Detector of an optical signal is very important element of FSO link that determines the efficiency of the entire system. The material of choice for the photodiodes depends on the wavelength at which they will be operated. For use in short-wavelength area around 850 nm, GaAs material perfectly fits. The longer-wavelength systems at 1550 nm require different photo detectors. These are typically composed of lattice-matched ternary InGaAs material. Germanium only detectors are generally not used in FSO links because of their dark current. Detailed overview of materials used for detectors can be found in Table 3.2. To calculate the wavelength upper limit of photodiode, following formula can be used [1], [5]:

$$\lambda_c = \frac{h \cdot c}{E_g} = \frac{1.24}{E_g} \quad , \quad (\mu m) \tag{3.1}$$

where λ_c is wavelength in (μm), E_g is the energy band-gap of the semiconductor material in (eV), h is Planck constant and c is speed of light in vacuum.

Table 3.2: Comparison of photodetector materials [1].

Material	Energy Gap (eV)	Cut-Off λ (nm)	λ Range (nm)
Silicon	1,17	1060	400 - 1060
Germanium	0,775	1600	600 - 1600
GaAs	1,424	870	650 - 870
InGaAs	0,73	1700	900 - 1700
InGaAsP	0,75 - 1,35	1650 - 920	800 - 1650

PIN photodiode works on the principle of conventional PN diodes but between heavily doped P and N layers there is intrinsic region inserted. Because of high resistance of intrinsic region, diode can achieve electric field with high intensity. Due to this property is PIN diode is often used for high-speed applications. Reaction speed to light changes is very fast and moves in order of ns to μs.

Table 3.3: Comparison of photodetector types [1].

Material/Structure	Wavelength (nm)	Responsivity	Typical Sensitivity	Gain
Si PIN	300 - 1100	0,5	-34 dBm @ 155 Mbps	1
Si PIN, transimpedance amplifier	300 - 1100	0,5	-26 dBm @ 1,25 Gbps	1
InGaAs PIN	1000 - 1700	0,9	-46 dBm @ 155 Mbps	1
Si APD	400 - 1000	77	-52 dBm @ 155 Mbps	150
InGaAs APD	1000 - 1700	9	-33 dBm @ 1,25 Gbps	10

The second type of photodiode used as a detector of radiation in FSO link is APD diode. It is used especially for longer distance, because photo in PIN diode generates single electron-hole pair, which is not suitable for applications with low intensity of radiation. The principle of APD is the process of impact ionization (avalanche effect) by applying high reverse voltage (typically 100-200 V in silicon), which generates strong magnetic field. Due to this field, single pulled electron can pull other electrons with avalanche effect. These electrons form another electron-hole pairs. This process is called photo-multiplication and can be expressed as a numerical coefficient of quantum efficiency. The basic assumption of APD is that quantum efficiency η is greater than 1. Typical gain values lie in the range 50 to 300, and this value is proportional of the reverse voltage. The main disadvantages of APDs are higher price and temperature-sensitivity of avalanche process. The differences in the parameters of the PIN and APD photodiodes are also evident from the Table 3.3 [1].

4 Shapes of Optical Beam

Sources of light radiation can significantly differ in the shape of emitted beam. These shapes can be divided into the most common types that are described in this chapter.

4.1 Gaussian Beam

Describe of Gaussian beam is the most important because this type of beam outputs from diode frequently. The distribution of intensity of Gaussian beam in transverse plane corresponds to a circularly symmetric Gaussian function where optical axis is also an axis of symmetry. Power in Gaussian beam is concentrated in a narrow cone. Minimum beam width is in part called neck and it increases in both directions as shown in Figure 4.1. Gaussian beam radius *w(z)* can be calculated using this relation:

$$w(z) = w_0 \sqrt{1 + \left(\frac{z}{z_0}\right)^2} \quad , \quad \text{(m)} \tag{4.1}$$

where w_0 is the half-width of beam at narrowest point, z is a coordination of the optical axis, z_0 is Rayleigh distance. This Rayleigh distance can be described as the distance of the longitudinal direction of propagation from the neck to the point where the transverse cross-sectional area is doubled. In other words the distance from which the beams do not propagate parallel but diverge (the plane wave becomes radial). It can be expressed by the formula [12]:

$$z_0 = \frac{\pi \cdot w_0^2}{\lambda} \quad , \quad \text{(m)} \tag{4.2}$$

where λ is wavelength of used source of light. The angle of divergence θ can be expressed as:

$$\theta = \frac{\lambda}{\pi \cdot w_0} \quad , \quad (^\circ) \tag{4.3}$$

Curvature radius of the wavefront *R(z)* is equal to:

$$R(z) = z\left[1 + \left(\frac{z_0}{z}\right)^2\right] . \quad (^\circ) \tag{4.4}$$

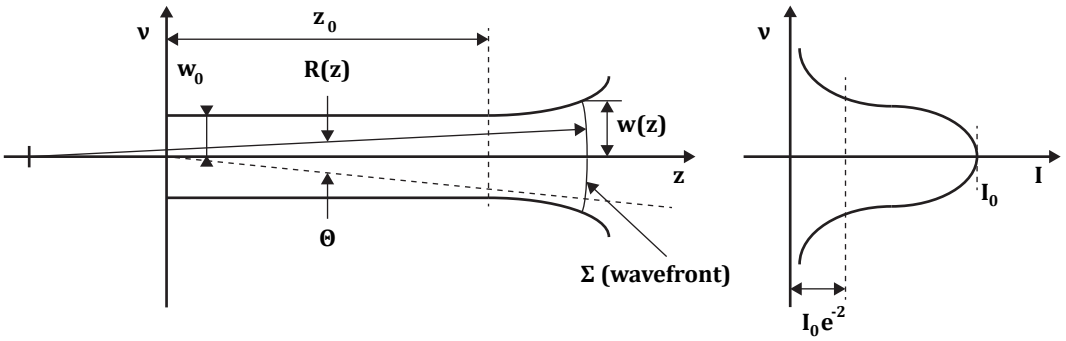

Figure 4.1: Profile of Gaussian beam [12].

4.1.1 Optical intensity of Gaussian beam

The intensity of the optical radiation is a axial (going in the direction of the axis) function of distance z and radial (going in the direction of the radius) distance ρ. This radial distance ρ can be expressed as:

$$\rho = \sqrt{\left(x^2 + y^2\right)}\ , \quad \text{(m)} \tag{4.5}$$

then intensity of Gaussian beam:

$$I\left(\rho,z\right) = I_0\left(\frac{w_0}{w\left(z\right)}\right)^2 \cdot \exp\left(-\frac{2\cdot\rho^2}{w^2\left(z\right)}\right), \quad \left(\text{W}\cdot\text{m}^{-2}\right) \tag{4.6}$$

Gaussian beam intensity is greatest at the center of beam (when axial z and radial distance ρ is equal to 0). Gaussian beam radius $w(z)$ growing with increasing axial distance. Intensity of the Gaussian beam decreases with increasing axial distance z [12].

4.1.2 Optical power of Gaussian beam

The total power transmitted by beam is determined by the integral of intensity and cross-sectional area of beam:

$$P = \int_0^{\infty} I\left(\rho,z\right)\cdot 2\cdot\pi\cdot\rho\ d\rho\ , \quad \text{(W)} \tag{4.7}$$

from this, following equation can be deduced:

$$P = \frac{I_0\cdot\left(\pi\cdot w_0^2\right)}{2}\ , \quad \text{(W)} \tag{4.8}$$

optical power P is given as the product of the maximal intensity I_0 and half of circle area w_0 [12].

4.2 Top Hat Beam

Another distribution of beam is called Top Hat beam. It is characterized by almost uniform shape - its intensity does not change with increasing radial distance ρ. Top Hat beam has a "softer" profile and that leads to smaller fluctuations in optical power caused by turbulence. Main disadvantage of this type of shape is the greater density distribution of optical intensity than in the case of Gaussian "sharp" profile. To obtain Top Hat shape several methods of forming from Gaussian beam can be used:

- Aperturing.
- Field mappers.
- Beam integrators.

Aperturing is method when aperture is used to select the appropriate part of the original beam. This technique is very simple but noticeable optical power loss can occur. Second method - field mappers is based on the transformation of input field to the field by desired way. This method is very sensitive to the accuracy of setting and size of optical beam. Third method uses beam integrators and is suitable for multimode and coherent beams. Beam is processed by a set of lenses. Problem with this method can be interference effects by coherent beams [13], [14].

4.3 Edge Beam

As types of beams used in optical communications are also often used distribution of beam called edge beam. It is characterized by concentrating its intensity to the edge. This type of optical beam is for example generated by VCSEL sources. Profile of edge beam reduces spherical defect and allows easy focusing on one point. Comparison of described beam profiles can be found in Figure 4.2.

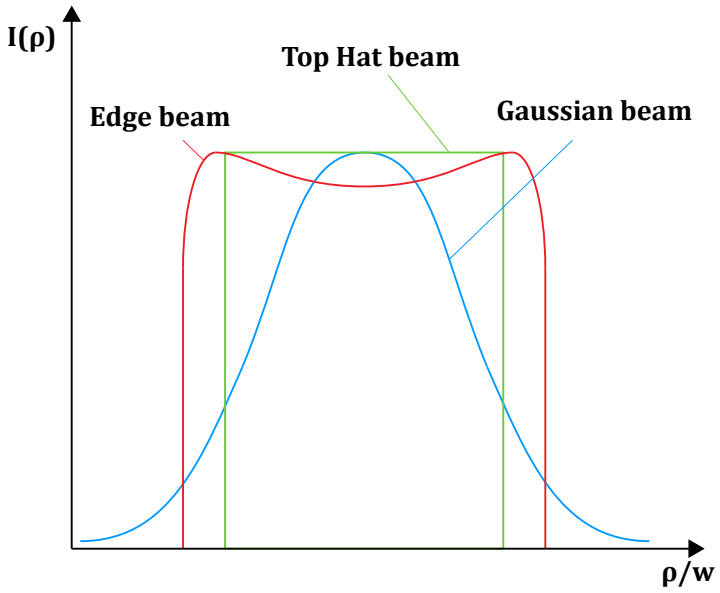

Figure 4.2: Profile of a Gaussian beam.

5 Atmospheric Environment as a Medium

Typical free space optical links work in the troposphere in areas up to about 10 km above sea level (see Figure 5.1). This altitude affects seasons, actual weather etc. In practice, we can also find connections operating at higher altitudes or in the space. This thesis deals with FSO links to communicate in troposphere, near the surface of the Earth where most connections are built.

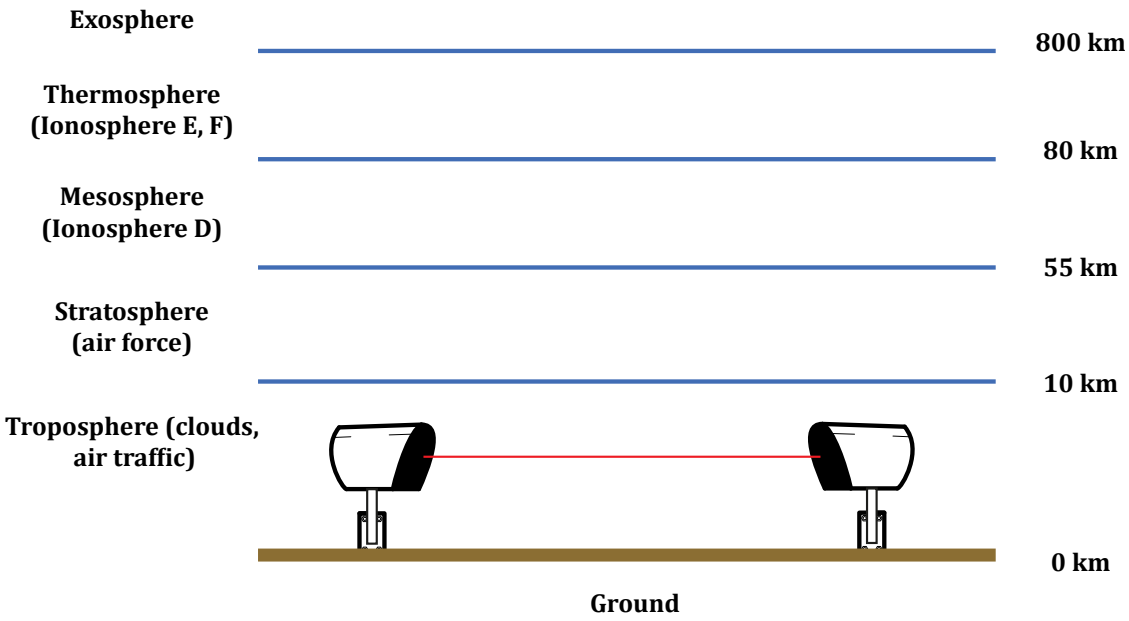

Figure 5.1: Composition of the atmosphere.

The effects of nature in troposphere highly influence optical communications. These phenomenons affect communication simultaneously but we can divide them into two primary groups - optical extinction and refractive-index fluctuations (i.e., optical turbulence). This chapter describes various influences in detail. Detailed overview of how much atmospheric influences affect optical links in terms of visibility and attenuation can be found in Table 5.1. Following subsections are focused on these influences and described in detail [2], [3].

Table 5.1: Visibility range and attenuation coefficient for various weather conditions [1].

International Visibility Code					
Weather Conditions	**Precipitation (mm/h)**			**Visibility (m)**	**Attenuation ($dB \cdot km^{-1}$)**
				0	
Dense fog				50	315
Thick fog				200	75
Moderate fog				500	28,9
Light fog	Snow			770	18,3
		Storm	100	1000	13,8
Very light fog				1900	6,9
		Strong rain	25	2000	6,6
Light mist				2800	4,6
		Average rain	12,5	4000	3,1
Very light mist		Light rain	2,5	5900	2
				10000	1,1
Clear air		Drizzle	0,25	18100	0,6
				20000	0,54
Very clear air				23000	0,47
				50000	0,19

5.1 Extinction

The optical extinction is defined as the reduction or attenuation in the amount of radiation passing through the atmosphere. Extinction can be further divided into molecular absorption and scattering. Absorption and scattering can be well simulated by quality software models developed by The Air Force Geophysical Laboratory (AFGL). In software packages like LOWTRAN, FASCODE, MODTRAN, HITRAN or PCLNWIN that are typically used, we can predict transmittance effects based on atmospheric conditions, latitude, wavelength [2], [3].

The transmittance is parameter of optical radiation that has propagated a distance L related to extinction. This follows Beer's law and can be written as

$$\tau = \exp\left[-\alpha_e(\lambda)\cdot L\right], \quad (-) \tag{5.1}$$

where $\alpha_e(\lambda)$ is the extinction coefficient. Then $\alpha_e(\lambda)L$ is called the optical depth. The mean extinction coefficient can be written as

$$\alpha_e(\lambda) = \alpha_a(\lambda) + \beta_s(\lambda) + \alpha_f(\lambda), \quad (\mathrm{dB\cdot km^{-1}}) \tag{5.2}$$

where $\alpha_a(\lambda)$ is the absorption coefficient, $\beta_s(\lambda)$ is the scattering coefficient and $\alpha_f(\lambda)$ is the parameter of mean attenuation due to fluctuations [1], [2], [8].

5.1.1 Molecular absorption

Molecular absorption occurs when a photon of radiation is absorbed by a molecule that converts molecule's kinetic energy. Hence atmosphere is heated by this mechanism. Absorption depends on the type of molecules and their concentration. Attenuation by absorption is given by imaginary part of the complex refractive index - the index of absorption $\kappa(\omega)$. Index of absorption is characteristic for specific molecule. For water the attenuation is following:

$$\kappa = \begin{cases} 2.929\cdot 10^{-7} & \lambda = 850nm \\ 1.348\cdot 10^{-4} & \lambda = 1550nm \end{cases}, \quad (-) \tag{5.3}$$

in comparison by scattering, these values are negligible. Absorption also strongly depends on wavelength and it is very selective. Because of this, we can choose from transparent zones - range of wavelength with minimal absorption (see Figure 5.2) [1], [2], [11].

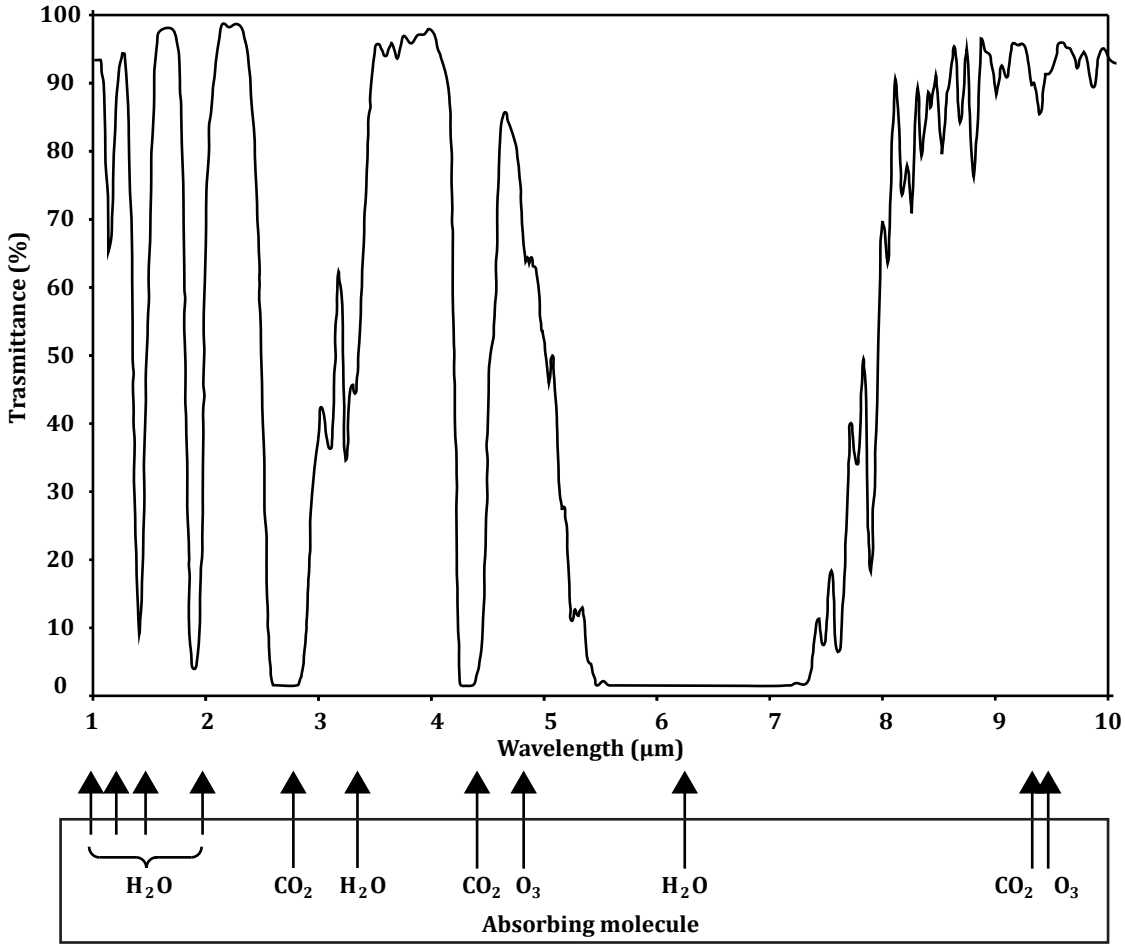

Figure 5.2: Atmospheric transmittance for 1 km horizontal path [1], [2].

5.1.2 **Scattering**

Scattering is strongly wavelength dependent effect. It occurs when radiation propagates through air molecules and particles. In comparison with the absorption, scattering is effect where there is no loss of energy only redistribution of the optical field [1], [2].

Coefficient of scattering can be written as the sum of the scattering effect:

$$\beta_s(\lambda) = \beta_m(\lambda) + \beta_a(\lambda) \ , \quad (\text{dB}\cdot\text{km}^{-1}) \tag{5.4}$$

where $\beta_m(\lambda)$ is coefficient of Rayleigh scattering and $\beta_a(\lambda)$ is coefficient of attenuation by Mie scattering. Typical types of particles affecting FSO links and the type of scattering can be found in Table 5.2.

Table 5.2: Typical scattering particles and their scattering process at 850 nm [1].

Type of Particle	Radius [μm]	Size Parameter x_0	Scattering Process
Air molecules	0,0001	0,00074	Rayleigh scattering
Haze particle	0,01 - 0,1	0,074 - 7,4	Rayleigh - Mie
Fog droplet	1 - 20	7,4 - 147,8	Mie - Geometrical
Rain	100 - 10000	740 - 74000	Geometrical
Snow	1000 - 5000	7400 - 37000	Geometrical
Hail	5000 - 50000	37000 - 370000	Geometrical

5.1.3 Rayleigh scattering

The Rayleigh scattering is also called molecular scattering. It is caused by molecules and particles much smaller than wavelength of radiation. It applies only when there is very clear atmosphere. Rayleigh scattering is given and can be written as:

$$\beta_m(\lambda) = 0.827 \cdot N_p \cdot A_p^3 \cdot \lambda^{-4} \ , \quad (\text{dB}\cdot\text{km}^{-1}) \tag{5.5}$$

where N_p is the number of particles per unit volume along the propagation path and parameter A_p is cross-sectional area of scattering. Directionality of Rayleigh scattering is shown in Figure 5.3. Well-known effect of the blue sky is caused by Rayleigh scattering [1], [2].

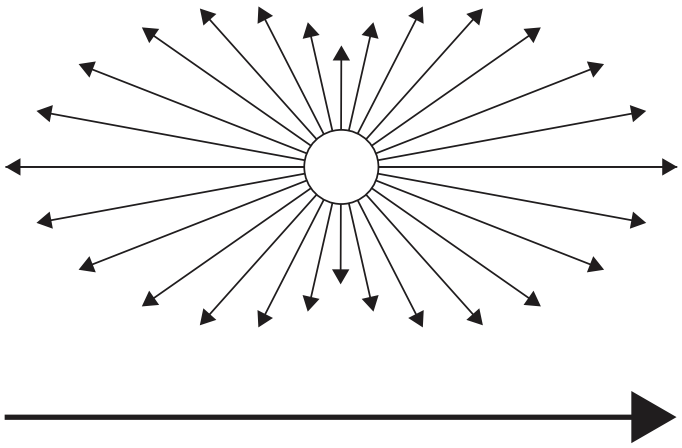

Figure 5.3: Directionality of the Rayleigh scattering.

5.1.4 Mie scattering

The Mie scattering also called aerosol scattering generates on particles comparable or greater in size with size of radiation wavelength. Unlike Rayleigh scattering Mie scattering radiation is concentrated in the forward direction (see Figure 5.4). With increasing wavelength, scattering effect rapidly losses. Fog particle size compares very much with most of FSO

wavelength (500 - 2000 nm) because of this Mie scattering is the dominant scattering process in FSO links. Mie scattering is also the reason why sunset looks red [1], [2].

Attenuation of Mie scattering can be written as:

$$\beta_a(\lambda) = 10^5 \int_0^{\infty} Q_d\left(\frac{2\cdot\pi\cdot r}{\lambda}, n'\right)\cdot\pi\cdot r^2\cdot n(r)\,dr \quad , \quad (\mathrm{km}^{-1}) \tag{5.6}$$

where r is radius of particle in cm, Q_d is efficiency of the Mie scattering, n' is real part of the complex refractive index, $n(r)$ is the volume concentration (number of fog particles per unit volume unit increment in radius) [1].

The application of Mie scattering is very complicated because particles in the atmosphere have various orientations and shapes. That is why description of attenuation due to scattering is now based on reported empirical formulas. Empirical formulas often uses parameter of visibility range V. Parameter of visibility indicates opacity of the atmosphere. Visibility defines range (in km) until transmitted power of optical beam drops to threshold τ_{TH} of the original power. Threshold τ_{TH} exists in two variants - 2% (which is used in the original Kruse equation) or 5% that is typically used today for example by airports. Visibility is typically measured at 550 nm which is at the center of human's eye sensitivity [1], [2].

We can choose Kruse formula using visibility parameter (τ_{TH} = 2%) for attenuation of Mie scattering written as:

$$\beta_a(\lambda) = \frac{3.912}{V}\cdot\left(\frac{\lambda}{550\,nm}\right)^{-q} \approx \alpha_e(\lambda) \quad , \quad (\mathrm{km}^{-1}) \tag{5.7}$$

where coefficient q is from Kruse approach. Because the Mie scattering is reflected so intensely, for simplicity we can neglect other influences of extinction. Then, the parameter $\alpha_e(\lambda)$ is approximately equal to the parameter $\beta_a(\lambda)$. Coefficient q has been subject of many works. In original Kruse work is given by [1], [9]:

$$q = \begin{cases} 1.6 & if\ V > 50\ km \\ 1.3 & if\ 6\ km < V < 50\ km \\ 0.585\cdot V^{1/3} & if\ V < 6\ km \end{cases} \quad , \quad (-) \tag{5.8}$$

This empirical Kruse equation was originally intended for applications in geodesy or meteorology where dense fog conditions were out of scope. It is important to have accurate model as far as possible, to describe how optical link operates under various conditions.

I. Kim, B. McArthur and E. Korevaar proposed following extension [9]:

$$q = \begin{cases} 1.6 & if\ V > 50\ km \\ 1.3 & if\ 6\ km < V < 50\ km \\ 0.16 \cdot V + 0.34 & if\ 1\ km < V < 6\ km \\ V - 0.5 & if\ 0.5\ km < V < 1\ km \\ 0 & if\ V < 0.5\ km \end{cases} \quad . \quad (-) \tag{5.9}$$

For calculation of attenuation, we can also choose equation with τ_{TH} = 5% as a transmission threshold, then:

$$\beta_a(\lambda) = \frac{13\,dB}{V}\left(\frac{\lambda}{550nm}\right)^{-q} \approx \alpha_e(\lambda) \quad . \quad (\mathrm{km}^{-1}) \tag{5.10}$$

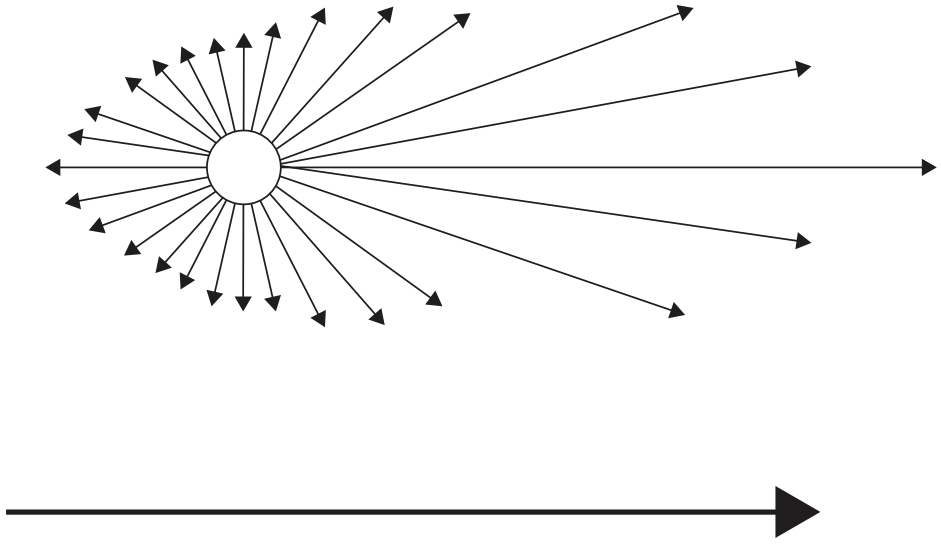

Figure 5.4: Directionality of the Mie scattering.

5.2 Turbulence

Random variations in the refractive index *n* of the atmosphere, otherwise called turbulence are responsible for intensity fluctuations of the transmitted signal. This effect is called scintillation. These turbulences induce effects as a beam spreading (which decreases spatial power density incident on the photodetector) and random motion of the beam centroid about the photodetector called beam wander [3].

Atmospheric turbulences are generated from different temperature of Earth's surface and air. During the day when the Earth surface is warmer than the ambient air, the air closer to the Earth, is warmer. This causes the rising warm air masses upward but also diffraction of the optical beam upward. If this rising is sufficiently large it might cause an effect known as

"mirage" (see Figure 5.5). The situation is reversed at night and optical beam is bending downwards. Besides these effects the atmospheric turbulence disturbs the coherence of the beam. Beam distortion caused by turbulence results in a divergence of beam, changing the position of the beam center and resulting in fluctuations of the signal [6].

Figure 5.5: The hot-road mirage - inverted image of the motorcycles and car on the road [7].

Turbulences can be divided into to the groups, according to the origin. Dynamical turbulences arise at height of about 5 km above the sea level. In this thesis focused on terrestrial optical links, dynamical turbulences will not be discussed further. This thesis is focused on velocity fluctuations, temperature fluctuations and index of refraction fluctuations also called optical turbulence.

Atmosphere can be considered as a viscous fluid as such it has two possible states of motion. In laminar flow, velocity flow characters are uniform and mixing of flows does not occur. In contrast, turbulent flow loses its uniform characteristics due to dynamic mixing. This dynamic mixing creates subflows called turbulent eddies. Figure 5.6 shows the transition of the laminar flow to turbulent [2].

Figure 5.6: Transition from laminar to turbulent flow in the atmosphere [4].

Size and shape of the cell of the turbulent eddy is important for determining of how the beam will be influenced. If the beam width $2W$ is much smaller than the cell size L_T , cell will

bend the propagation direction of the optical beam (Figure 5.7a). When the beam width *2W* is similar to the cell size L_T, cell behaves as an optical lens (Figure 5.7b). Direction of beam propagation does not change but lens effect influences beam divergence. In Figure 5.7c is a situation, where the beam width *2W* is much larger than the cell size L_T. Because of individual rays of beam where each ray is diverted into the different directions there is a intense scattering effect [12].

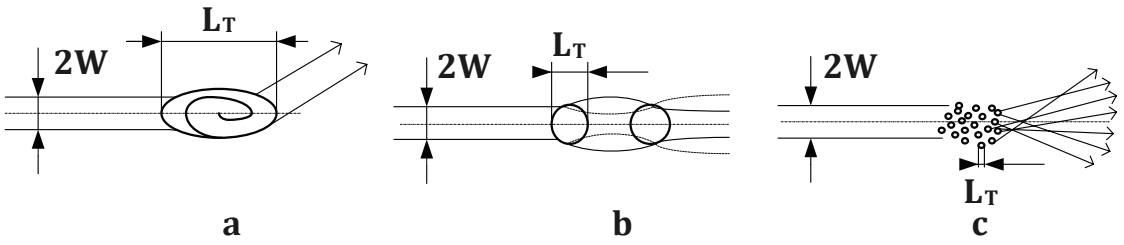

Figure 5.7: Interaction of optical beam with turbulent cells in different sizes [12].

Classical studies of turbulence were concerned with the fluctuations in the velocity field of a fluid with very low level of viscosity. It was found that the wind velocity field of the nature has a random or stochastic field. That means at each point in space and time within the flow the velocity may be represented by a random variable. Turbulent motion of the atmosphere in an environment with moisture and gradients of temperature gives rise to disturbance of refractive index in the form of cells. These cells are called optical turbules. Studies by Kolmogorov suggest that subclass of all optical turbules has a degree of statistical consistency that permits a meaningful theoretical treatment. Optical turbulence is defined as the fluctuations in the index of refraction resulting from the small temperature fluctuations [2].

5.2.1 Velocity fluctuations by Kolmogorov theory of turbulence

To understand the structure of atmospheric turbulence, it is necessary to adopt a Kolmogorov's energy cascade theory shown in Figure 5.8. As the source of energy at large scales is wind shear or convection. The wind velocity increases until it reaches a point where the critical Reynolds number is exceeded. The Reynolds number is a dimensionless number that indicates the boundary between laminar and turbulent environment. Reynolds number can be expressed as [2], [15]:

$$\mathrm{Re} = \frac{v \cdot l}{v_k} \quad (-), \tag{5.11}$$

where v is the air speed, v_k is the kinematic viscosity and l characteristics linear dimension. When the Reynolds number is exceeded there are local unstable air masses (eddies) formed. These eddies have characteristic dimensions slightly smaller than, and independent of, the parent flow. The larger eddies break up into smaller eddies to form a continuum of eddy size for the transfer of energy from macroscale L_0 (outer scale of turbulence) to a microscale l_0 (inner scale of turbulence). The family of eddies bounded above by outer and inner scale forms the

inertial subrange. The turbulence eddies smaller than the inner scale disappears and the remaining energy is dissipated as heat [2].

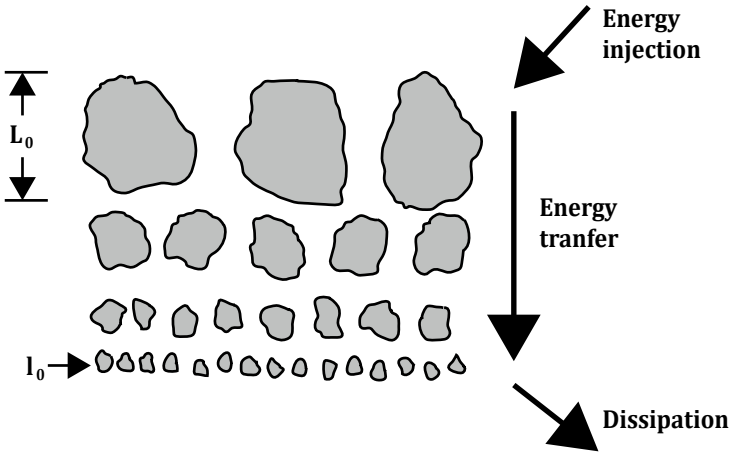

Figure 5.8: Kolmogorov cascade theory of turbulence [2].

The outer scale L_0 means the scale size below which turbule properties are independent of the parent flow. Eddies of scale size smaller than L_0 are expect statistically homogenous and isotropic but eddies of scale size equal or larger to L_0 are generally nonisotropic and their structure is not well defined. At an altitude over 100 m the horizontal dimension of L_0 is much greater than vertical dimension due to stratification. The inner scale is typically on the order of 1 to 10 mm near the ground [2].

Longitudinal structure function of wind velocity in the inertial subrange satisfies the Kolmogorov 2/3 power law:

$$D_{RR}(R) = \left\langle \left(V_1 - V_2\right)^2 \right\rangle = C_V^2 \cdot R^{2/3}, \quad l_0 << R << L_0 \quad (-) \tag{5.12}$$

where $D_{RR}(R)$ is the velocity structure function, V_1, V_2 are velocity components at two points separated by distance R and C_V^2, which is the structure constant of velocity. C_V^2 indicates a measure of the total amount of energy in the turbulence and is given by:

$$C_V^2 = 2 \cdot \varepsilon^{2/3} \quad , \quad (m^{4/3} \cdot s^{-2}) \tag{5.13}$$

where ε is the average energy dissipation rate [2].

It turns out, that strong turbulence has smaller inner scales l_0 and weak turbulence has larger inner scales l_0. On the other hand the outer scale L_0 increases and decreases directly with the strength of turbulence. The behavior of the longitudinal structure function of wind at small sizes ($R << l_0$) varies with the square of R, and can be inferred from Taylor series expansion at small distances [2].

Then longitudinal velocity structure function of wind can be expressed [2]:

$$D_{RR}(R) = \begin{cases} C_V^2 \cdot l_0^{4/3} \cdot R^2, & 0 \le R << l_0 \\ C_V^2 \cdot R^{2/3}, & l_0 << R << L_0 \end{cases} \quad . \text{ (-)} \tag{5.14}$$

The R^2 and $R^{2/3}$ power-law given by equation (5.12) is shown in Figure 5.9 (dashed lines). The solid curve shows the continuous behavior of scaled velocity structure function. Intersection of two asymptotic curves given by R^2 and $R^{2/3}$ defines the inner scale [2].

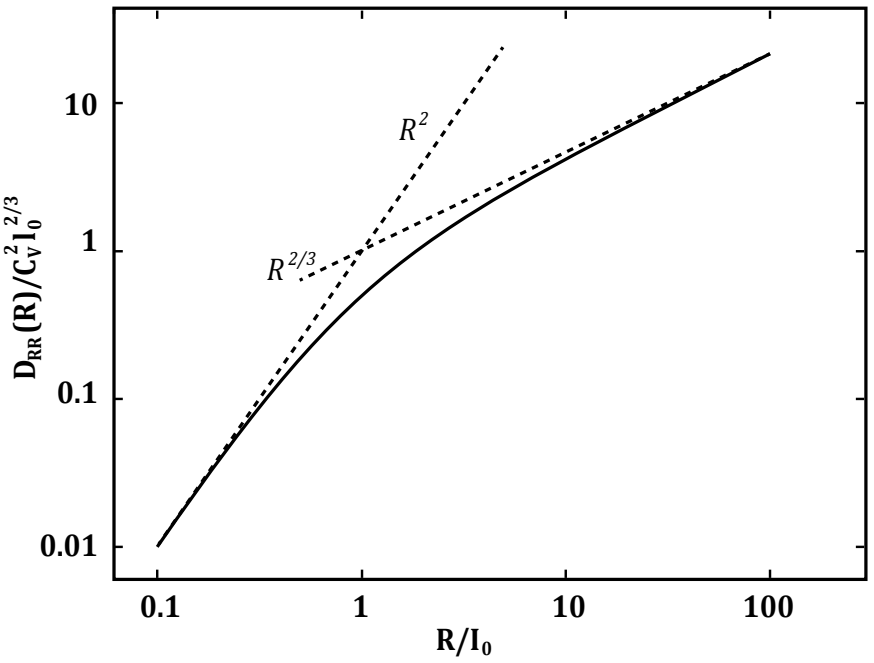

Figure 5.9: The scaled longitudinal velocity structure function of wind [2].

No general description of the velocity structure function can be predicted for $R > L_0$, because the random field of velocity fluctuations is nonisotropic for scale sizes larger than L_0 [2].

Power spectrum in three dimensions is equivalent to the 2/3 power law behavior of velocity structure function and it is given by:

$$\phi_{RR}\left(\vec{\kappa}\right) = 0.066 \cdot \varepsilon^{2/3} \cdot \vec{\kappa}^{-11/3} = 0.033 \cdot C_V^2 \cdot \vec{\kappa}^{-11/3}, \quad 1/L_0 << \vec{\kappa} << 1/l_0 \text{ , (-)} \tag{5.15}$$

where $\vec{\kappa}$ is the scalar spatial frequency (rad·km^{-1}) [2].

5.2.2 Temperature fluctuations by Kolmogorov theory of turbulence

Temperature fluctuations do not exchange energy with the velocity fluctuations and because of this they are considered to be passive. Dissipation mechanism of inhomogeneity is not viscosity as in the case of velocity fluctuations but it is molecular diffusion. Inner and outer scale of small temperature forms the lower and upper boundaries of the inertial-convective range. For statistically homogeneous and isotropic temperature fluctuations we are able to use similar power law relations as used with longitudinal velocity fluctuations. By extending Kolmogorov theory of structure functions, temperature structure function is given by:

$$D_T(R) = \left\langle \left(T_1 - T_2\right)^2 \right\rangle = \begin{cases} C_T^2 \cdot l_0^{4/3} \cdot R^2, & 0 \le R << l_0 \\ C_T^2 \cdot R^{2/3}, & l_0 << R << L_0 \end{cases} \quad , \quad (-) \tag{5.16}$$

where T_1 and T_2 are temperatures at two points separated by distance R. C_T^2 is the temperature structure constant which can be expressed as:

$$C_T^2 = \left(\frac{79 \cdot 10^{-6} \cdot P}{T^2} \right)^{-2} \cdot C_n^2 \quad , \quad (K \cdot m^{-2/3}) \tag{5.17}$$

where P is the pressure and T is the temperature of atmosphere. C_n^2 is structure parameter of refractive-index which will be described in more detail in chapter 5.2.3 [2], [16].

5.2.3 Fluctuations of refractive-index by Kolmogorov theory of turbulence

The refractive-index n is one of the most important parameters in the optical telecommunications. This parameter is very sensitive to small-scale temperature fluctuations combined with turbulent mixing. These influences induce a random behavior of the refractive-index. The position and time depended refractive-index denoted by $n = \left(\vec{R}, t\right)$ can be expressed by as the sum of no turbulence value n_0 and induced random fluctuation component $n_1 = \left(\vec{R}, t\right)$. Thus [1], [2]:

$$n(\vec{R}, t) = n_0 + n_1(\vec{R}, t) \quad . \quad (-) \tag{5.18}$$

Fluctuations of refractive-index are related to temperature and pressure fluctuations. For most engineering applications, the rate of refractive-index fluctuations can be given by:

$$n = 1 + 77.6 \cdot \left(1 + 7.52 \cdot 10^{-3} \cdot \lambda\right) \cdot \frac{P(R)}{T_e(R)} \cdot 10^{-6} \cong 1 + 79 \cdot 10^6 \cdot \frac{P(R)}{T(R)} \ , \ (-) \tag{5.19}$$

where λ is wavelength (μm), P is air pressure (mbar) and T is the temperature (K). Wavelength dependence is small, so for second expression (5.19) is set $\lambda \approx 0.5$ μm [1], [2].

The refractive-index structure parameter C_n^2 ($m^{-2/3}$) is a constant of the strength of turbulence fluctuations in the refractive-index. For terrestrial optical links it is typically within the range from 10^{-13} (strong turbulence) to 10^{-15} $m^{-2/3}$ (weak turbulence). The attenuation caused by turbulence is shown in Figure 5.10. This structure parameter varies as a function of altitude also according local conditions such as terrain type, geographic location, time of day etc. [1], [2], [3].

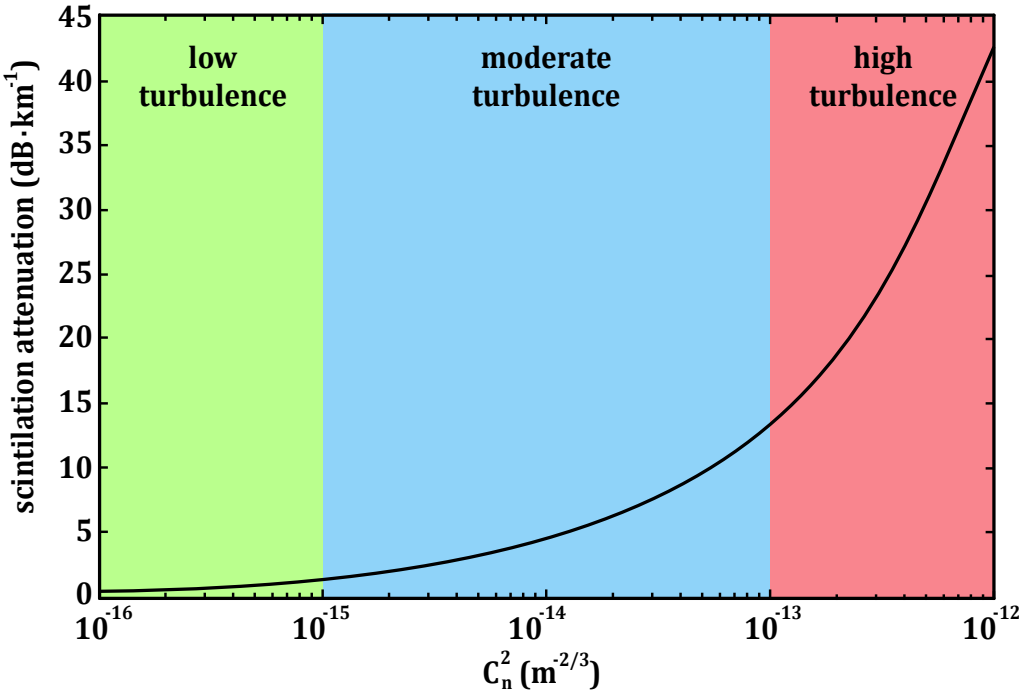

Figure 5.10: The scintillation attenuation based on refractive-index structure parameter [17].

The value of refractive structure parameter can be described by commonly used Hufnagel-Valley model:

$$C_n^2(H) = 0.00594 \cdot \left(\frac{W}{27}\right)^2 \cdot \left(H \cdot 10^{-5}\right)^{10} \exp\left(-\frac{H}{1000}\right) + \\ +2.7 \cdot 10^{-16} \exp\left(-\frac{H}{1500}\right) + A \exp\left(-\frac{H}{100}\right) \quad , \qquad (m^{-2/3}) \qquad (5.20)$$

where H (m) is the height above sea level, W (m·s^{-1})is rms wind speed and A is nominal value of refractive-index structure parameter at the ground. W is commonly set to 21 and A to $1.7 \cdot 10^{-14}$ [1], [2], [5].

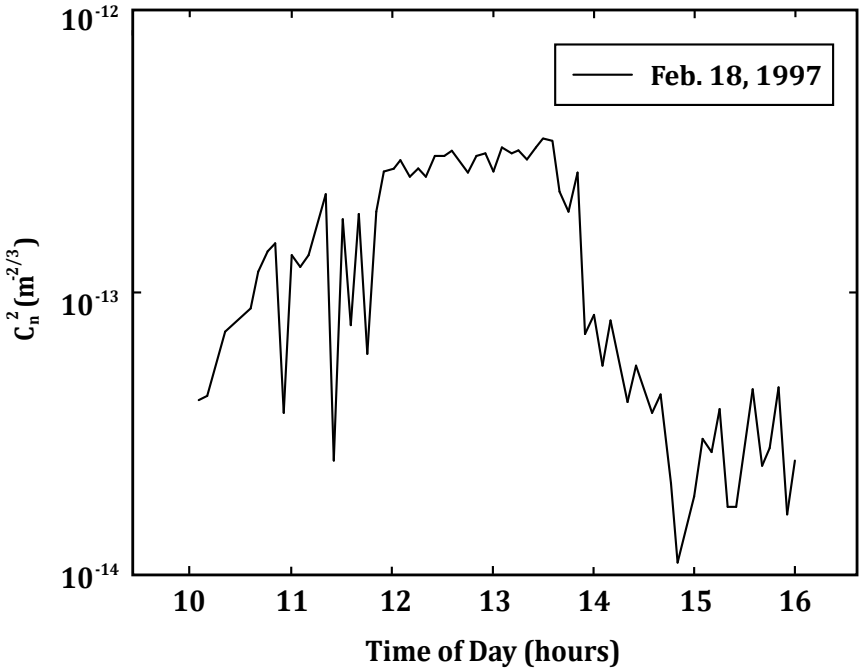

Figure 5.11: The refractive-index structure parameter during daytime [2].

6 Experimental Workplace

As part of this work it was necessary to create an appropriate laboratory and measurement instruments to create suitable conditions for the measurements. The first series of measurements at Krásnopolská building of VŠB - Technical University of Ostrava was proved that measurement results were strongly influenced by parasitic sunlight. Because of this equipment was moved to a more appropriate place - CPIT building of VŠB - Technical University of Ostrava. Used room has the possibility of darkening and it is also spacious enough for measurements. On October 24, 2012, measurement with photon counter PerkinElmer type MP 984 RS was made and the mean value of the light in the room after darkening was $3{,}52 \cdot 10^6$ photons per second.

6.1 Design of Simulation Boxes

Older simulation box available at the university did not match the required measurement quality. It is made of wood with acrylic glass front wall and side windows for the passage of the optical beam. The main disadvantage of this box is small distance for simulation, only 0,5 m as visible in Figure 6.1. Also only three fans can be used. First measurements were made on this box but the results are not included in this study because of clarity of work. Because of these limitations new box was designed suitable for simulating atmospheric conditions.

Figure 6.1: Old simulation box.

The new box was designed with focus on distance of measuring, variability and possibility of further development of measuring options. In the first drafts the simulation distance was determined to 5 m. However this length brings complications due to heavy weight and size of the box. Therefore, the box was divided into the two 2.5 m identical parts as visible in Figure 6.2. The end part of the box is removable for connecting boxes into the one uninterrupted 5 m box. Another advantage of this solution is the opportunity to measure on 2.5 m box only. The upper part of the box is also removable for two reasons. First reason is the possibility of cleaning after using fog simulation and access for fans and cover installation. Second reason is opportunity to turning box upside down and use open bottom side to flow hot air into the box using hot-air fans for simulation of thermal turbulences.

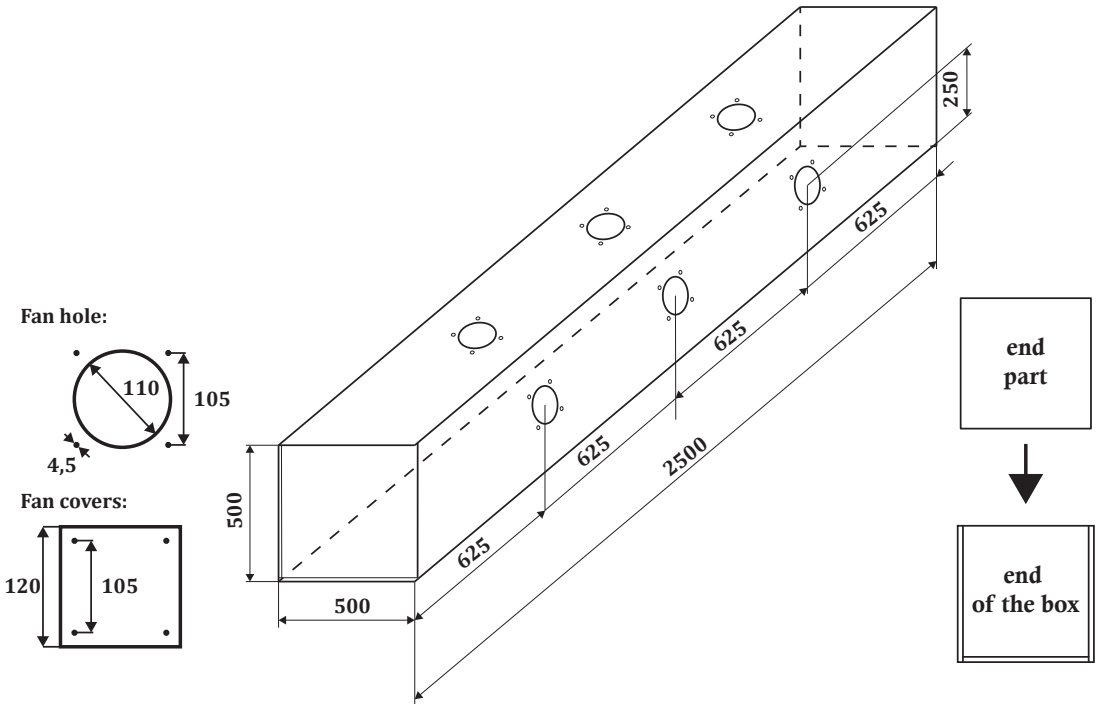

Figure 6.2: Layout of new simulation box (dimensions are in mm).

Another aspect of the box design was creating suitable conditions for measurement of various atmospheric conditions. The entire box is made from acrylic glass. Special holes were carved to place 120 mm fans. To cover holes for example when filling box with the fog, covering caps were made (shown in Figure 6.3). 2.5 meters part of the box, ready for the measurement of mechanical turbulence is shown in Figure 6.4. Height-adjustable stands for box were also designed during this work.

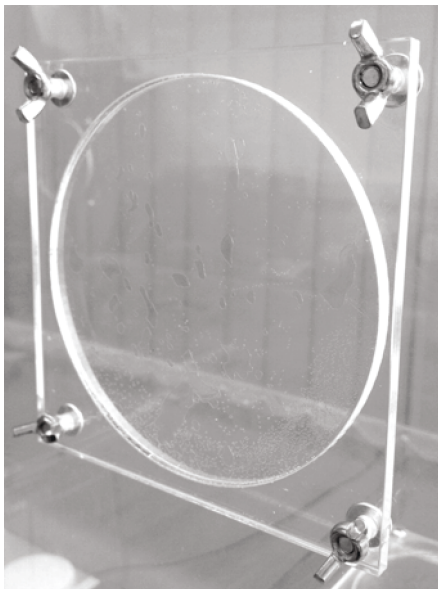

Figure 6.3: Detail of box design - cover on fan hole (fog measurement)

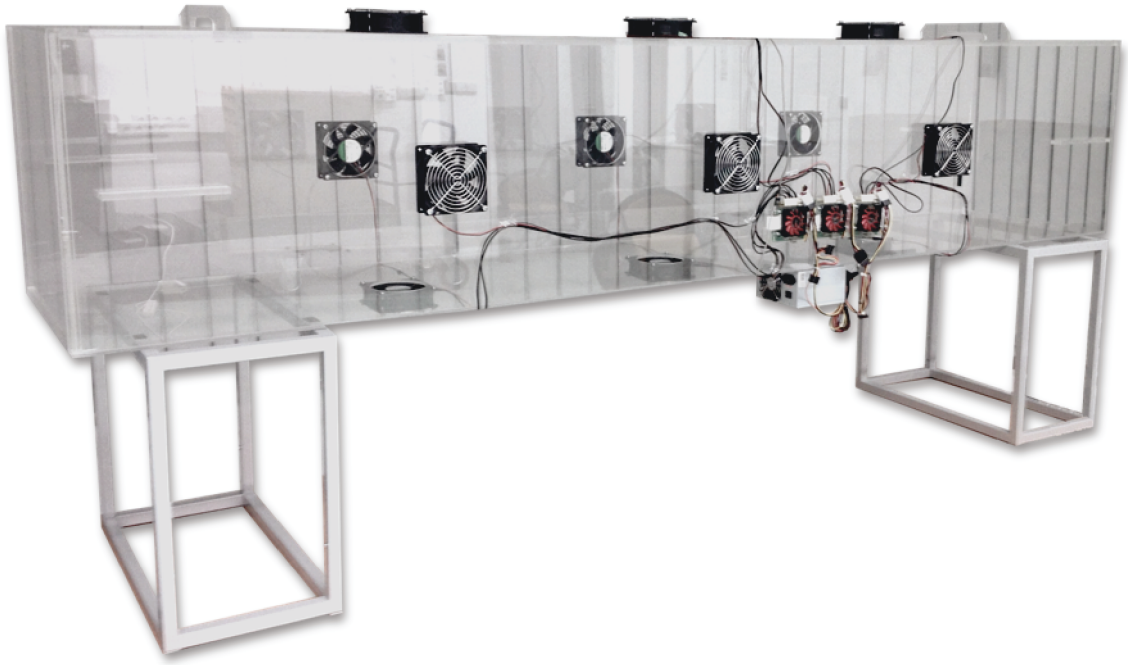

Figure 6.4: Simulation box ready for measurement of velocity turbulence.

For the measurement of velocity turbulence fans PMD1212PMB1-A (19.2W, 4200 RPM) were used with protective grille against accidental contact with the blades. Fan control units T-Balancer bigNG were used due to possibility of different configurations and settings. This controller can manage 4 fans (up to 20W on one channel) with the possibility of setting and monitoring fans speed and connecting of many temperature sensors. 2 heat fans Cata Empire CTH-5000 and 2 heat fans Solac TH 8325 were used for the creation of the temperature

turbulences. Each of these fans has the input power equal to 2 kW. Industrial Fog machine Antari F-80Z was used to produce fog conditions in the box (Figure 6.5). By the analysis of the used liquid for generating fog was found that the main ingredient in this liquid is ammonium chloride (NH_4Cl).

Figure 6.5: Fog machine Antari F-80Z

Measurement of atmospheric conditions in the box during measurement was managed by data-logger Voltcraft DL-181THP. This data-logger allows to wireless measure of temperature, pressure and humidity inside the box. Data-logger can be configured using PC with Voltcraft software, where it is possible to set interval of measurement duration and other parameters (maximum and minimum temperature, sound warning, etc.). Up to 10000 values can be saved into the internal memory of this data-logger.

6.2 Software Applications for Measuring

Two software applications in MATLAB were created for communication on serial link with measuring device Thorlabs PM 120. The development of these applications began in bachelor thesis of the author. The first application is a utility for saving optical power from detector of measuring device. In user interface of this application is necessary to choose serial port on which the measuring device is located. User is able to choose measuring wavelength directly from the application. Also time and number of measurement can be selected. Measuring interval is fixed at 0.25 second. The resulting data are stored in text that can be easily imported to further processing. With this application it was possible to perform all the measurements that were measured by Thorlabs PM 120. Application interface is illustrated in Figure 6.6.

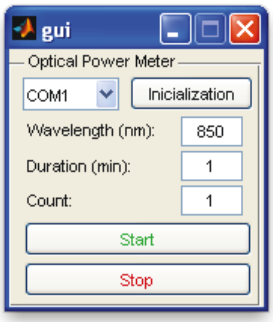

Figure 6.6: Application for saving optical power from PM120.

The second application (shown in Figure 6.7) was developed for cross-sectional measuring of optical beam. This application allows using the special biaxial device Festo for moving in 2D space with optical power meter Thorlabs PM 120 for saving results. Communication with devices works on three connections over serial port RS-232. New version of this application provides significantly better stability of application, possibility of setting the number of repeated measuring and saving text file by the date and time of measurement. After completion of the measurement 3D graph is displayed. After few measurements this application was used only for finding the maximum power of beam in space.

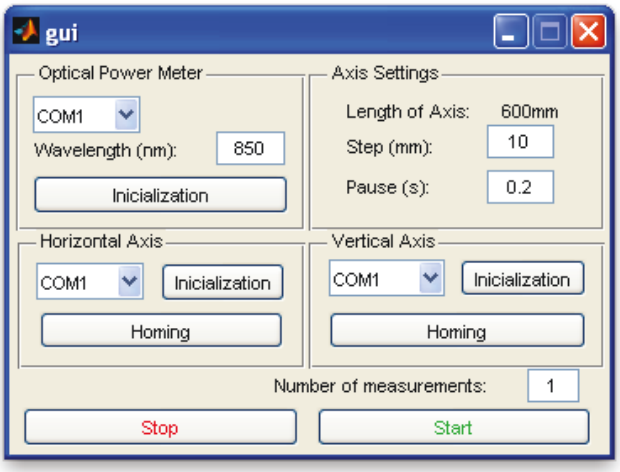

Figure 6.7: Application for the power measurement of the cross section optical beam.

6.3 Laser Sources and Detectors Used for Measurement

First measurements were performed on the LED optical head WO-LINK 4E1/300 which works at λ=850 nm. However, this head not proved to suitable for further measurements because of its stability of optical power. The values of optical power in long-term measurements varied in the range of 0.1 mW - without simulating atmospheric conditions. This instability can be attributed to equipment age. Another unusable optical power source was pigtailed DFB laser SPL1550-1-9-PD (λ=850 nm) collimated by Edmund optics 0.50 NA Fiber Collimator. This laser had also very varied output power. After stability measurements was used following type of lasers.

At wavelength 632.8 nm was used tubed Helium Neon laser 25-LHP-151-230 (15 mW of output optical power). This laser is characterized by high stability of the output optical power. Laser light is in visible spectrum and because of this it was easy to find laser beam on the other side of the simulated connection. Laser is shown in Figure 6.8. Output optical beam was not collimated and optical power on detector was approximately 5 mW.

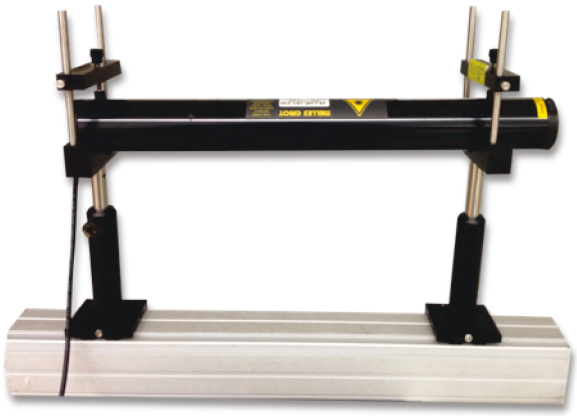

Figure 6.8: Laser source (Helium Neon) for measurement at 632.8 nm - 15 mW.

Laser diode Thorlabs L850P030 (30 mW of output optical power) with collimator Thorlabs C110TME-B (Figure 6.9) was used for measurements at 850nm Collimator in S1TM09 adapter was positioned in temperature controlled laser diode mount TCLDM9 controlled by current driver LCD205C a temperature driver TED200C. Collimated laser source in adapter is shown Figure 6.10. Output optical power was set to 5 mW.

Figure 6.9: Laser source for measurement at 850 nm - 30 mW.

Figure 6.10: 850 nm laser source is positioned in laser diode mount and collimated.

The third type of laser source was laser module Thorlabs LDM1550. This adjustable laser source has collimated output beam with maximal output power 5 mW at 1550 nm. Entire laser is placed in tube.

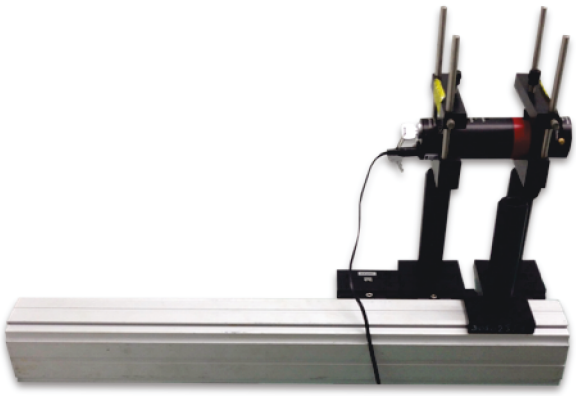

Figure 6.11: Laser source for measurement at 1550 nm - 5 mW.

For measurement of optical power two Thorlabs devices were used. PM 120 device with silicon photodiode S120B was determined to measure the wavelength 632.8 nm and 850 nm. Measuring device was controlled over serial connection by application mentioned above. Measurement at 1550 nm was done by optical power meter PM100D using germanium photodiode S122C. Application to remove and store data is available for this measuring device already.

To determine ideal time for measurement of turbulence, following method was used. The same measuring conditions were used as in measurement of mechanical turbulence mentioned below. Optical power values were measured for different times - 1, 2, 3, 5, 10, 15, 20, 30, 40, 50, 60, 70, 80, 90, 100, 110 and 120 minutes. Results from these measurements were plotted into the histograms of probability. Result from these histograms proved that the result does not change significantly after 15 minutes of measuring. It was confirmed that 20 minutes would be sufficient time for the measurement by this method.

7 Measurement in Simulation Boxes

The objective of the measurement in simulation boxes was how different influences affects optical beam. The selected factors for measuring were fog and two types of turbulence (velocity and thermal). The goal of measurements was also testing of spectral dependence of these effects and dependence on length of simulation link. In Figure 7.1 we can see schematic layout for all measurements. The distance between the laser source and the box was 250 mm. Also distance between photodetector and box was 250 mm.

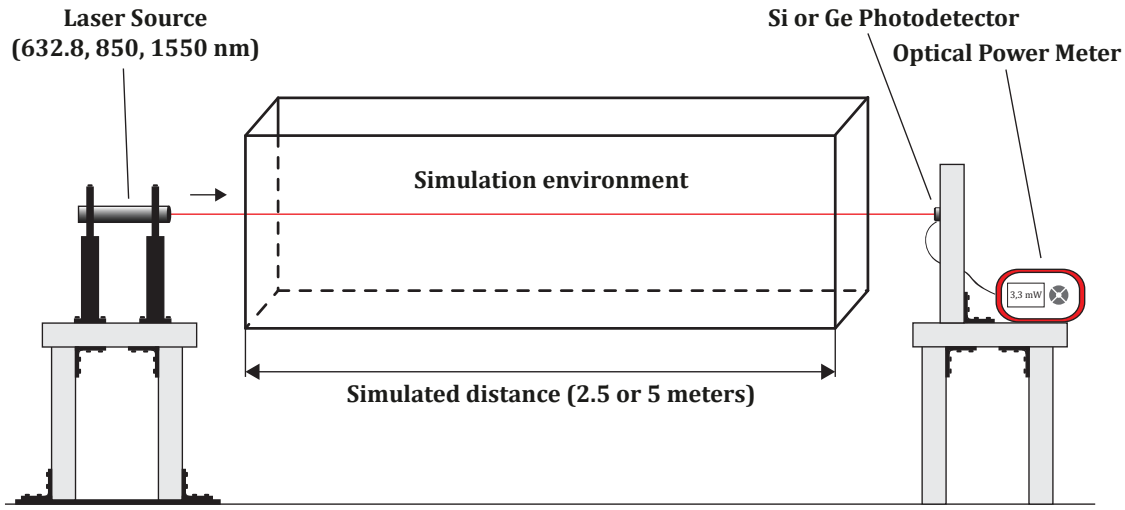

Figure 7.1: Schematic layout of the workspace for measurement of atmospheric conditions.

7.1 Measurement of Velocity Turbulences

The methodology for the measurements of velocity turbulences was following. Velocity turbulence conditions using a total of 12 fans installed on all 4 sides of the box as visible in Figure 7.2 were formed in the simulation box with length of 2.5 m. The end of box is open to get air out. 24 fans on two boxes were used in configuration with length of 5 m. Between these two boxes was a 250 mm gap to get air out (shown in Figure 7.3). Measurement for both distances and all wavelengths was measured for 20 minutes (with interval 0.25 second). Total 10 measurements were done for each wavelength and distance. The resulting values of these 10 measurements were averaged a brought to the variability plots using application Statgraphics Centurion. Reference data were measured and averaged in the same way.

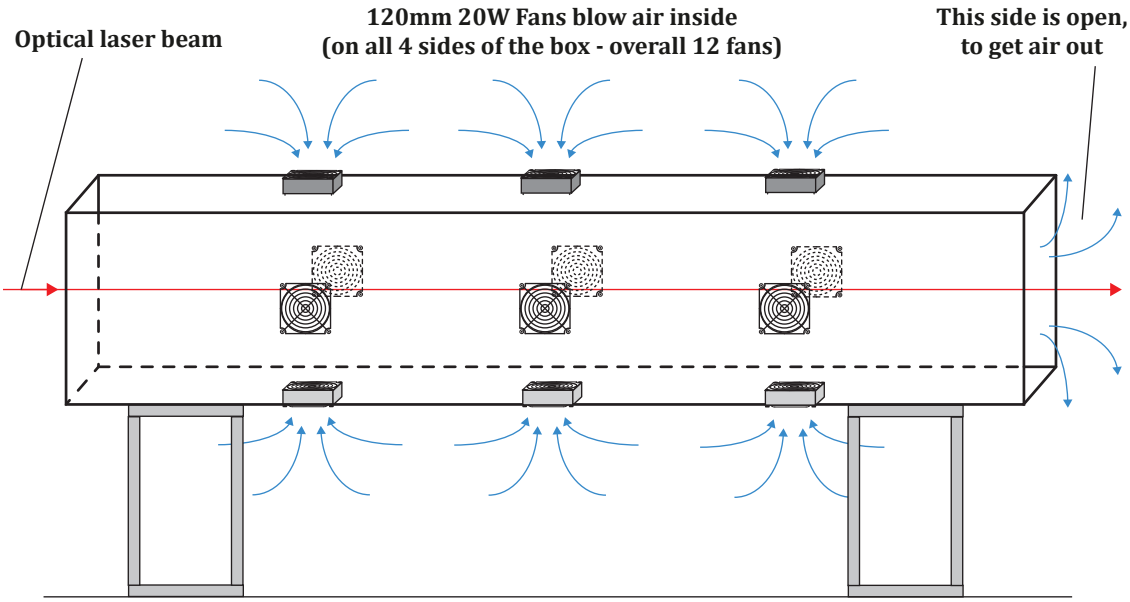

Figure 7.2: Schematic layout for the measurement of velocity turbulence at distance of 2,5 m.

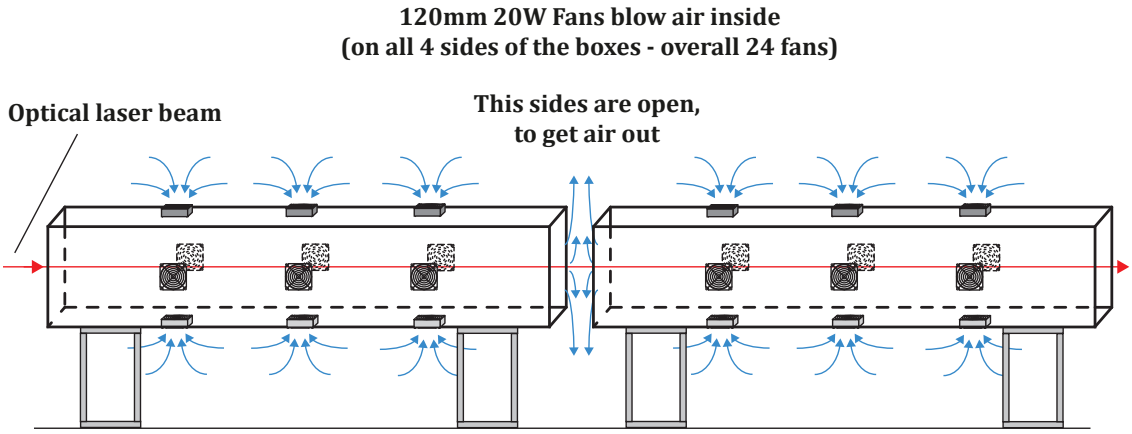

Figure 7.3: Schematic layout for the measurement of velocity turbulence at distance of 5 m.

7.1.1 The measurement results

The variation coefficient of velocity turbulence for each distance and wavelength and variance coefficient of reference (without fans) is shown in Table 7.1. The effect of velocity turbulence visible in Table 7.1 was calculated as a variation coefficient of velocity turbulence divided by coefficient of reference.

At wavelength 632.8 nm and 1550 nm, we can see small variation coefficient of reference compared to 850 nm. Results at 850 nm can be affected by this instability of laser source. If we look at the effect of velocity turbulence in Table 7.1, we can see behavior changes depending on the wavelength. At 632.8 nm effect of velocity is minimal. These results are also visible in the graphs of variance in Figure 7.4 and Figure 7.5. The difference between variances

is almost impossible to see in graphs. At 850 nm values of velocity turbulence effect are also affected only minimally. However here occurs a phenomenon where variation coefficient is more influenced in case of reference and effect of velocity is opposite to what is expected. This effect can be assign to the aforementioned power stability of this laser source. Results of 850 nm are shown in Figure 7.6 and Figure 7.7. Results at wavelength of 632.8 nm and 850 nm can be considered as the changes in term of measurement inaccuracy. We can say that these wavelengths are not or very little affected by velocity turbulence. At a wavelength of 1550 nm, the variance with turbulence significantly increased which is very visible in graphs in Figure 7.8 and Figure 7.9. Unfortunately, these particular results were probably influenced by type of laser mount. It was found that the optical power is varied because of weak assembly and movements of the building. According to the theoretical assumptions we can say that the measurements in these first experimental tests were influenced by measurement error. For measurement of thermal turbulence and effects of fog, the laser mount has been modified.

Table 7.2 shows atmospheric conditions during measurement. We can see that the conditions for measurement in 5 m were identical, because all three measurements were made at the same time.

Table 7.1: Comparison of coefficient of variation due to velocity turbulence.

Wavelength	Simulated Distance	Variation Coefficient of Reference	Variation Coefficient of Velocity Turbulence	Effect of Velocity Turbulence
632.8 nm	2.5 m	0.01673 %	0.01954 %	1.17
632.8 nm	5.0 m	0.02767 %	0.03486 %	1.26
850.0 nm	2.5 m	0.13403 %	0.09387 %	0.70
850.0 nm	5.0 m	0.09528 %	0.08784 %	0.92
1550.0 nm	2.5 m	0.01415 %	0.10606 %	7.50
1550.0 nm	5.0 m	0.00919 %	0.13125 %	14.28

Table 7.2: Conditions of measurement for velocity turbulence.

Wavelength	Simulated Distance	Temperature	Pressure	Humidity
632.8 nm	2.5 m	22.2 °C	982.7 hPa	25.4 %
632.8 nm	5.0 m	22.7 °C	978.6 hPa	30.2 %
850.0 nm	2.5 m	22.5 °C	986.4 hPa	25.3 %
850.0 nm	5.0 m	22.7 °C	978.6 hPa	30.2 %
1550.0 nm	2.5 m	21.6 °C	996.8 hPa	27.5 %
1550.0 nm	5.0 m	22.7 °C	978.6 hPa	30.2 %

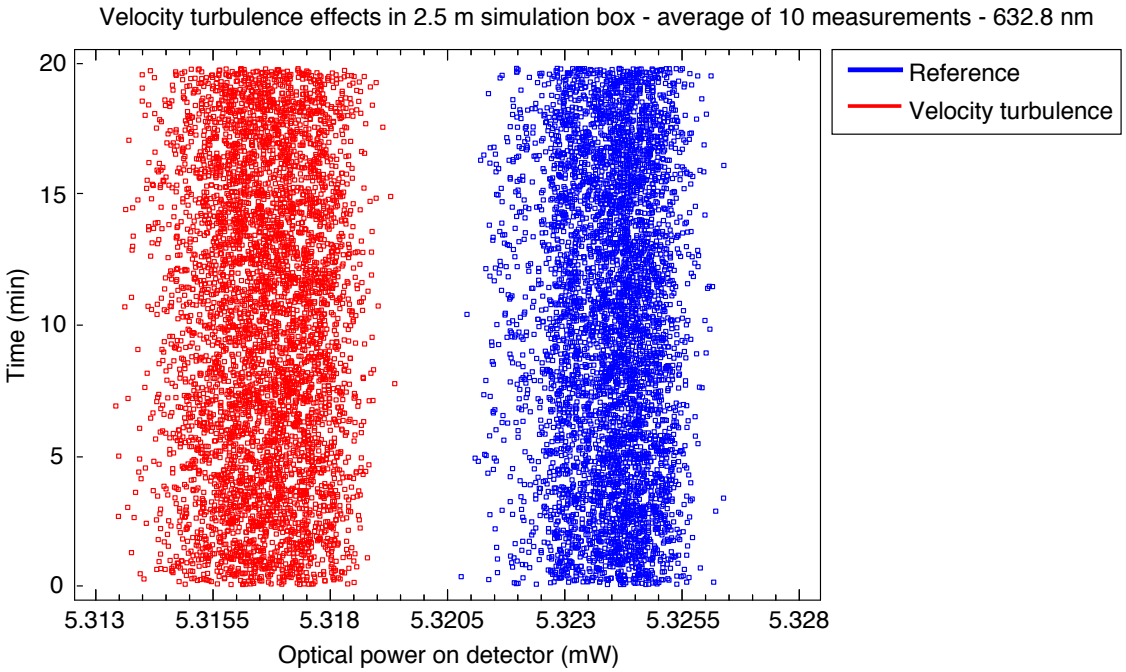

Figure 7.4: Velocity turbulence effects at 632.8 nm - 2.5 m of length.

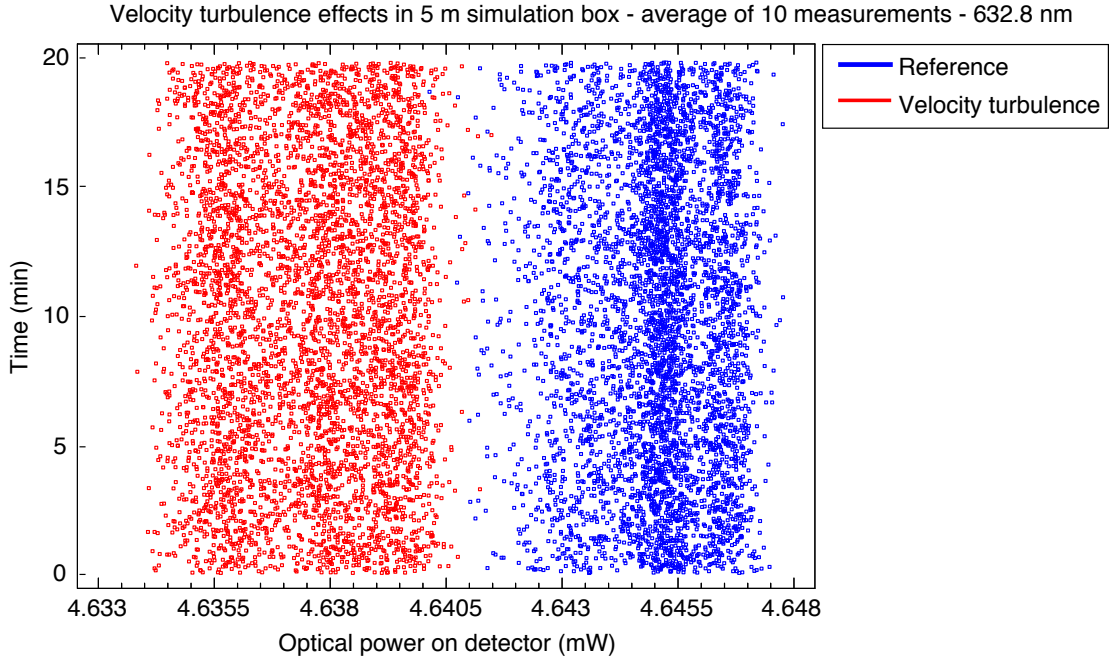

Figure 7.5: Velocity turbulence effects at 632.8 nm - 5 m of length.

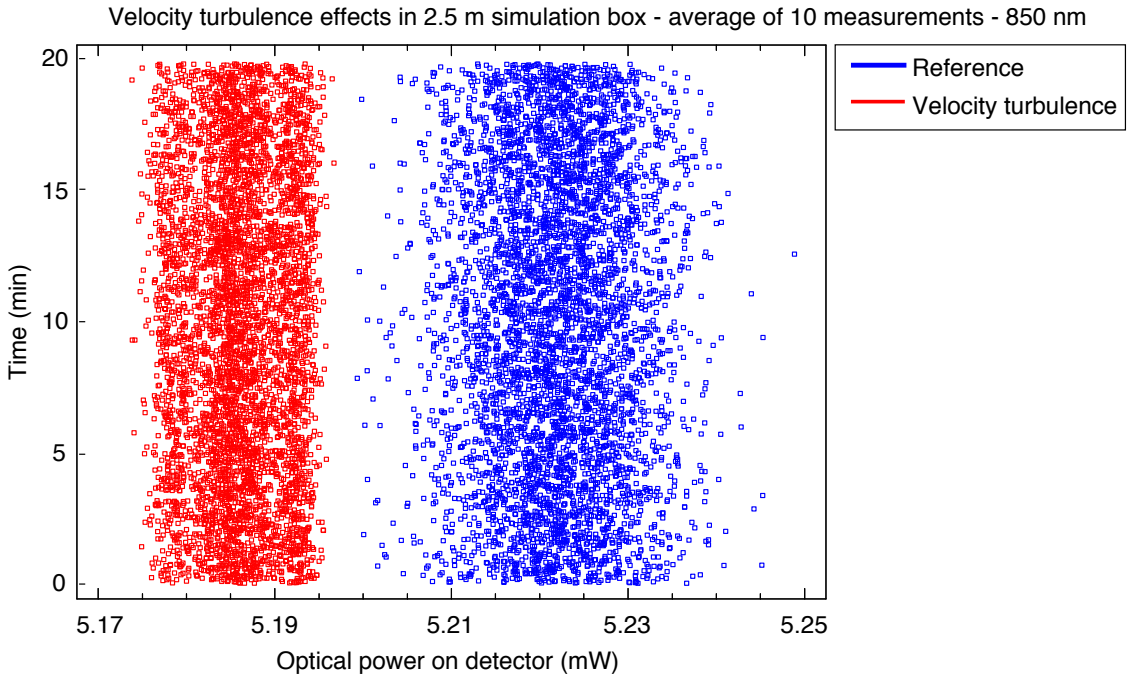

Figure 7.6: Velocity turbulence effects at 850 nm - 2.5 m of length.

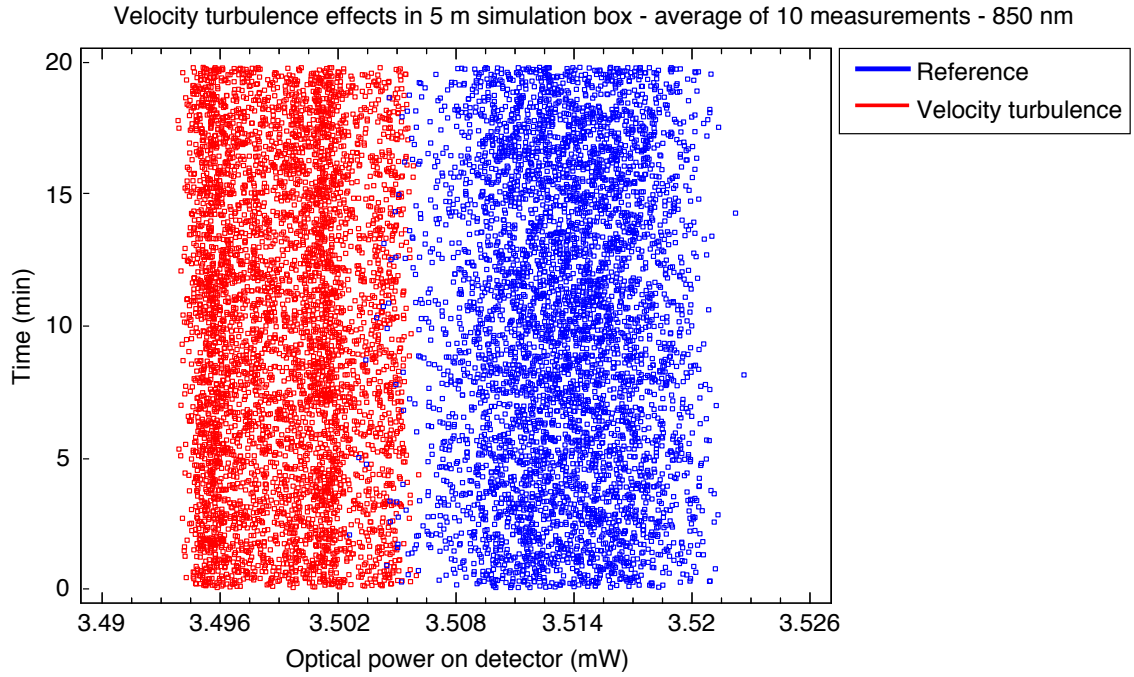

Figure 7.7: Velocity turbulence effects at 850 nm - 5 m of length.

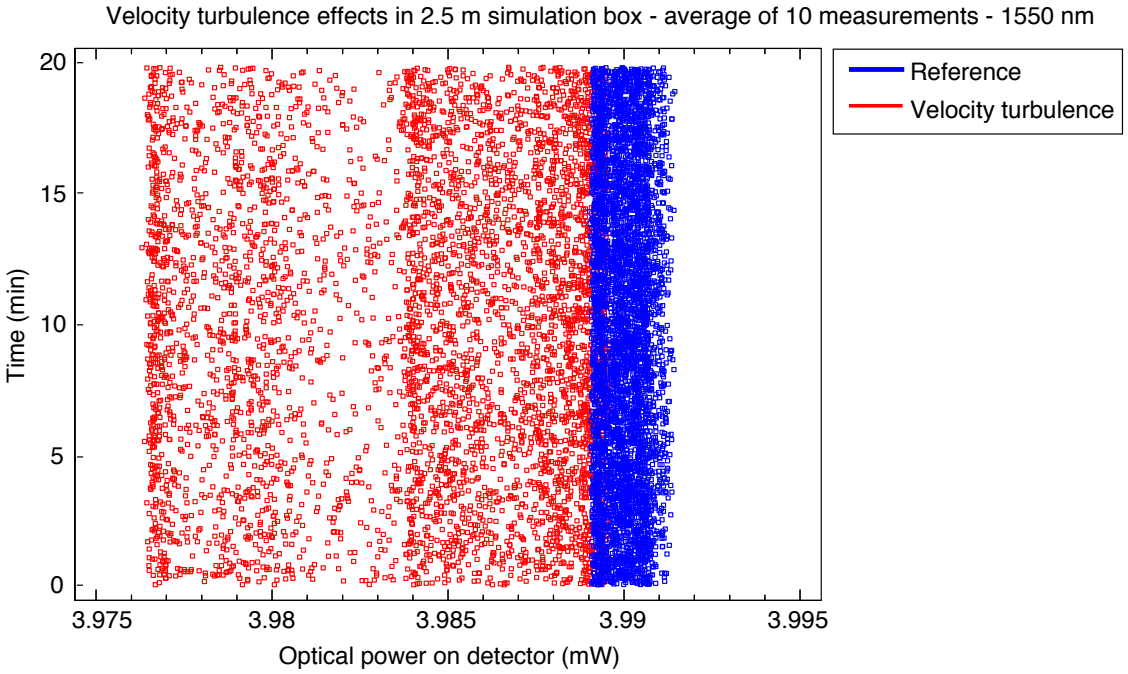

Figure 7.8: Velocity turbulence effects at 1550 nm - 2.5 m of length.

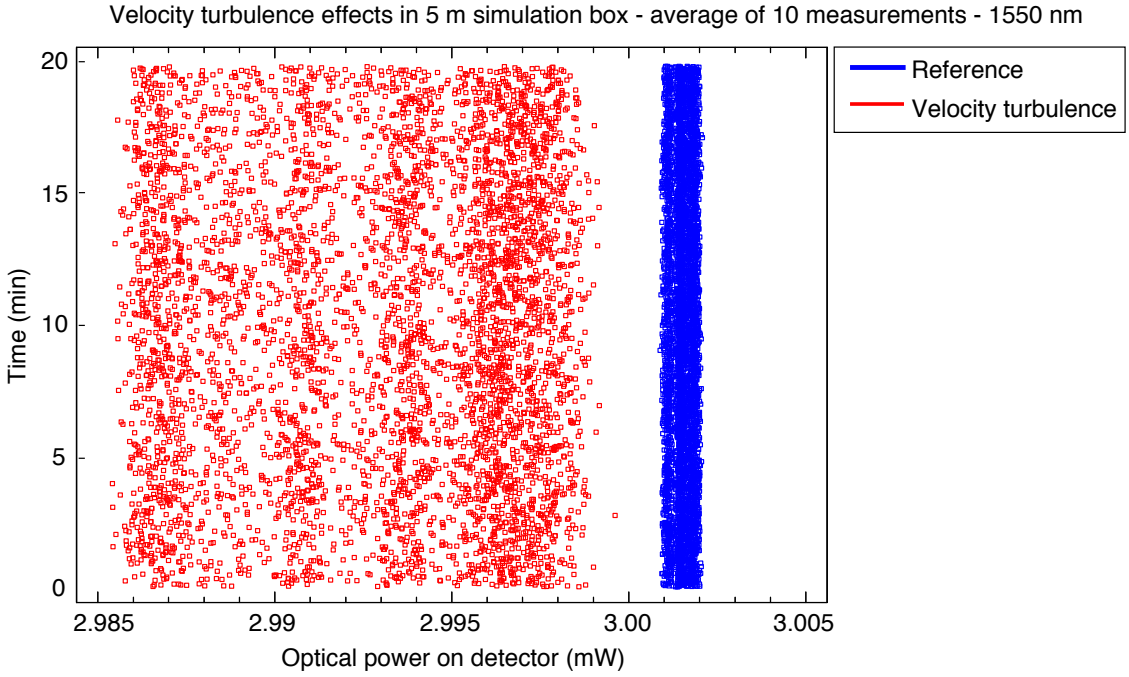

Figure 7.9: Velocity turbulence effects at 1550 nm - 5 m of length.

7.2 Measurement of Temperature Turbulences

It was necessary to create suitable conditions in simulation box to measure the temperature turbulences. This was done by turning box upside down with removed bottom part and then was possible to place 4 heat fans under the box. One of the fans (previously used for velocity turbulence) was placed on top of the box and used for heat removal (due to requirement of different temperatures for creating thermal turbulences). Schematic layouts are shown in Figure 7.10 and Figure 7.11. In Figure 7.12 we can see temperature outside and inside the box measured by thermal imaging camera FLIR E50. The measurement for both distances and all wavelengths was measured for 20 minutes. Total was 10 measurements done for each wavelength and distance in the same way as in case of velocity. Also reference data were measured 10 times for 20 minutes (with interval 0.25 second). These data were also averaged and processed in Statgraphics Centurion.

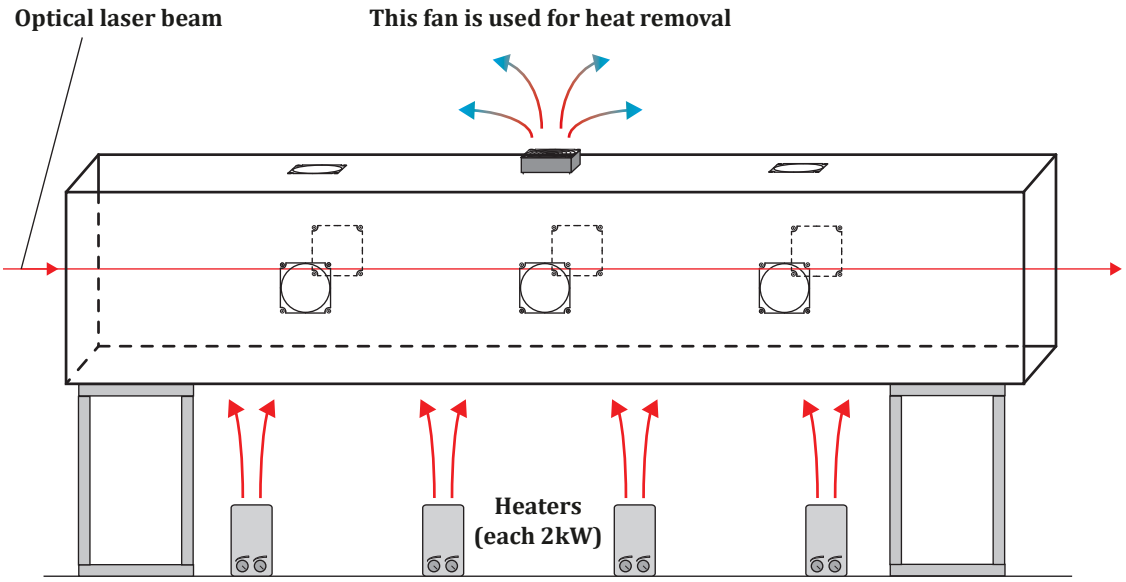

Figure 7.10: Schematic layout for the measurement of thermal turbulence - 2,5 m.

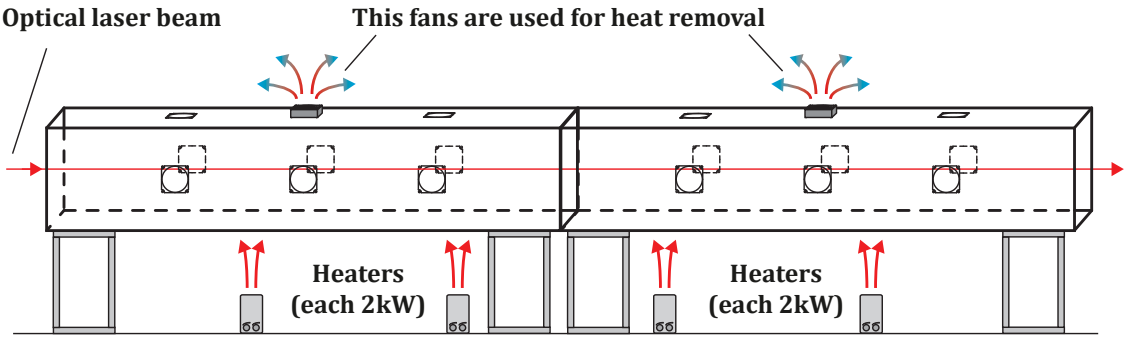

Figure 7.11: Schematic layout for the measurement of thermal turbulence - 5 m.

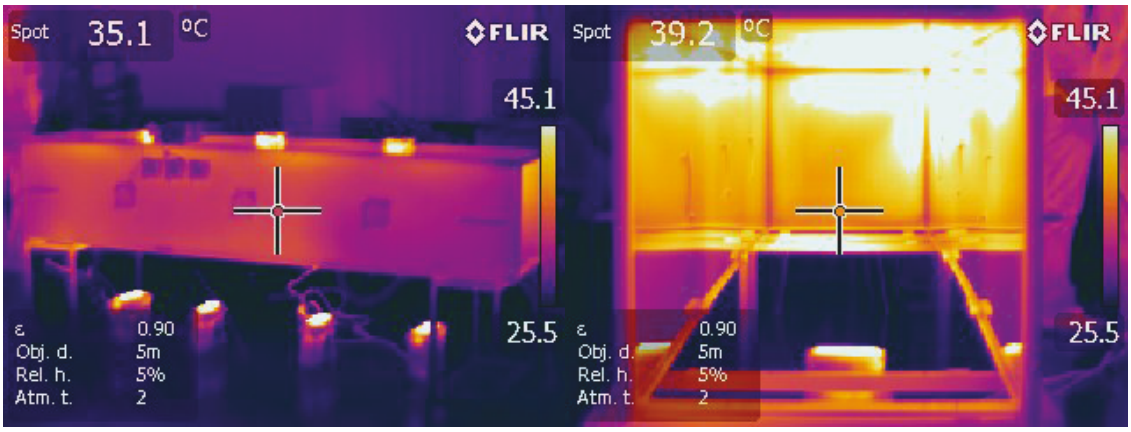

Figure 7.12: Temperature outside and inside of the simulation box.

Figure 7.13: The simulation box ready for measurement of thermal turbulences - 2.5 m.

7.2.1 The measurement results

We can see larger variation coefficient of reference at 850 nm as in case of velocity turbulence in Table 7.3, which is again due to less stable laser source at this wavelength. We see at first glance that the temperature turbulence greatly affects the optical power and very increase fluctuations of the power on detector. Results in Table 7.3 shows that the effect of thermal turbulence is higher at distance of 5 meters. The effect of thermal turbulence visible in was calculated as a variation coefficient of thermal turbulence divided by coefficient of reference.

This result was expected for two reasons. The first is the larger influence of environment in the box due to longer distance. The second result is that the space between heat fans is bigger so in the box should be higher temperature differences and thus higher thermal turbulence. However the most interesting is the comparison of results based on the wavelength. We can see that laser source at 632.8 nm is most affected source of radiation. With increasing wavelength the value of thermal turbulence effect decreases. At a wavelength of 1550 nm compared to 632.8 nm decreased this effect more than 2 times. These results are also shown in graphs from Figure 7.14 to Figure 7.19.

Table 7.4 shows atmospheric conditions during measurement. Conditions for measurement at distance of 5 m were identical again, because all three measurements were made at the same time.

Table 7.3: Comparison of coefficient of variation due to thermal turbulence.

Wavelength	Simulated Distance	Variation Coefficient of Reference	Variation Coefficient of Thermal Turbulence	Effect of Thermal Turbulence
632.8 nm	2.5 m	0.01673 %	0.15636 %	9.34
632.8 nm	5.0 m	0.02767 %	0.70264 %	25.40
850.0 nm	2.5 m	0.09146 %	0.60092 %	6.57
850.0 nm	5.0 m	0.09528 %	1.36050 %	14.28
1550.0 nm	2.5 m	0.01753 %	0.08693 %	4.96
1550.0 nm	5.0 m	0.00935 %	0.09798 %	10.48

Table 7.4: Conditions of measurement for thermal turbulence.

Wavelength	Simulated Distance	Temperature	Pressure	Humidity
632.8 nm	2.5 m	49.6 °C	980.1 hPa	19.6 %
632.8 nm	5.0 m	47.4 °C	980.6 hPa	5.8 %
850.0 nm	2.5 m	48.7 °C	980.2 hPa	20.2 %
850.0 nm	5.0 m	47.4 °C	980.6 hPa	5.8 %
1550.0 nm	2.5 m	47.5 °C	995.4 hPa	22.7 %
1550.0 nm	5.0 m	47.4 °C	980.6 hPa	5.8 %

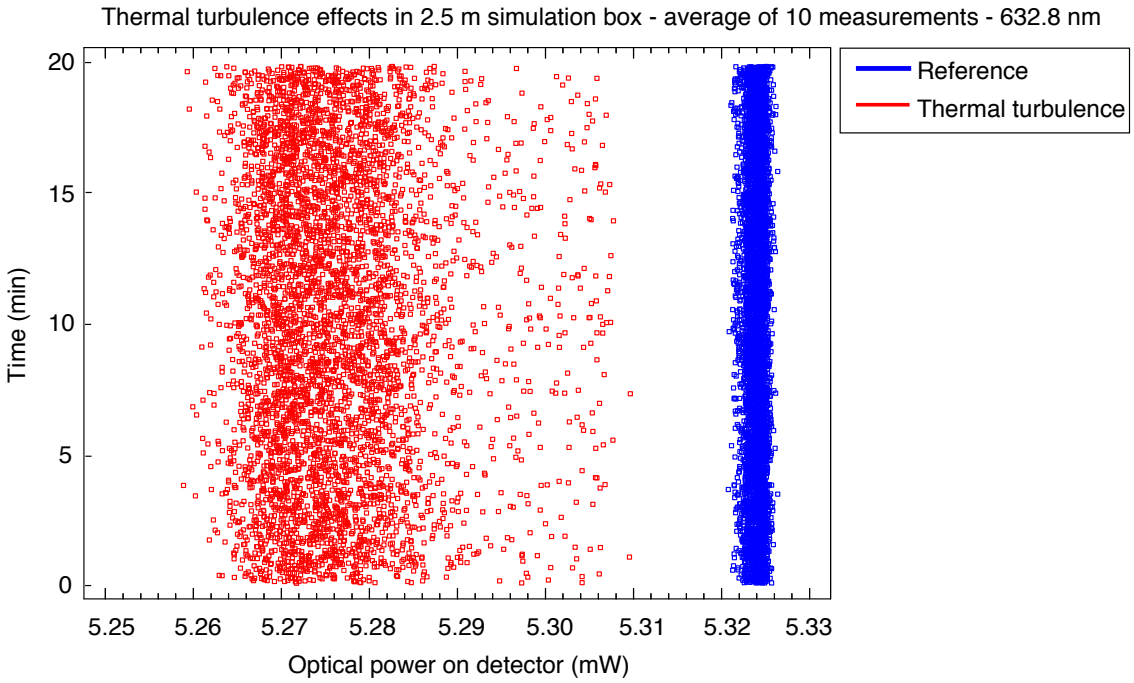

Figure 7.14: Thermal turbulence effects at 632.8 nm - 2.5 m of length.

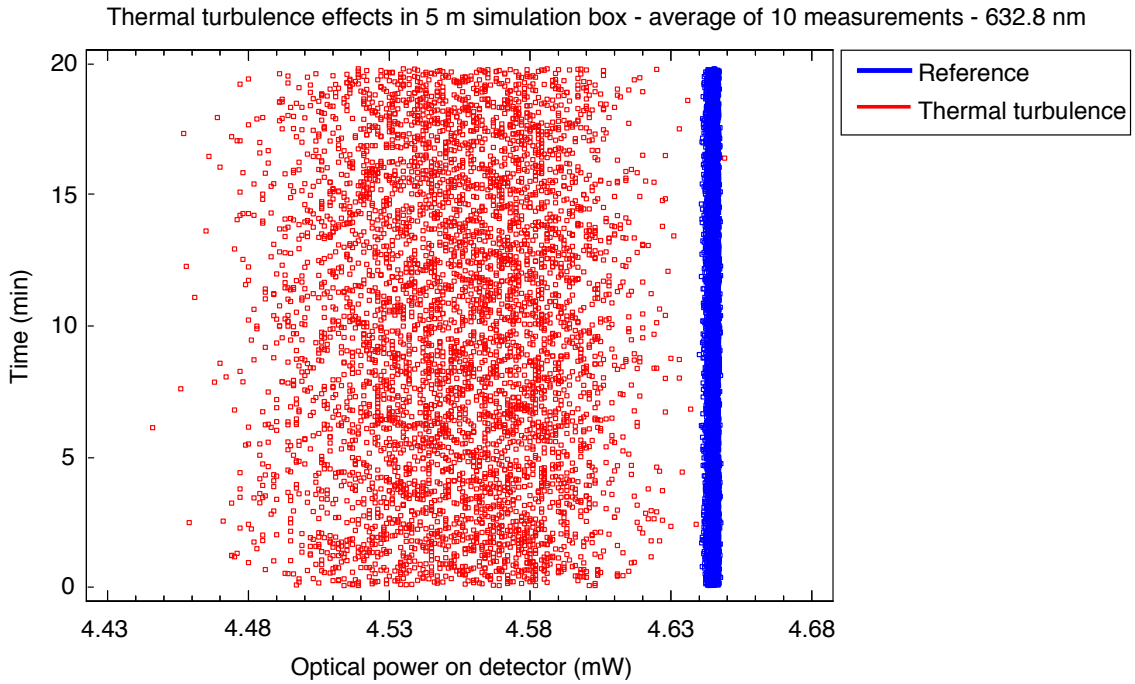

Figure 7.15: Thermal turbulence effects at 632.8 nm - 5 m of length.

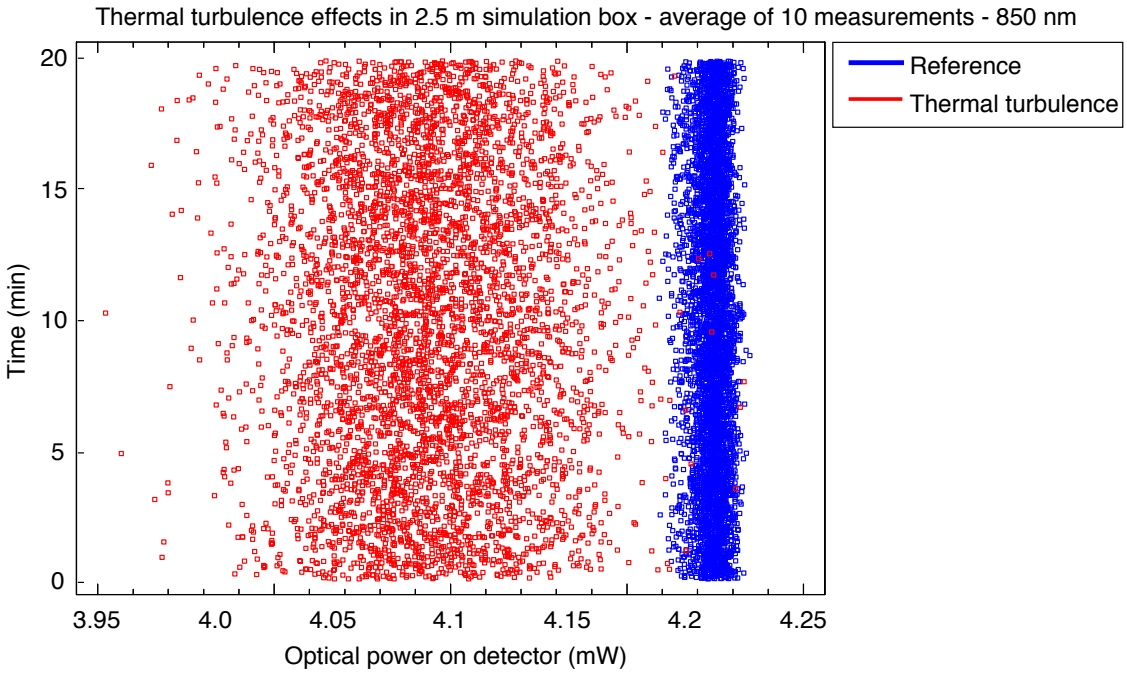

Figure 7.16: Thermal turbulence effects at 850 nm - 2.5 m of length.

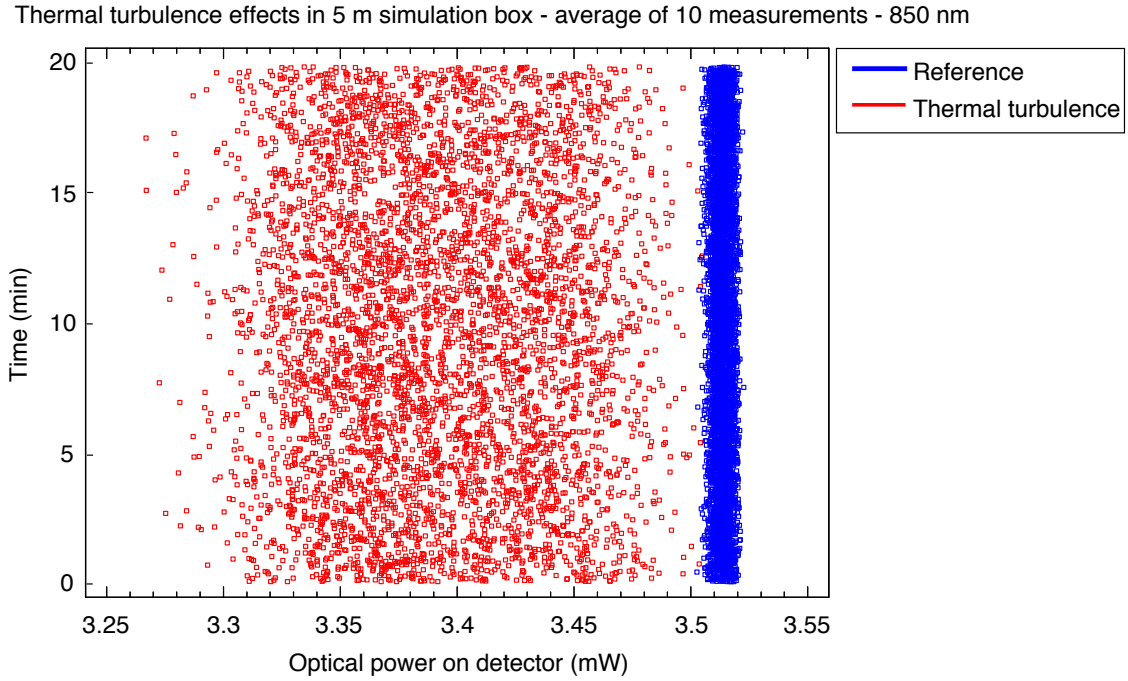

Figure 7.17: Thermal turbulence effects at 850 nm - 5 m of length.

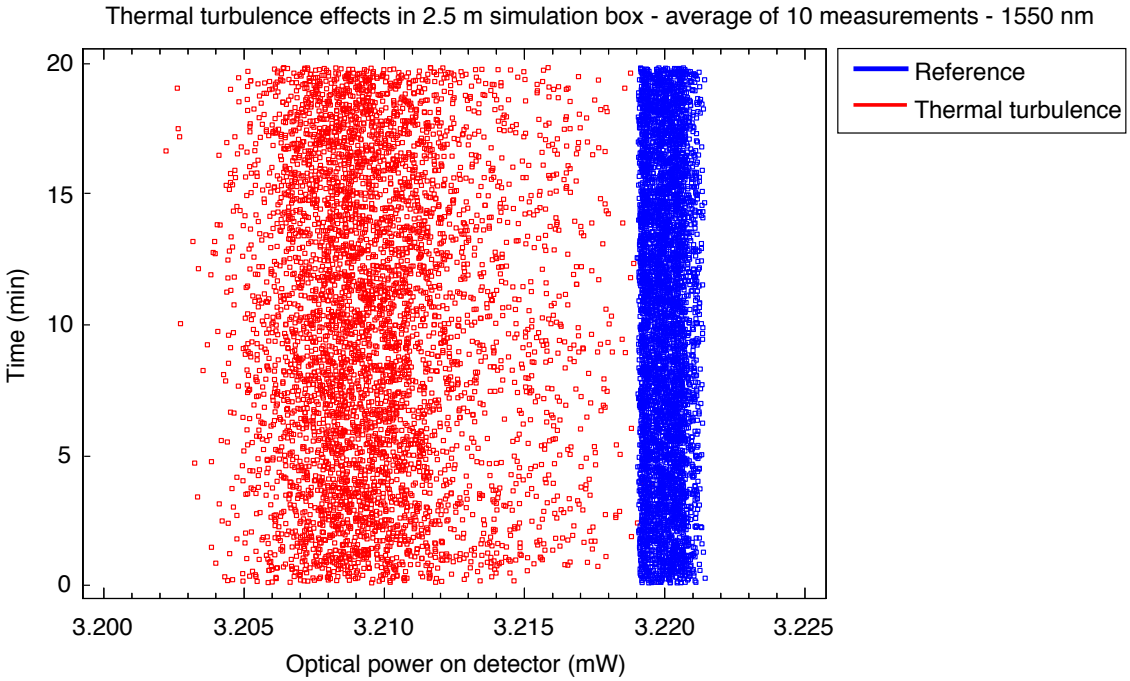

Figure 7.18: Thermal turbulence effects at 1550 nm - 2.5 m of length.

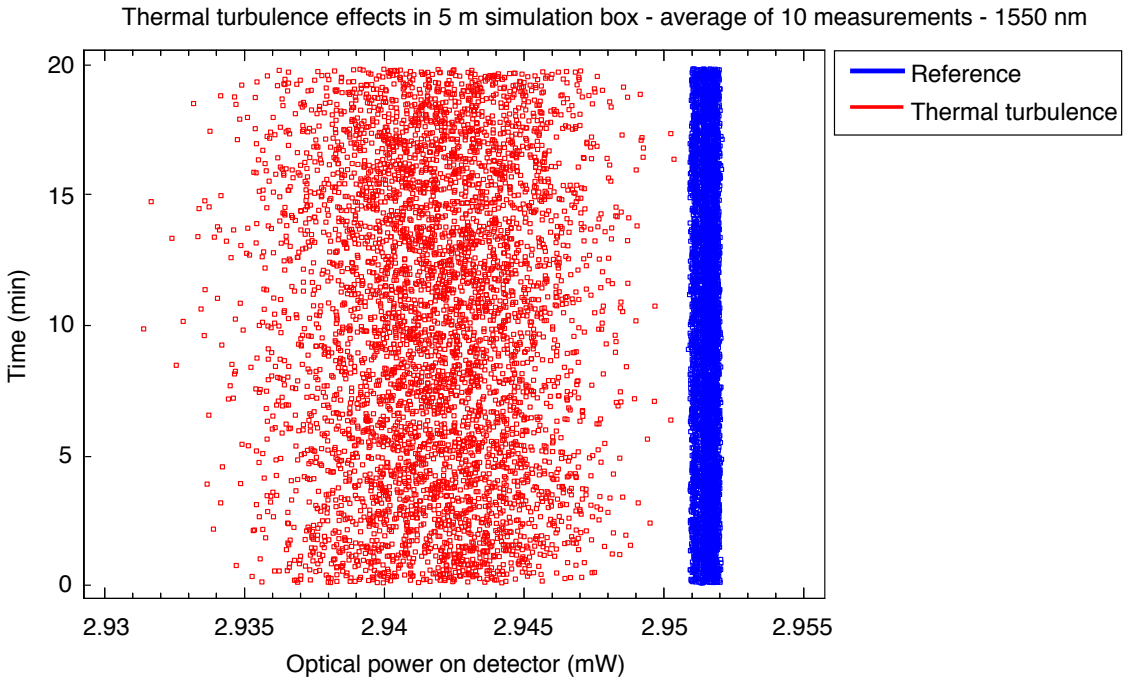

Figure 7.19: Thermal turbulence effects at 1550 nm - 5 m of length.

7.3 Measurement of Fog Effects

For the fog effects measuring simulating box was filled with fog generated by fog machine mentioned above. The schematic layout of measurement is shown in Figure 7.20. For measurements at a distance of 5 m boxes were connected together and sealed into the one uninterrupted box as visible in Figure 7.21. Box was completely closed and filled with fog for 30 seconds. After this time the measurement of optical power on detector was started. To show how fog influences optical power on detector measurement time was set to 60 minutes (with interval 0.25 second). The number of the measurements was 10 for each distance and wavelength as in case of turbulence measurements. The values from these measurements were averaged and processed in MATLAB 2012a. Results were also processed by regression, which is discussed in Chapter 7.3.1.

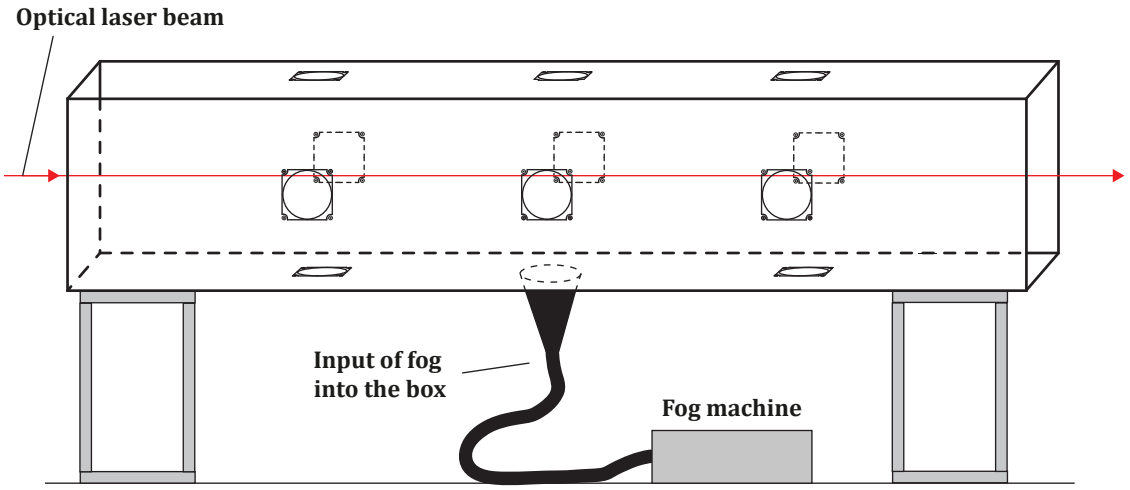

Figure 7.20: Schematic layout for the measurement of fog - 2,5 m.

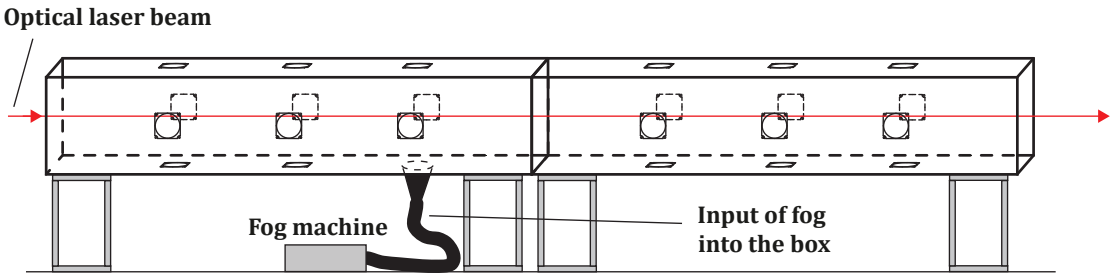

Figure 7.21: Schematic layout for the measurement of fog - 5 m.

Figure 7.22: The simulation box filled with the fog for measurement at distance of 2.5 m.

7.3.1 Used types of regression

Two types of regression were used to determine the probable ideal curve. The first type is linear polynomial regression (approximation), which is special case of linear regression. Coefficients of searched polynomial are calculated by the method of least squares so that the sum of squared deviations from original values was minimal. Polynomial models for curves are given by [19]:

$$y = \sum_{i=1}^{n+1} p_i \cdot x^{n+1-i} \quad , \tag{7.1}$$

where $n+1$ is the order of the polynomial, n is the degree of the polynomial ($1 \leq n \leq 9$). The order gives the number of coefficients to be fit and the degree gives the highest power of the predictor variable. Polynomials can be described in terms of their degree. For example a third-degree polynomial is given by [19]:

$$\gamma = p_1 \cdot x^3 + p_2 \cdot x^2 + p_3 \cdot x + p_4 \ . \tag{7.2}$$

The main advantage of linear polynomial fits includes flexibility for data that is not too complicated. However, the problem can occurs due to outliers. Outliers have a large influence on the fit because of squaring residuals magnifies the effects of these extreme data points. To minimize this problem robust least-squares can be used. In this work regression by bisquare weights method was used. This method minimizes a weight sum of squares where the weight give to each data point depends on how far the point is from fitted line. Robust fitting with bisquare weights uses a reweighted least-squared algorithm, and follows this procedure [19]:

1. Fit the model by weighted least squares.
2. Compute the adjusted residuals and standardize them. The adjusted residuals are given by this equation:

$$r_{adj} = \frac{r_i}{\sqrt{1-h_i}} \quad , \tag{7.3}$$

where r_i are the usual least-squares residuals and h_i are leverages that adjust the residuals by reducing the weight of high-leverage data point, which have a large effect on the least-squares fit. The standardized adjusted residuals are given by:

$$u = \frac{r_{adj}}{K \cdot s} \quad , \tag{7.4}$$

where K is tuning constant ($K = 4.685$) and s is the robust variance.

3. Compute the robust weights as a function of u. The bisquare weights are given by:

$$w_i = \begin{cases} \left(1-\left(u_i\right)^2\right)^2 & |u_i| < 1 \\ 0 & |u_i| \geq 1 \end{cases} \tag{7.5}$$

4. If the fit converges the iteration is done. Otherwise, next iteration from the first step of fitting procedure will be performed [19].

7.3.2 The measurement results

In graphs from Figure 7.23 to Figure 7.28 we can see attenuation caused by fog on all measured wavelengths and distances. Attenuation in most cases decreases with increasing time. This is caused by disintegration and condensation of fog in box. Measured curves were approximate by regression method mentioned above. Because of impossibility to fill box on distance 5 m with the same amount of fog (caused by limitations of fog machine) it was used the same amount as in case of 2.5 m. This caused that attenuation on 5 m is slightly lower than on 2.5 m - on all wavelengths. It is also visible that in 5 m box attenuation decreases in more linear way.

However more interesting results are if we look at dependence on wavelength. After filling the box, the fog dense and sparse areas are mixing for first few minutes. The effect of mixing is more evident in 5 m. We can see in Figure 7.23 and Figure 7.24 that at 632.8 nm is very little effect of mixing fog. At 850 nm is already visible that the attenuation is lower in first minutes especially on 5 m. Essential results are visible at 1550 nm. Due to this mixing of fog attenuation is significantly lower in the first 15 minutes (2.5 m) or rather 20 minutes (5 m) of measurement.

If we look at the values of the maximal attenuation we can see another interesting characteristic. The maximal attenuation at 632.8 nm is very similar to 850 nm. It is about 57 dB on 2.5 m (Figure 7.23 and Figure 7.25) and 54 dB on 5 m (Figure 7.24 and Figure 7.26). But at 1550 nm attenuation is significantly lower, only about 24 dB on 2.5 m and 20 dB on 5 m. (Figure 7.27 and Figure 7.28).

The distance between measured points and regression curve shows us the rate of signal fluctuations. Probability of these fluctuations were calculated using Laplace probability:

$$P(\Delta A) = \frac{m_f}{n_f} \quad , \tag{7.6}$$

where m_f is number of fluctuations in interval and n_f is total number of fluctuations. Each interval was calculated as a deviation measured data from regression curve. The results of these calculations are shown below. In Figure 7.29 (632.8 nm and 2.5 m) we can see that the fluctuations are very small, most in the interval of 0 to 0.1 dB. In Figure 7.30 (632.8 nm and 5 m) the situation is different. Intervals are larger because of more outliers. Other regression type (bisquare) incurs these outliers. We can see that most that about 80% of fluctuations are in the interval of 0 to 1.25 dB. Similar results we can also see in Figure 7.31 and Figure 7.32 (850 nm). In Figure 7.33 and Figure 7.34 is visible that interval are smaller due to used linear polynomial regression (1550 nm).

Another results of fog measurements are graphs of visibility. I. Kim equations (5.7 and 5.9) from Chapter 5.1.4 were used for calculating. According to theoretical bases, two thresholds (2 % and 5 %) of visibility were applied. Calculations were done for both of these thresholds. In Figure 7.35 and Figure 7.36 are visible results for 632.8 nm. These results show atmospheric visibility in the box during measurements. For other wavelengths graphs are shown

below, 850 nm - Figure 7.37, Figure 7.38 and 1550 nm - Figure 7.39 Figure 7.40. We can notice that also in these graphs is demonstrated the effect of fog mixing. This effect is observable in distance of 5 m on all wavelengths.

Table 7.5 shows the atmospheric conditions during the measurement for each wavelength and distance. In Table 7.6 is shown regression order, polynomial models and R-square for each wavelength and distance. Coefficients of used models are as a part of Appendix A and they are visible in Table A.2. The R-Square is a parameter indicates how close the regression curve to real data values is. When the R-Square value is 1 model is consistent with the data. All data were processed using MATLAB 2012a.

Table 7.5: Conditions of fog measurement.

Wavelength	Simulated Distance	Temperature	Pressure	Humidity
632.8 nm	2.5 m	21.41 °C	1006.06 hPa	57.9 %
632.8 nm	5.0 m	22.1 °C	980.9 hPa	32.7 %
850.0 nm	2.5 m	22.0 °C	978.2 hPa	34.5 %
850.0 nm	5.0 m	22.1 °C	980.9 hPa	32.7 %
1550.0 nm	2.5 m	23.2 °C	994.7 hPa	40.4 %
1550.0 nm	5.0 m	22.1 °C	980.9 hPa	32.7 %

Table 7.6: Regression order, used polynomial models and R-Square.

Wavelength	Distance	Order	Used polynomial model	R-Square
632.8 nm	2.5 m	7^{th}	$f(x) = p_1 \cdot x^7 + p_2 \cdot x^6 + p_3 \cdot x^5 + p_4 \cdot x^4 + p_5 \cdot x^3 + p_6 \cdot x^2 + p_7 \cdot x + p_8$	0.9999
632.8 nm	5.0 m	6^{th}	$f(x) = p_1 \cdot x^6 + p_2 \cdot x^5 + p_3 \cdot x^4 + p_4 \cdot x^3 + p_5 \cdot x^2 + p_6 \cdot x + p_7$	0.9997
850.0 nm	2.5 m	4^{th}	$f(x) = p_1 \cdot x^4 + p_2 \cdot x^3 + p_3 \cdot x^2 + p_4 \cdot x + p_5$	0.9997
850.0 nm	5.0 m	5^{th}	$f(x) = p_1 \cdot x^5 + p_2 \cdot x^4 + p_3 \cdot x^3 + p_4 \cdot x^2 + p_5 \cdot x + p_6$	0.9996
1550.0 nm	2.5 m	6^{th}	$f(x) = p_1 \cdot x^6 + p_2 \cdot x^5 + p_3 \cdot x^4 + p_4 \cdot x^3 + p_5 \cdot x^2 + p_6 \cdot x + p_7$	0.9983
1550.0 nm	5.0 m	3^{rd}	$f(x) = p_1 \cdot x^3 + p_2 \cdot x^2 + p_3 \cdot x + p_4$	0.9835

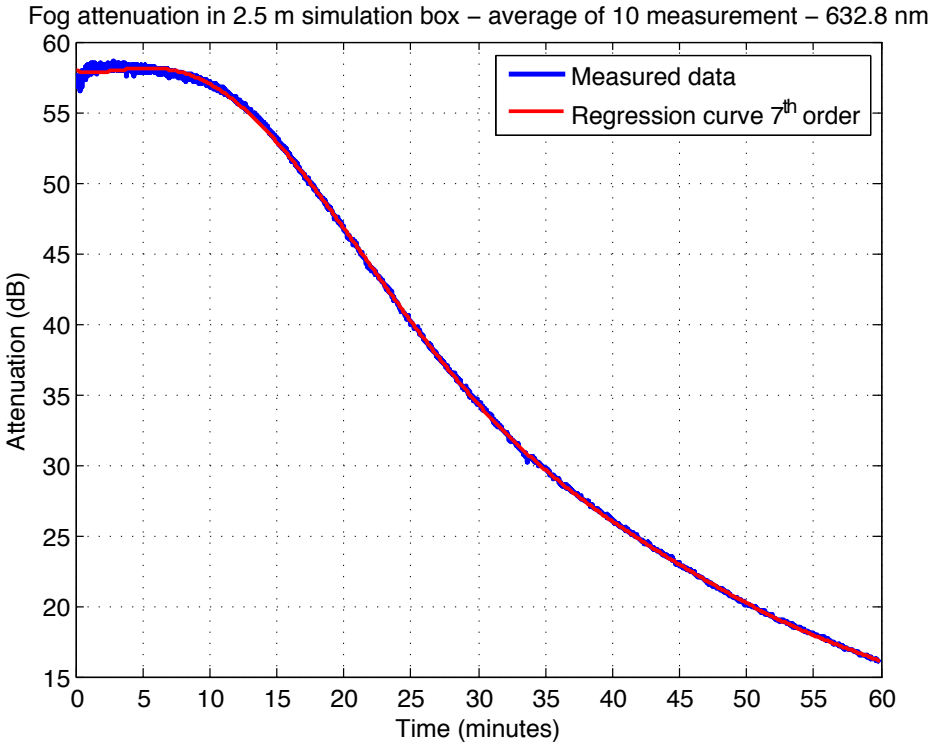

Figure 7.23: Attenuation of fog at 632.8 nm - 2.5 m of length.

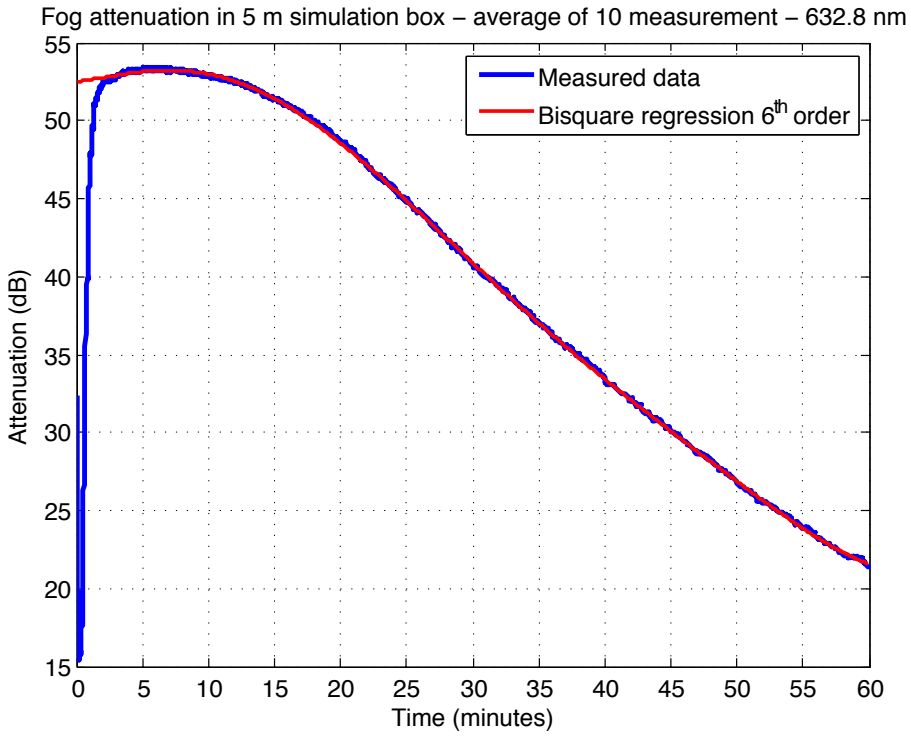

Figure 7.24: Attenuation of fog at 632.8 nm - 5 m of length.

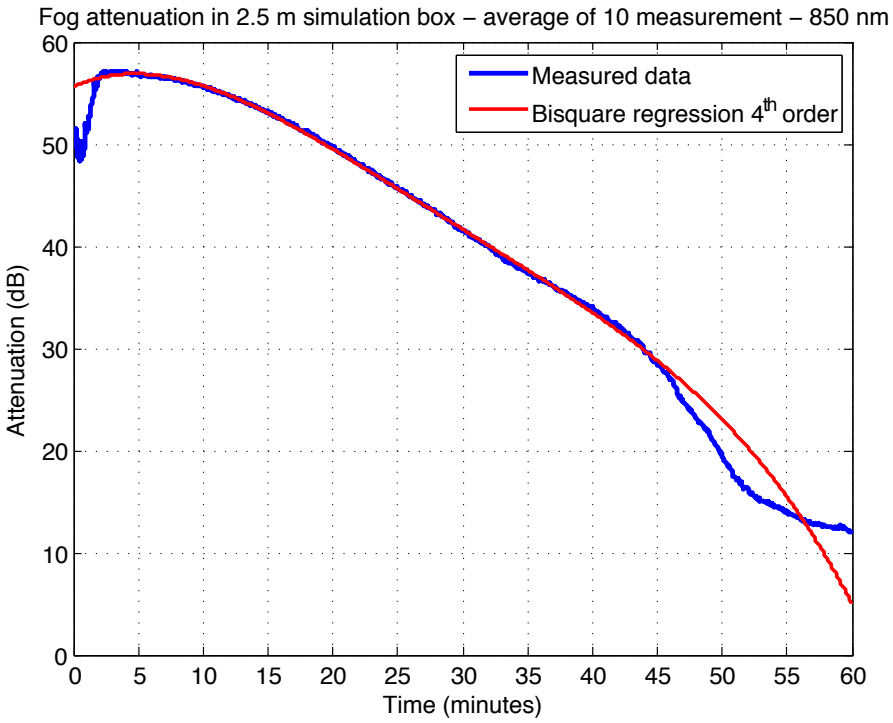

Figure 7.25: Attenuation of fog at 850 nm - 2.5 m of length.

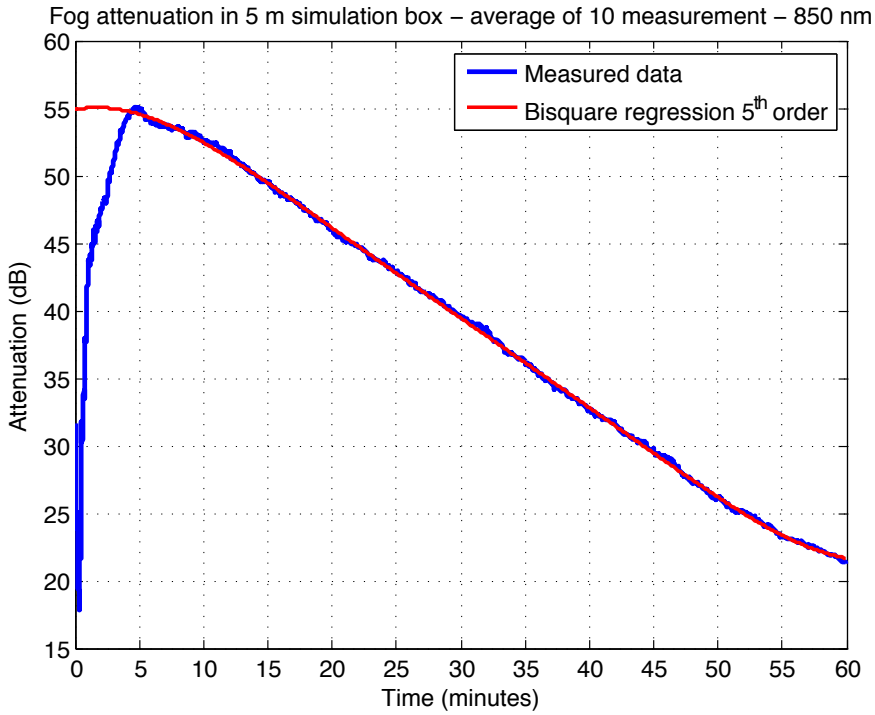

Figure 7.26: Attenuation of fog at 850 nm - 5 m of length.

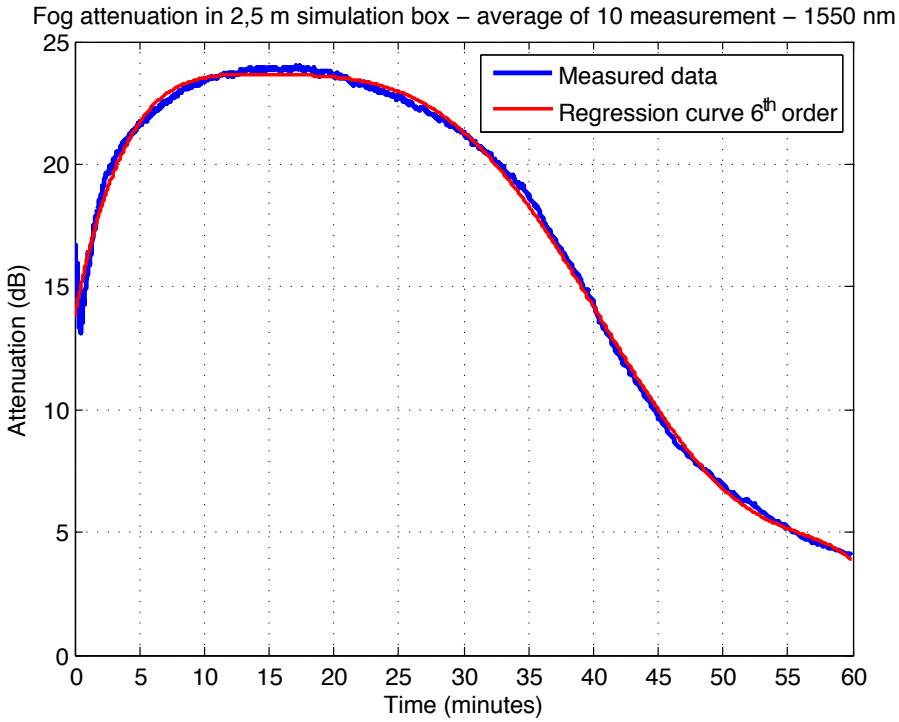

Figure 7.27: Attenuation of fog at 1550 nm - 2.5 m of length.

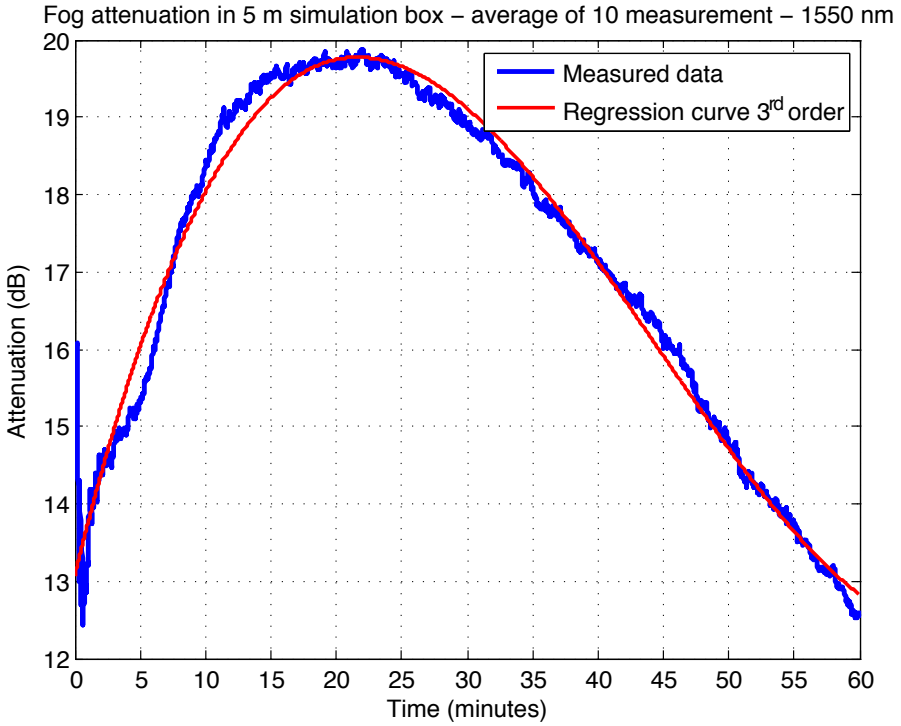

Figure 7.28: Attenuation of fog at 1550 nm - 5 m of length.

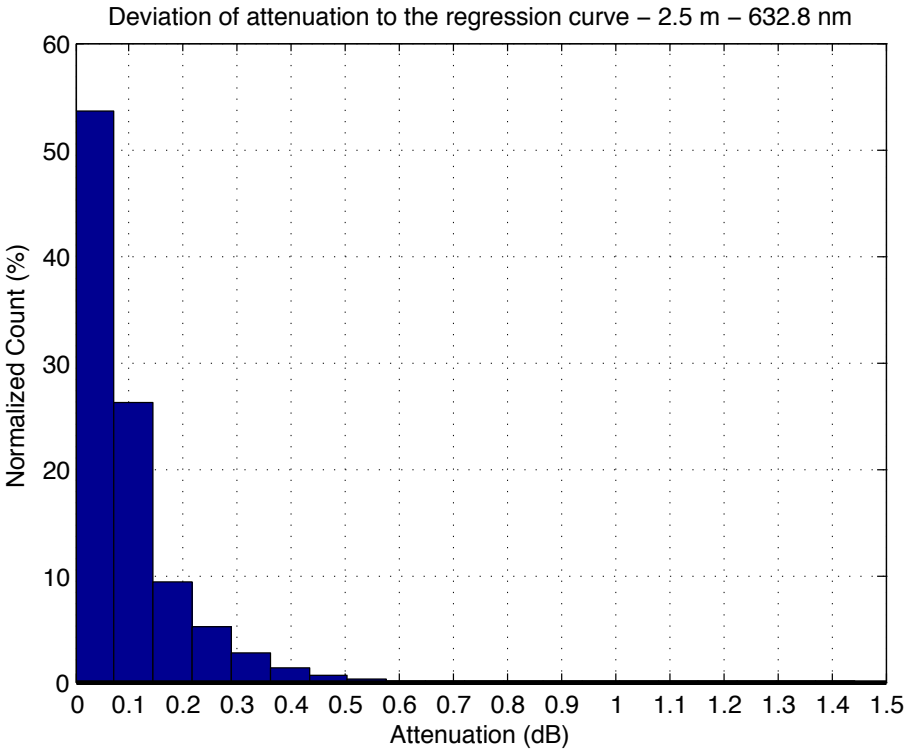

Figure 7.29: Deviation of attenuation at 632.8 nm - 2.5 m of length.

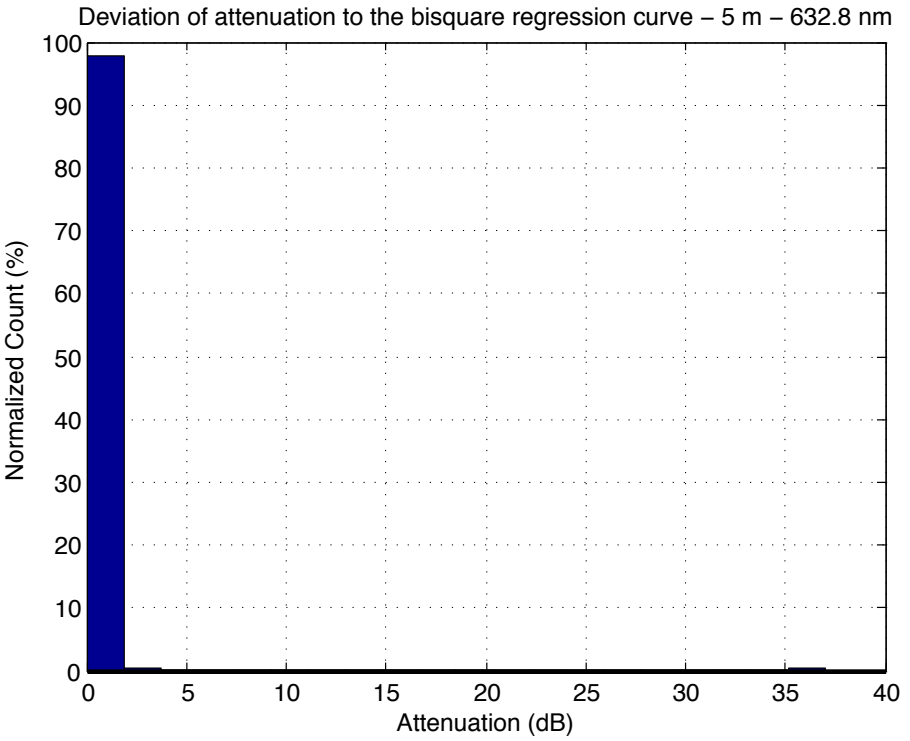

Figure 7.30: Deviation of attenuation at 632.8 nm - 5 m of length.

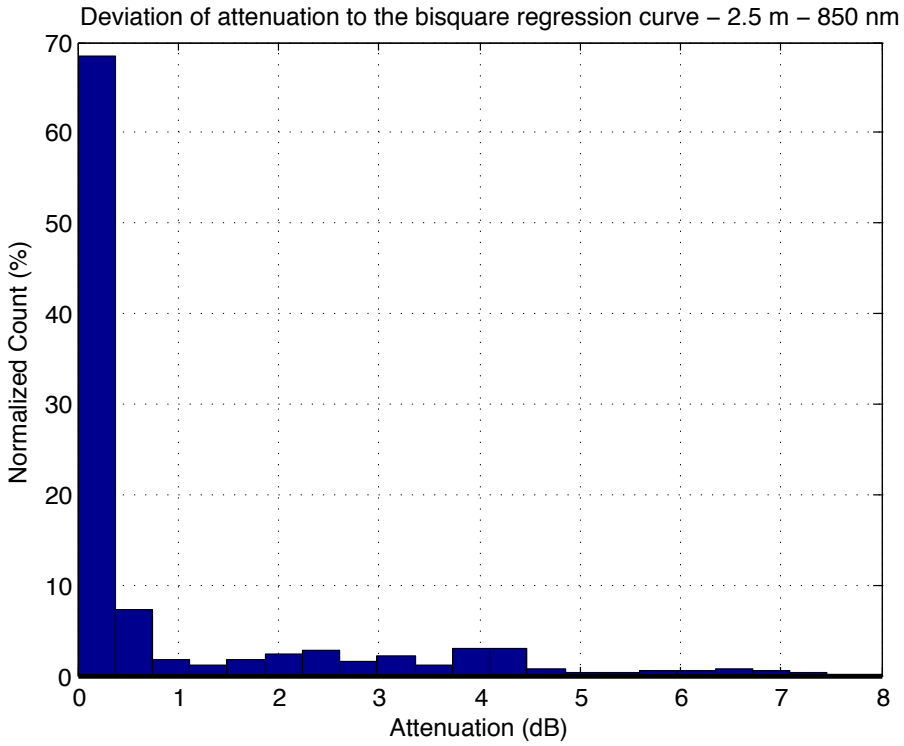

Figure 7.31: Deviation of attenuation at 850 nm - 2.5 m of length.

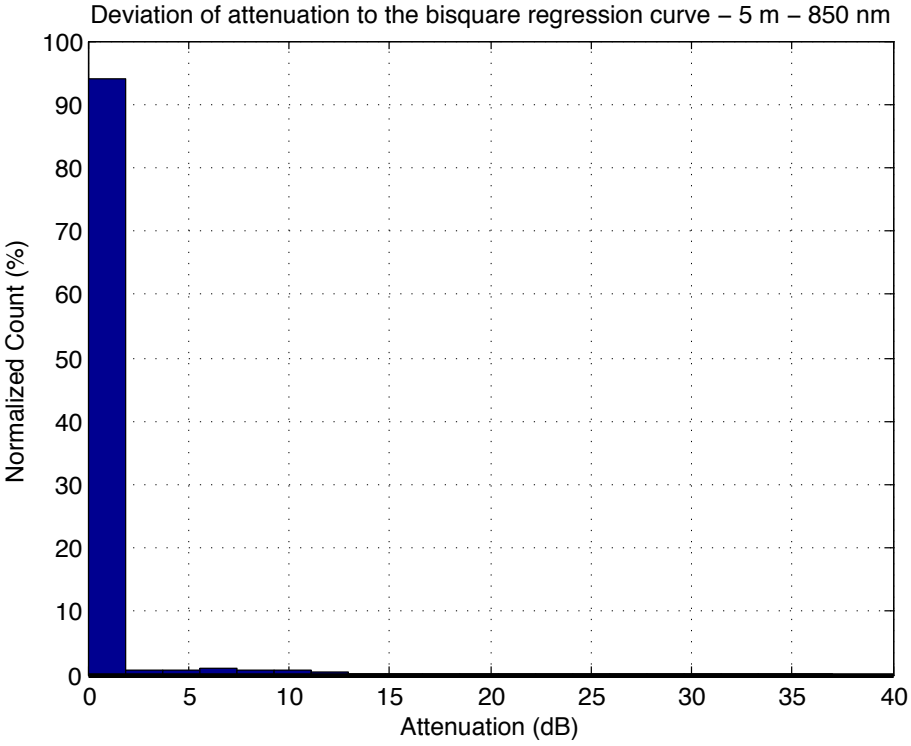

Figure 7.32: Deviation of attenuation at 850 nm - 5 m of length.

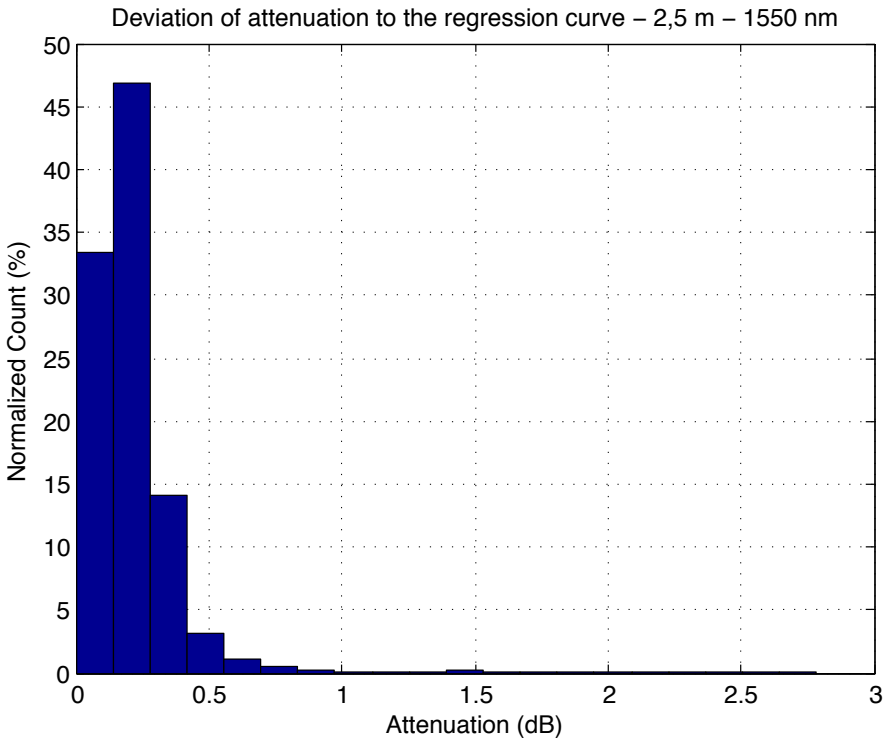

Figure 7.33: Deviation of attenuation at 1550 nm - 2.5 m of length.

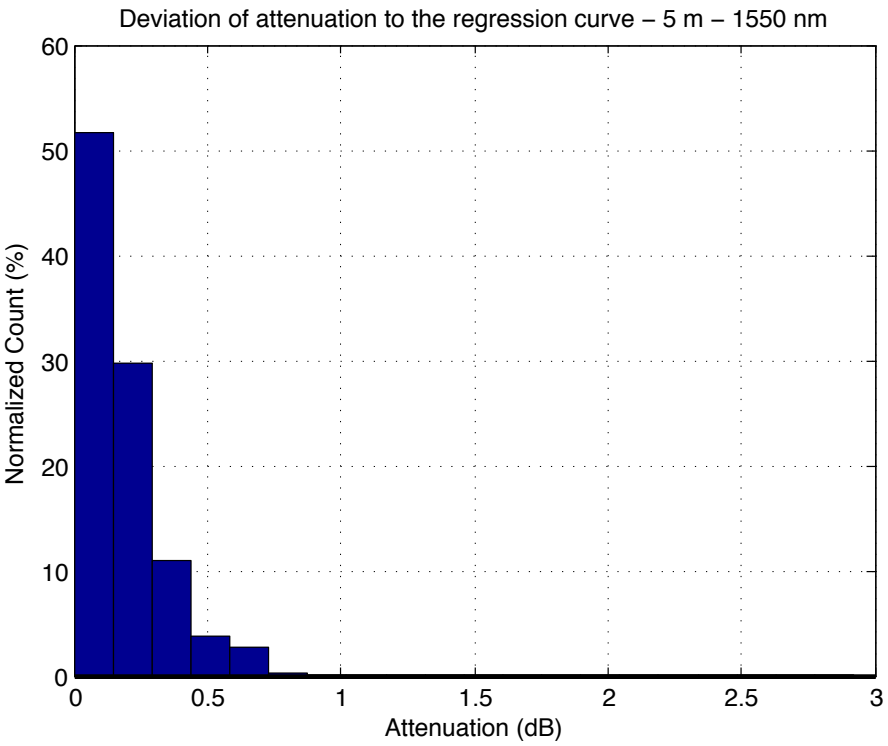

Figure 7.34: Deviation of attenuation at 1550 nm - 5 m of length.

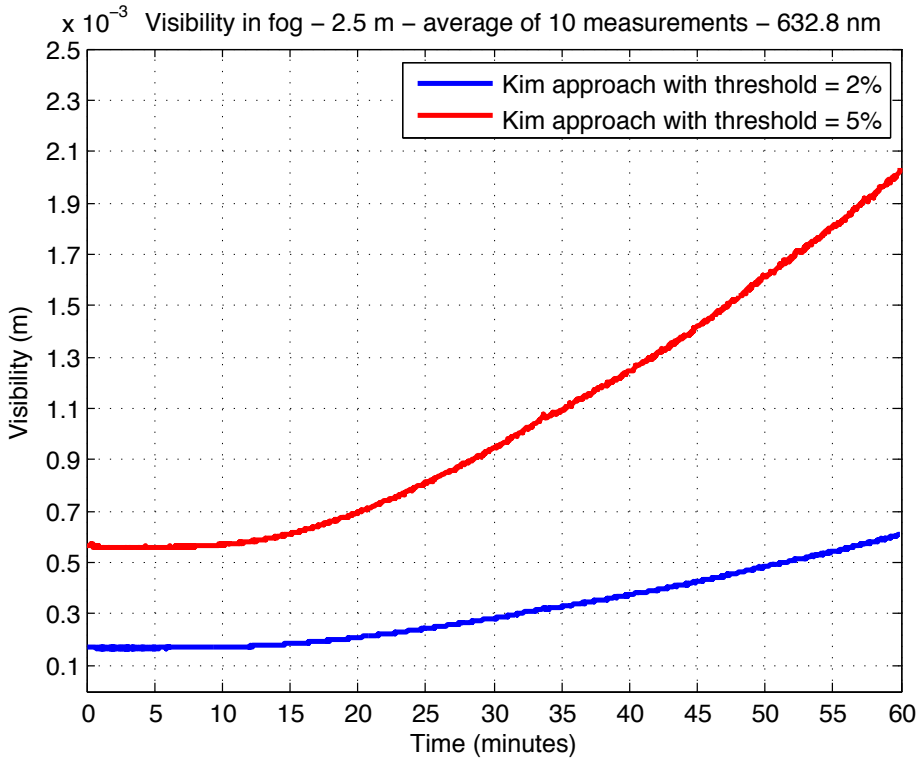

Figure 7.35: Atmospheric visibility in fog at 632.8 nm - 2.5 m of length.

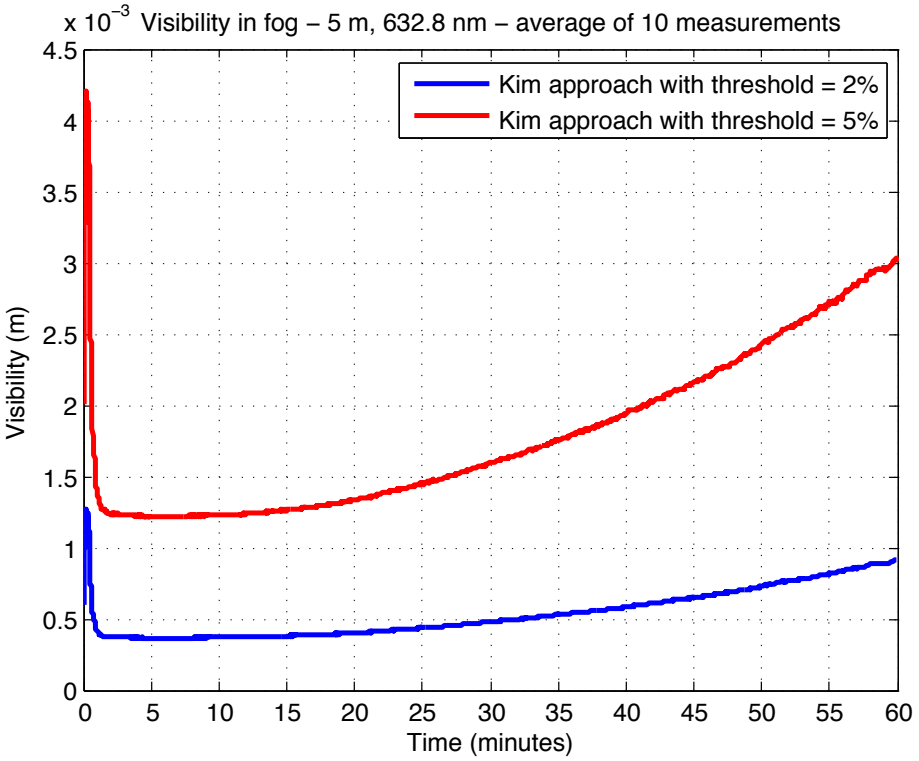

Figure 7.36: Atmospheric visibility in fog at 632.8 nm - 5 m of length.

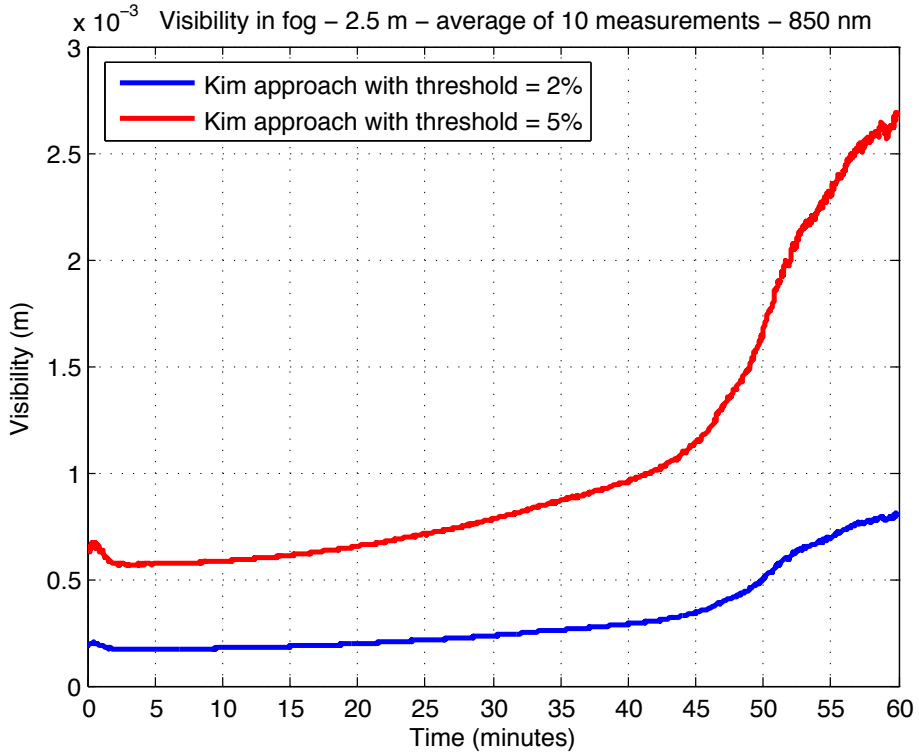

Figure 7.37: Atmospheric visibility in fog at 850 nm - 2.5 m of length.

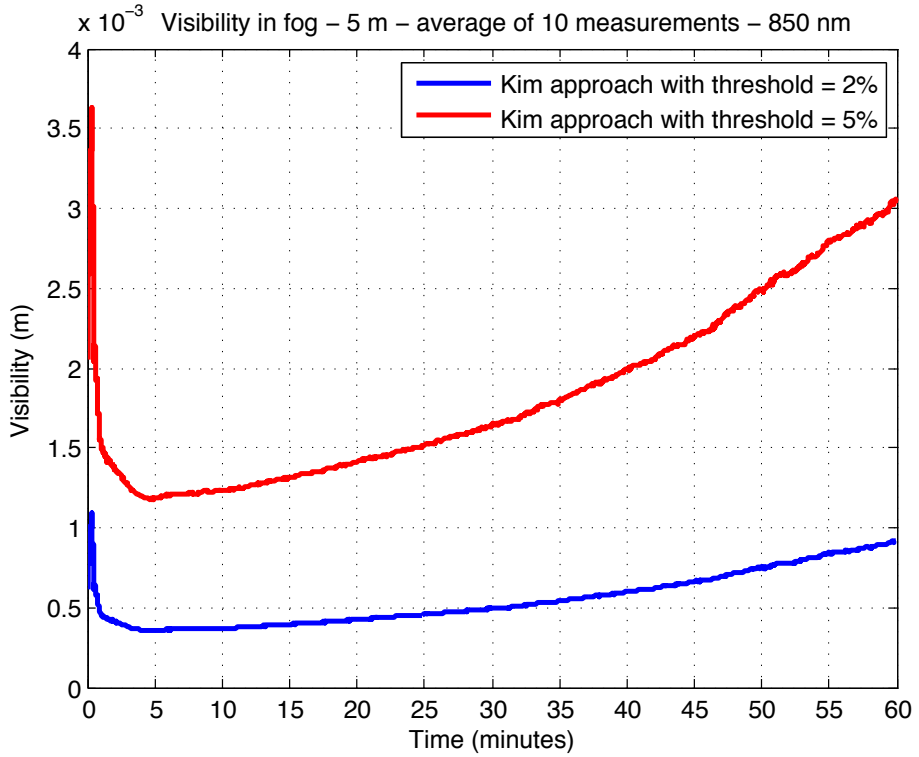

Figure 7.38: Atmospheric visibility in fog at 850 nm - 5 m of length.

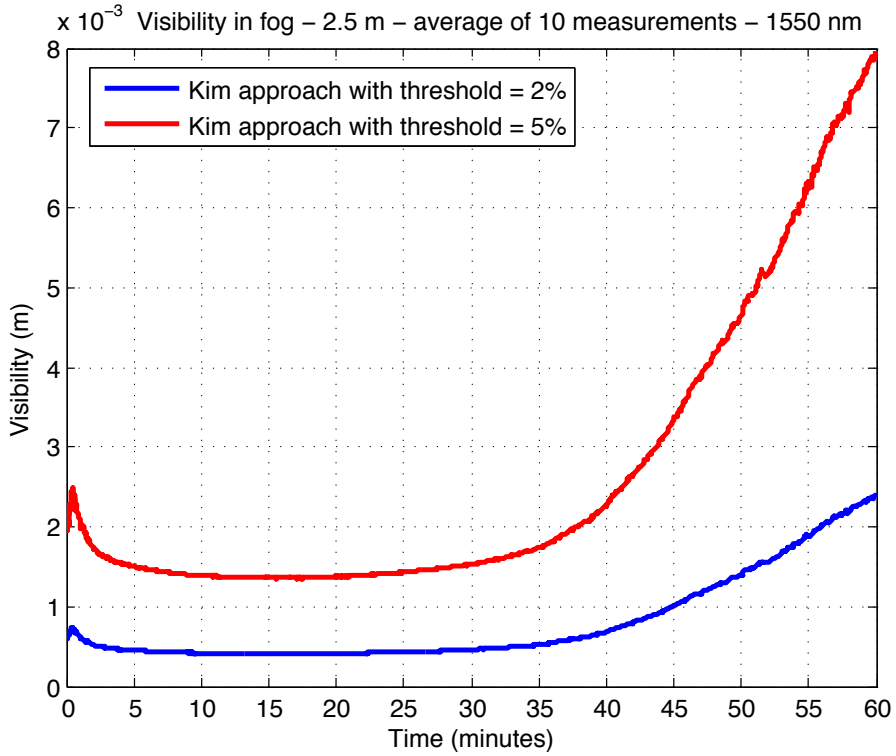

Figure 7.39: Atmospheric visibility in fog at 1550 nm - 2.5 m of length.

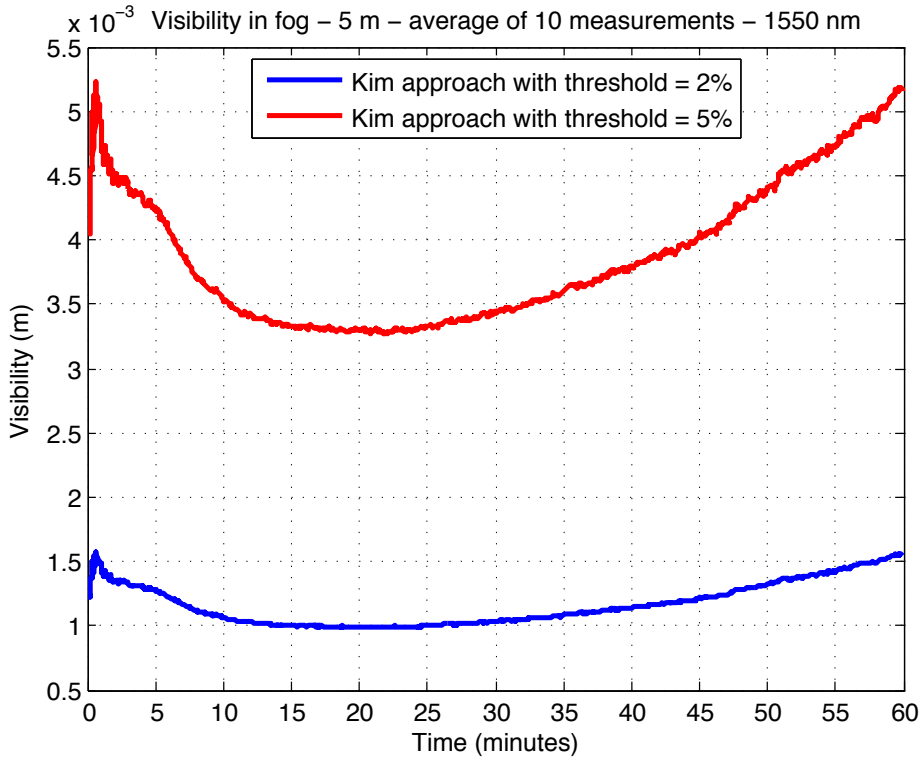

Figure 7.40: Atmospheric visibility in fog at 1550 nm - 5 m of length.

8 Simulation

The task of the simulation part of this work was to simulate atmospheric conditions that were measured in the previous chapter. For this task, simulation software Optiwave OptiSystem 11 was assigned to use. This simulation tool is designed especially for optical fiber systems. However this brings limitations in terms of simulation of atmospheric effects. To create free space optics link special component "FSO Channel" is available. This component determines the settings of whole atmospheric environment.

For simulation effects of turbulent environment there is a possibility of settings structural parameter of refractive index (Figure 8.1). After series of attempts to simulate turbulent environment it was found that software is not possible to simulate this type of environment because of substantial bugs in this software. Software showed obviously wrong values of output optical power (often greater than the value of the input optical power). This error occurred at all tested simulations and for this reason was simulated only part of the effects of fog.

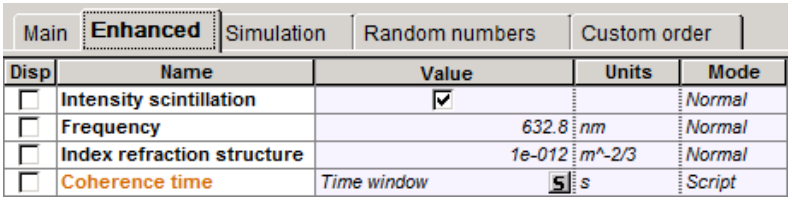

Figure 8.1: Settings of intensity scintillation in OptiSystem 11.

8.1 Simulation of Fog Effects

The task of fog effects simulation was to determine how the connections that were tested in simulation box behaved in terms of BER (Bit Error Rate) and other quality parameters.

Schematic diagram used for simulation is shown in Figure 8.2. On the left side is the optical transmitter where wavelength, optical power and modulation were set. Modulation type was set to NRZ. All wavelength and the same optical power measured in Chapter 7.3 were simulated - 632.8 nm (15 mW), 850 nm (5 mW) and 1550 nm (5 mW). To see input optical power for FSO channel optical power meter was connected to the transmitter. The following component of schematic diagram is the FSO Channel. This component was set to 2.5 m or 5 m of range. The conditions of fog were simulated using data of attenuation measured in Chapter 7.3.2. Attenuation created by fog in the box had to be converted to attenuation per km (Table 8.1). These data of attenuation were iterated in FSO component. In order to measure optical power reduced by FSO channel another optical power meter is used. The optical receiver with PIN photodetector is placed on the output of FSO channel. The last component is eye diagram analyzer that gives us information about eye diagram, BER and Q-Factor. Parameters that were not mentioned were left at the default value.

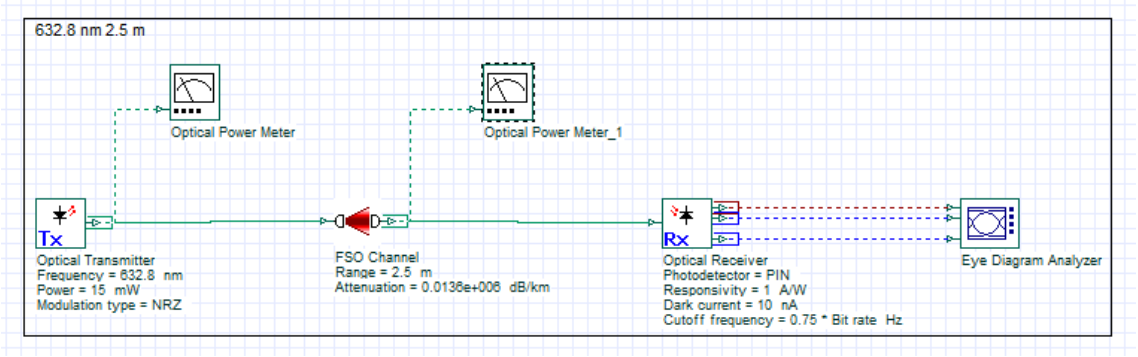

Figure 8.2: Schematic diagram for simulation of fog at 632.8 nm and 2.5 m in OptiSystem 11.

Table 8.1: Converted attenuation per km used for simulation of fog in OptiSystem 11.

Wavelength	**632.8 nm**		**850.0 nm**		**1550.0 nm**	
Distance	**2.5 m**	**5.0 m**	**2.5 m**	**5.0 m**	**2.5 m**	**5.0 m**
Time	**Attenuation (dB ·km^{-1})**					
0 min.	23000	10500	22400	11000	5600	2600
5 min.	23200	10600	22800	10900	8800	3200
10 min.	22800	10540	22400	10500	9200	3600
15 min.	21000	10400	21600	9900	9280	3840
20 min.	18800	9600	20000	9200	9200	3960
25 min.	16000	9000	18400	8600	9000	3940
30 min.	13600	8100	16600	7900	8400	3820
35 min.	12000	7400	15200	7200	7200	3640
40 min.	10400	6700	13400	6500	5600	3420
45 min.	9400	6000	11400	5900	4000	3380
50 min.	8000	5400	9200	5200	2800	2940
55 min.	7000	4800	6200	4600	2080	2720
60 min.	6400	4400	2000	4300	1600	2580

8.2 Simulation Results

According to the BER values we can determine if the connection work reliably under the circumstances. Value of BER should be lower than the range from 10^{-7} to 10^{-12} for the correct transmission. In Table 8.2 we can see BER results obtained by simulation in OptiSystem 11. Additional results are the eye diagrams for all wavelength, distances of link and times of measurements. For the presentation of results have been selected essential eye diagrams only.

From Table 8.2 we see that the connection at wavelength of 632.8 nm and distance of 5 m in the first minutes does not work correctly, because the BER is equal to 1. Eye diagram for 0 minute of simulation is shown in Figure 8.3. In the 25 minute, BER parameter is improved to an acceptable value and the connection starts work reliably (Figure 8.4). In the following minutes we see improving BER parameter to zero indicating zero bit errors. The connection works reliably from 25 minute to end of the measurement - 60 minute (Figure 8.5). A similar situation occurs at the same wavelength at a distance of 5 m. Eye diagram for 0 minute of simulation is shown in Figure 8.6 We can see that this eye diagram is completely broken. The connection does not work properly until the 45 minute (Figure 8.7). Graph of eye diagram for 60 minute is shown in Figure 8.9. Quality of this eye diagram is good but still worse than at the distance of 2.5 m.

The same situation is also at 850 nm in case of 2.5 m. In Figure 8.9 we can see that the connection does not work reliably from 0 minute and the eye diagram is broken. Connection starts work at 50 minute (Figure 8.10). At 60 minute in Figure 8.11 the eye diagram is very clear. At distance of 5 m in 0 minute eye diagram is probably the worst of all simulated diagrams - Figure 8.12. The connection starts work reliably even in 55 minute - Figure 8.13. At 60 minute, graph is very similar to 55 minute (Figure 8.14).

We can find an interesting result again in case of the laser source at 1550 nm. From Table 8.2 we can see that the connection works reliably during the whole measurement for both distances. At distance of 2.5 m in 0 minute, the eye diagram is very clear compared to other wavelengths (Figure 8.15). The critical time of this distance was 15 minute. In this time the BER parameter was highest but still not overcome the unreliability boundary (Figure 8.16). In 60 we can see very clear diagram in Figure 8.17. At the distance of 5 m differences between each diagrams are smaller compared to results on 2.5 m. Time with the highest BER parameter is 20 minute but the connection was still reliably (Figure 8.19). The eye diagram for 0 minute is shown in Figure 8.18 and for 60 minute in Figure 8.20.

The third parameter that was to obtain by simulations is the quality parameter - Q Factor which gives us information about quality of signal with respect to distance of the signal from the noise. Q Factor is closely dependent on the BER value. Values of Q Factor obtained by simulation are visible in Table 8.3.

From these results we can confirm assumption of the measurement results, that the 1550 nm is least affected by fog effects. Values of optical power simulated on the output of FSO Channel are in Table A.1, which is part of Appendix A.

Table 8.2: Bit Error Rate obtained by simulation of fog in OptiSystem 11.

Wavelength	**632.8 nm**		**850.0 nm**		**1550.0 nm**	
Distance	**2.5 m**	**5.0 m**	**2.5 m**	**5.0 m**	**2.5 m**	**5.0 m**
Time	**Bit Error Rate**					
0 min.	1,0	1,0	1,0	1,0	0,0	0,0
5 min.	1,0	1,0	1,0	1,0	$8,4E^{-33}$	0,0
10 min.	1,0	1,0	1,0	1,0	$1,9E^{-21}$	$2,8E^{-167}$
15 min.	1,0	1,0	1,0	1,0	$1,0E^{-19}$	$6,9E^{-101}$
20 min.	1,0	1,0	1,0	1,0	$1,9E^{-21}$	$3,9E^{-78}$
25 min.	$2,5E^{-13}$	1,0	1,0	1,0	$1,7E^{-26}$	$1,5E^{-181}$
30 min.	$8,1E^{-168}$	1,0	1,0	1,0	$1,1E^{-50}$	$2,9E^{-105}$
35 min.	0,0	1,0	1,0	1,0	$6,5E^{-188}$	$7,2E^{-154}$
40 min.	0,0	$57E^{-3}$	1,0	1,0	0,0	$2,4E^{-242}$
45 min.	0,0	$2,1E^{-08}$	$4,2E^{-3}$	1,0	0,0	$9,0E^{-263}$
50 min.	0,0	$1,0E^{-26}$	$5,4E^{-20}$	$5,1E^{-07}$	0,0	0,0
55 min.	0,0	$2,2E^{-96}$	0,0	$1,2E^{-22}$	0,0	0,0
60 min.	0,0	$1,8E^{-232}$	0,0	$5,2E^{-43}$	0,0	0,0

Table 8.3: Q Factor obtained by simulation of fog in OptiSystem 11.

Wavelength	**632.8 nm**		**850.0 nm**		**1550.0 nm**	
Distance	**2.5 m**	**5.0 m**	**2.5 m**	**5.0 m**	**2.5 m**	**5.0 m**
Time	**Q Factor**					
0 min.	0,0	0,0	0,0	0,0	69,4	79,0
5 min.	0,0	0,0	0,0	0,0	11,9	41,4
10 min.	0,0	0,0	0,0	0,0	9,4	27,5
15 min.	0,0	0,0	0,0	0,0	9,0	21,3
20 min.	0,0	0,0	0,0	0,0	9,4	18,7
25 min.	7,2	0,0	0,0	0,0	10,9	19,1
30 min.	27,6	0,0	0,0	0,0	14,9	21,8
35 min.	65,8	1,0	0,0	0,0	29,2	26,4
40 min.	149,7	2,5	0,0	0,0	69,4	33,2
45 min.	241,4	5,5	2,6	0,0	155,9	34,6
50 min.	442,3	10,6	9,1	4,9	262,3	54,9
55 min.	644,3	20,8	48,3	9,7	352,3	69,5
60 min.	788,0	32,5	378,0	13,7	423,2	80,7

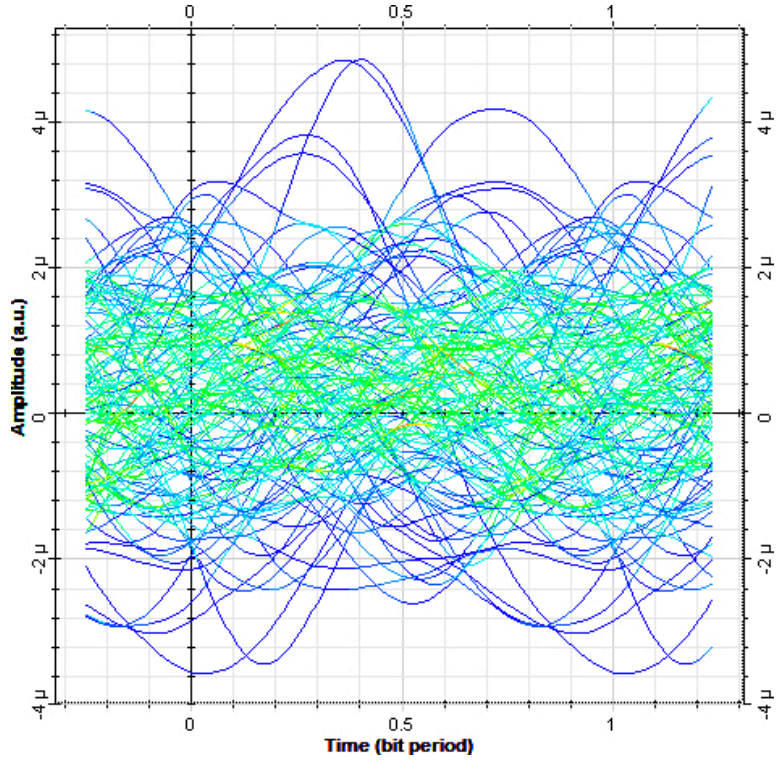

Figure 8.3: Eye diagram of fog simulation at 632.8 nm and 2.5 m - 0 minute.

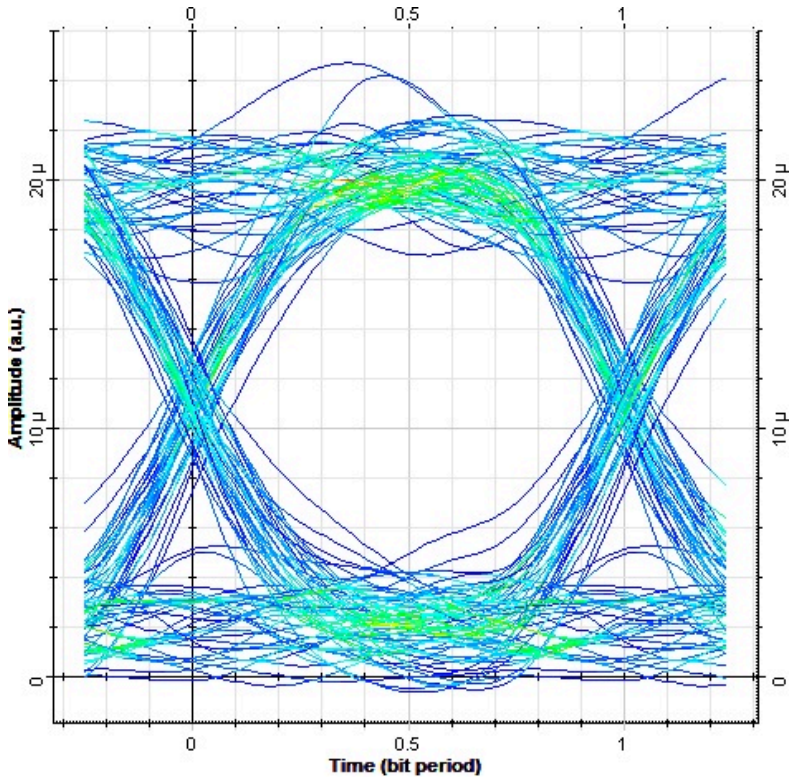

Figure 8.4: Eye diagram of fog simulation at 632.8 nm and 2.5 m - 25 minute.

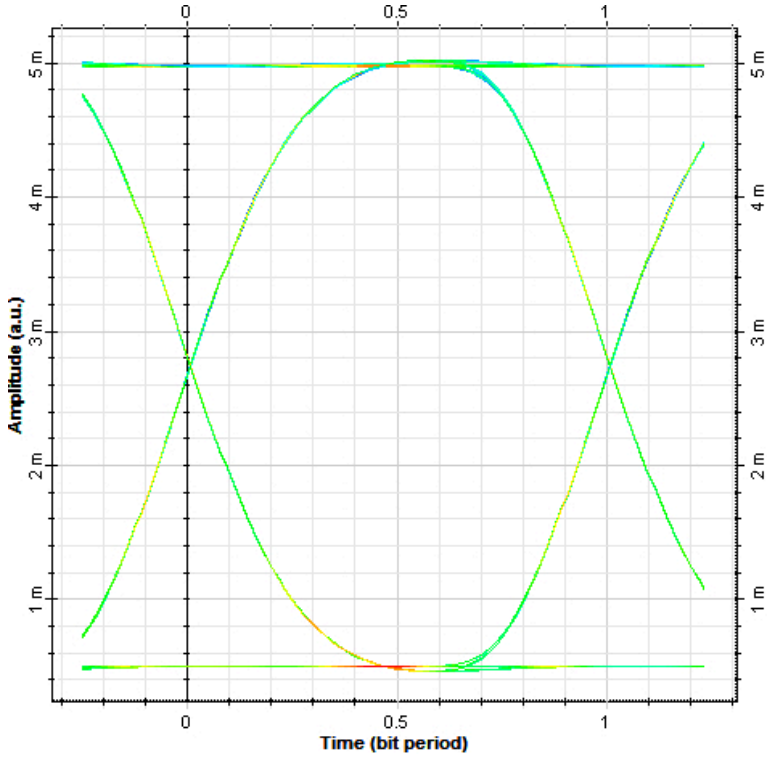

Figure 8.5: Eye diagram of fog simulation at 632.8 nm and 2.5 m - 60 minute.

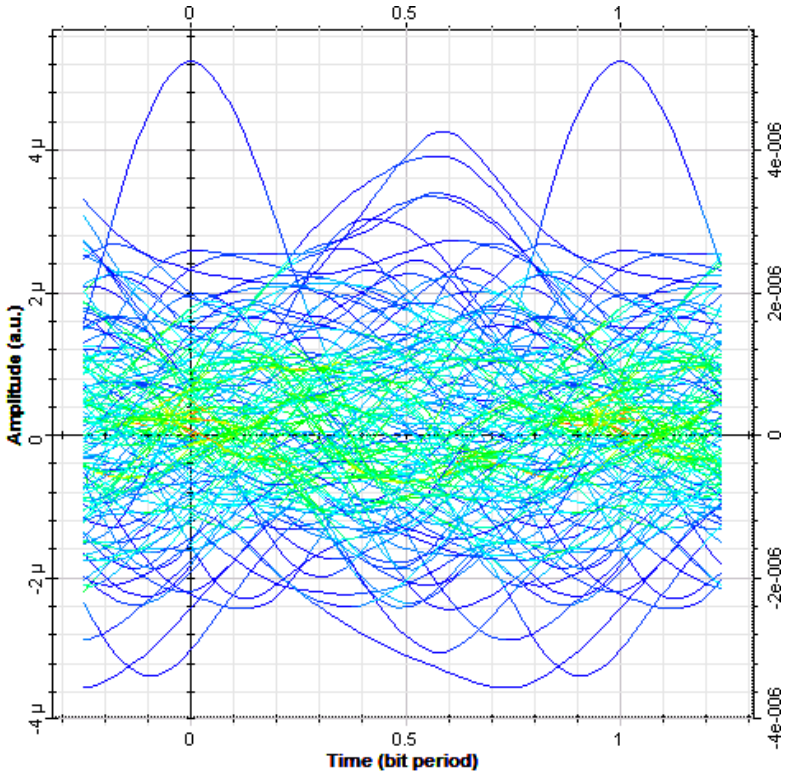

Figure 8.6: Eye diagram of fog simulation at 632.8 nm and 5 m - 0 minute.

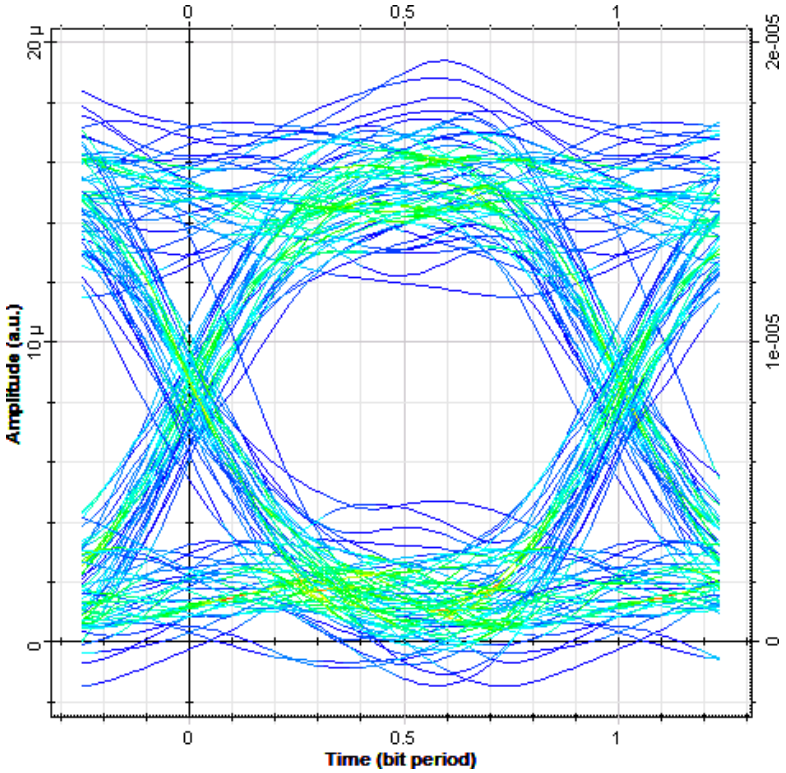

Figure 8.7: Eye diagram of fog simulation at 632.8 nm and 5 m - 45 minute.

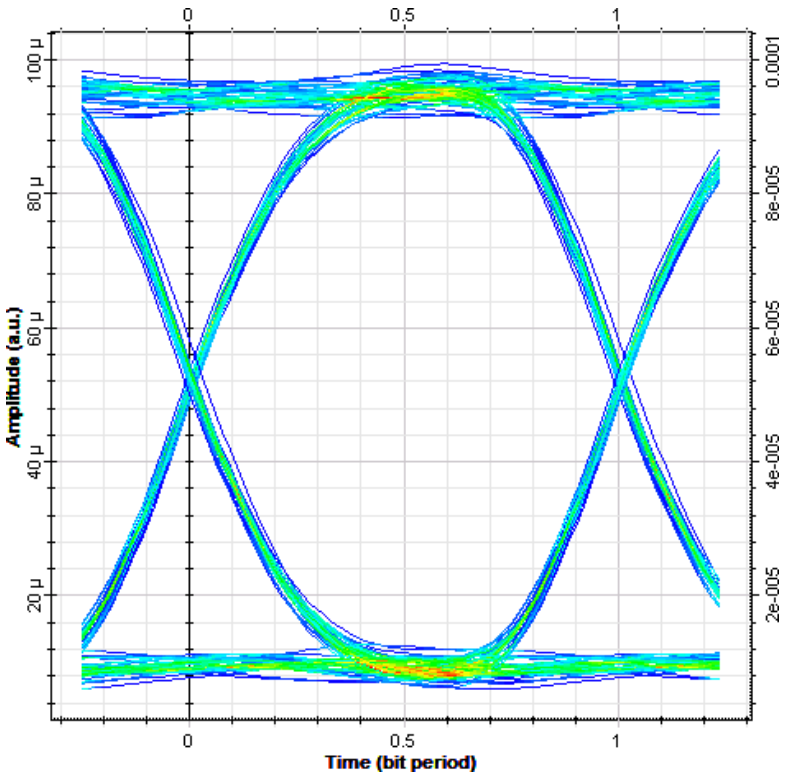

Figure 8.8: Eye diagram of fog simulation at 632.8 nm and 5 m - 60 minute.

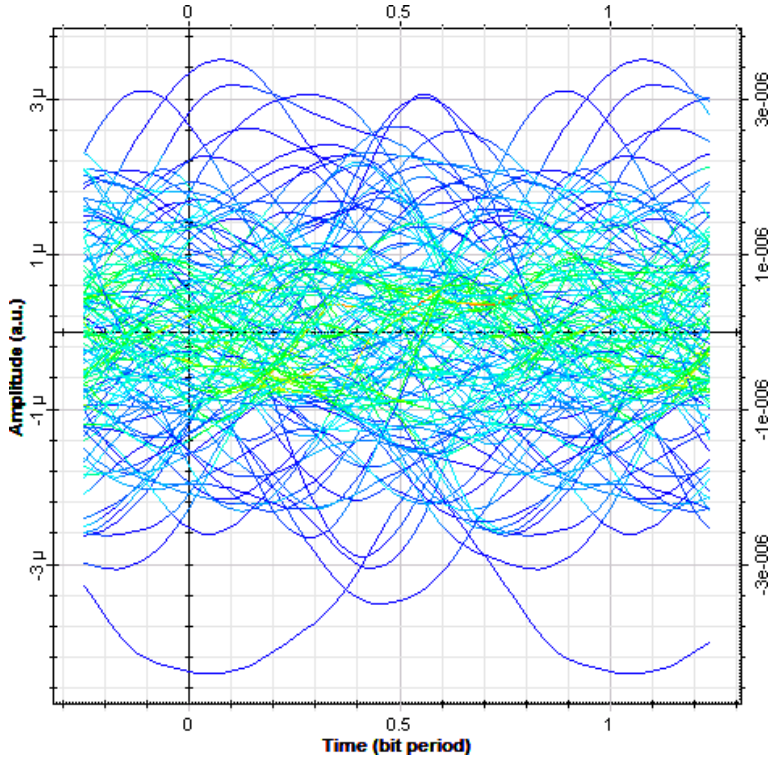

Figure 8.9: Eye diagram of fog simulation at 850 nm and 2.5 m - 0 minute.

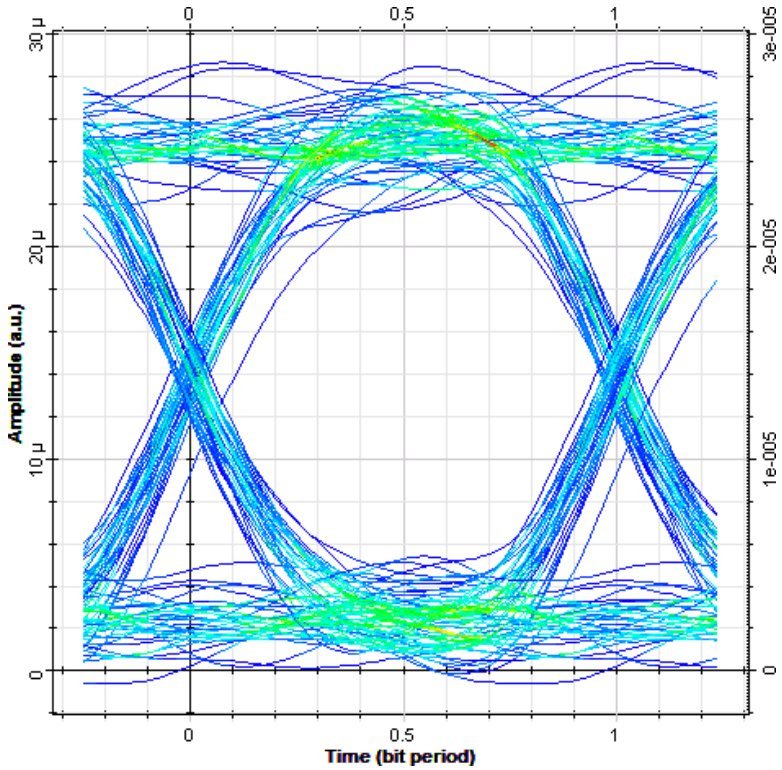

Figure 8.10: Eye diagram of fog simulation at 850 nm and 2.5 m - 50 minute.

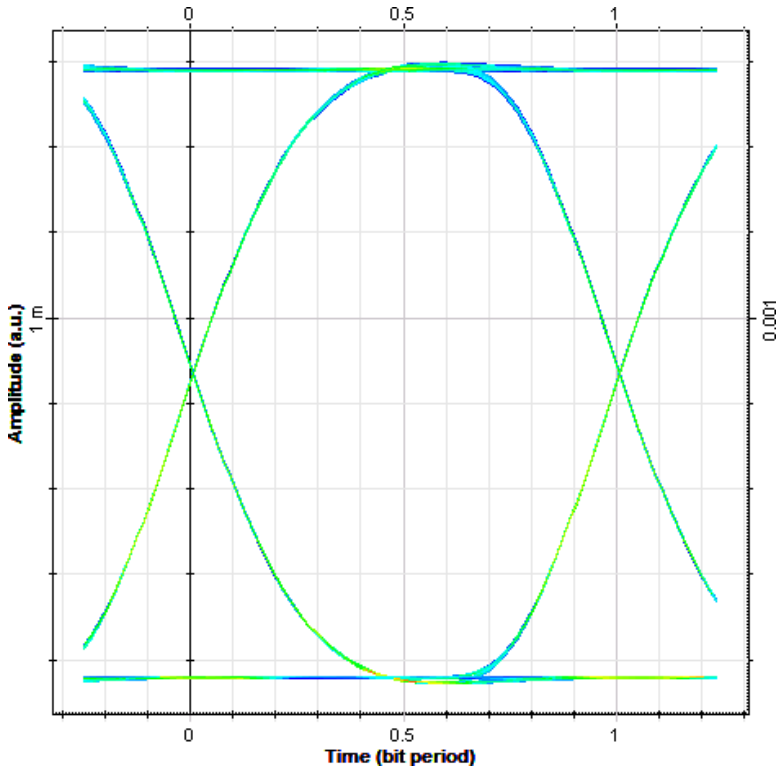

Figure 8.11: Eye diagram of fog simulation at 850 nm and 2.5 m - 60 minute.

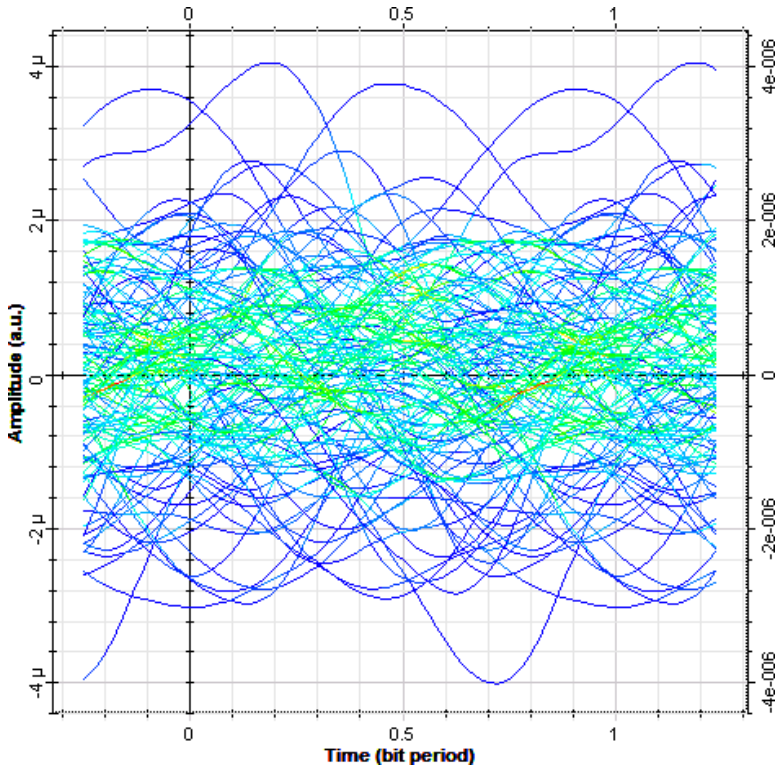

Figure 8.12: Eye diagram of fog simulation at 850 nm and 5 m - 0 minute.

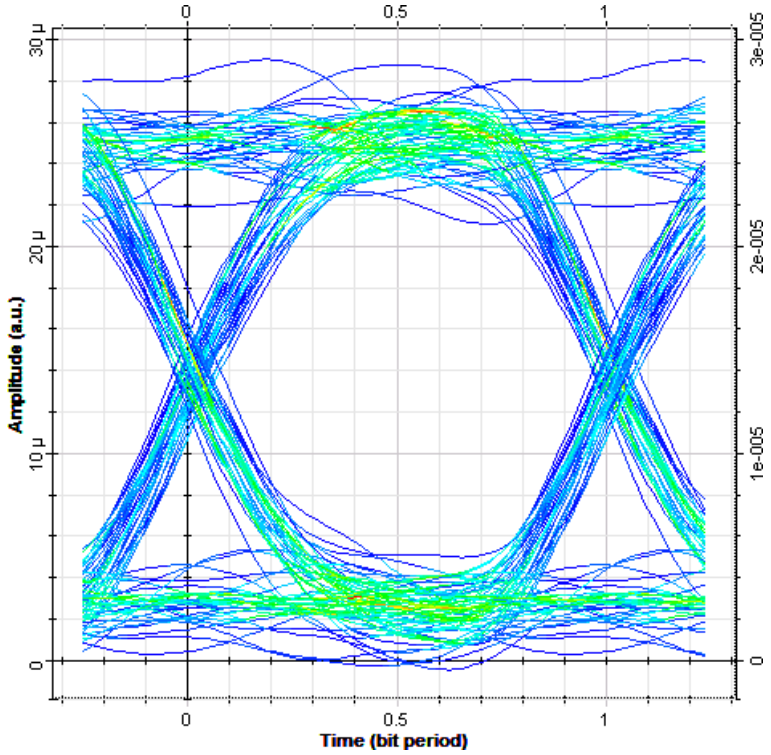

Figure 8.13: Eye diagram of fog simulation at 850 nm and 5 m - 55 minute.

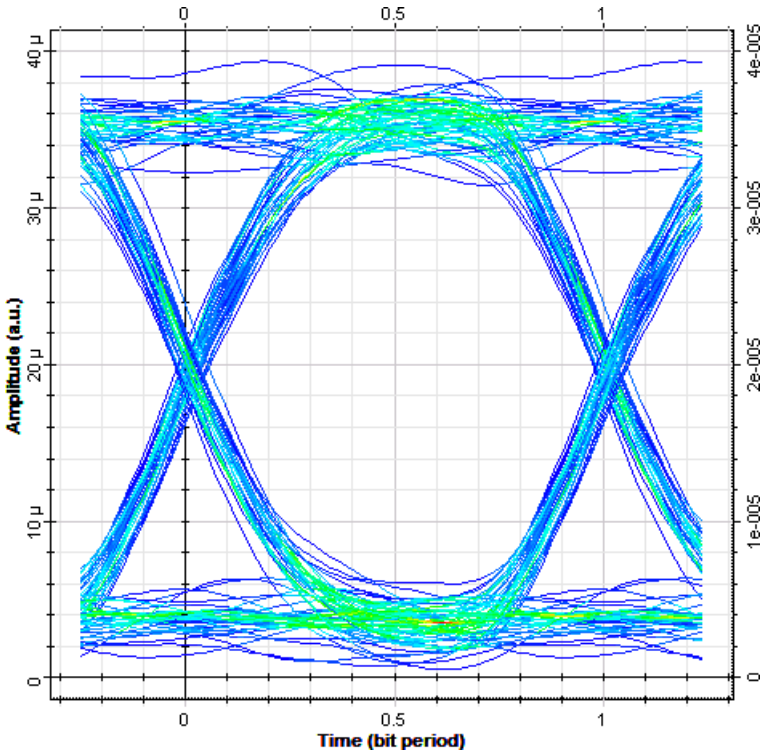

Figure 8.14: Eye diagram of fog simulation at 850 nm and 5 m - 60 minute.

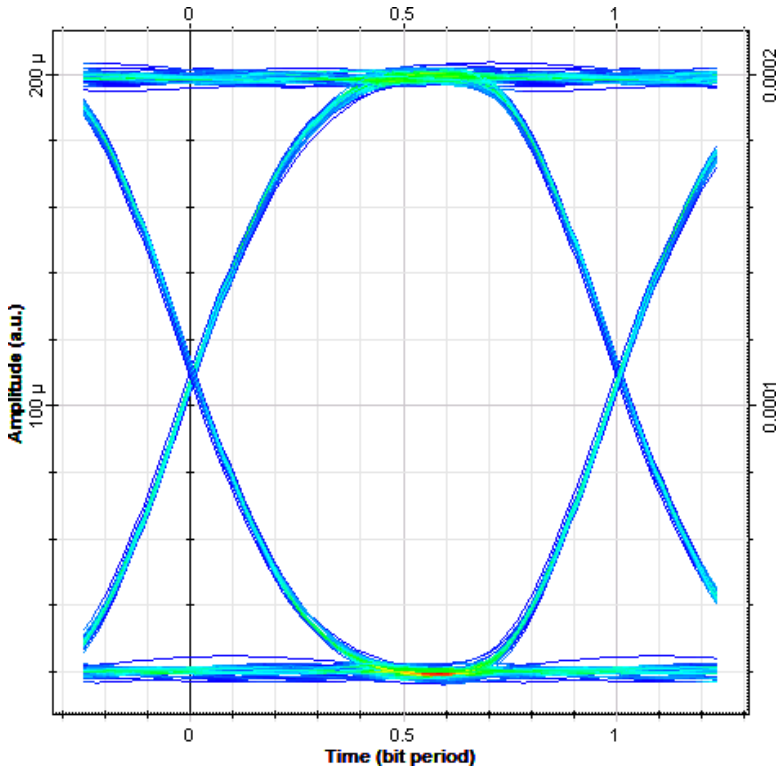

Figure 8.15: Eye diagram of fog simulation at 1550 nm and 2.5 m - 0 minute.

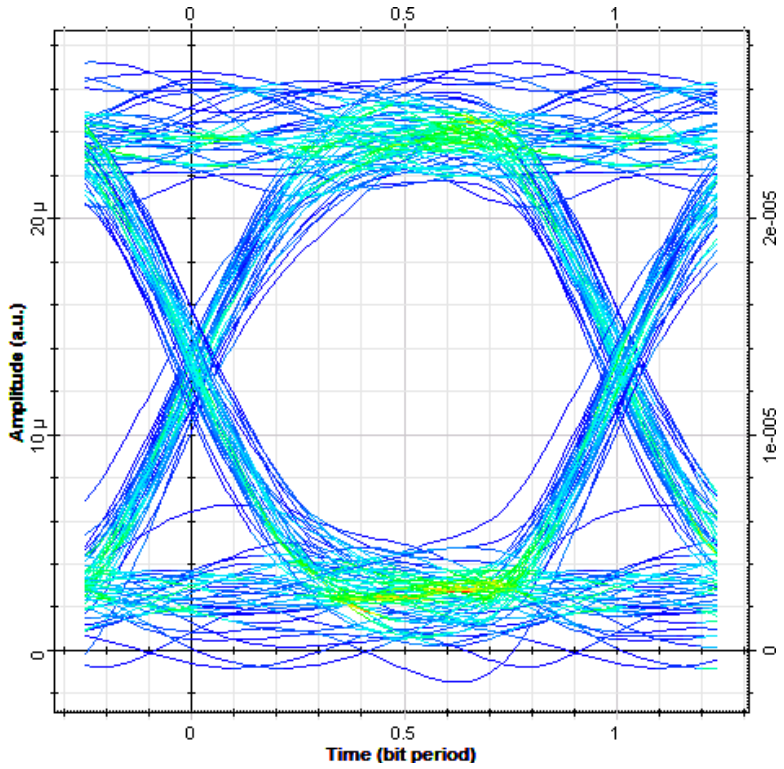

Figure 8.16: Eye diagram of fog simulation at 1550 nm and 2.5 m - 15 minute.

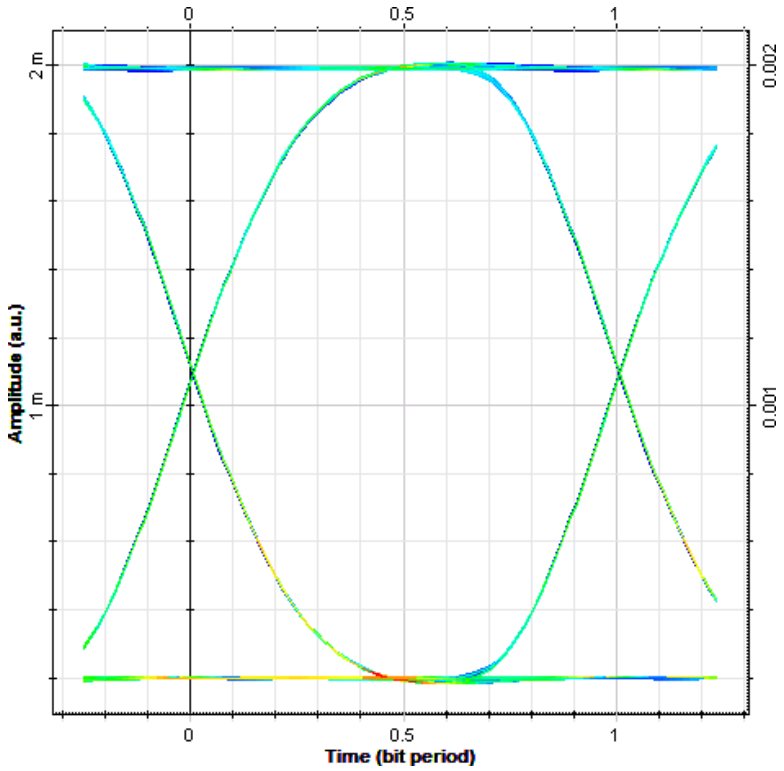

Figure 8.17: Eye diagram of fog simulation at 1550 nm and 2.5 m - 60 minute.

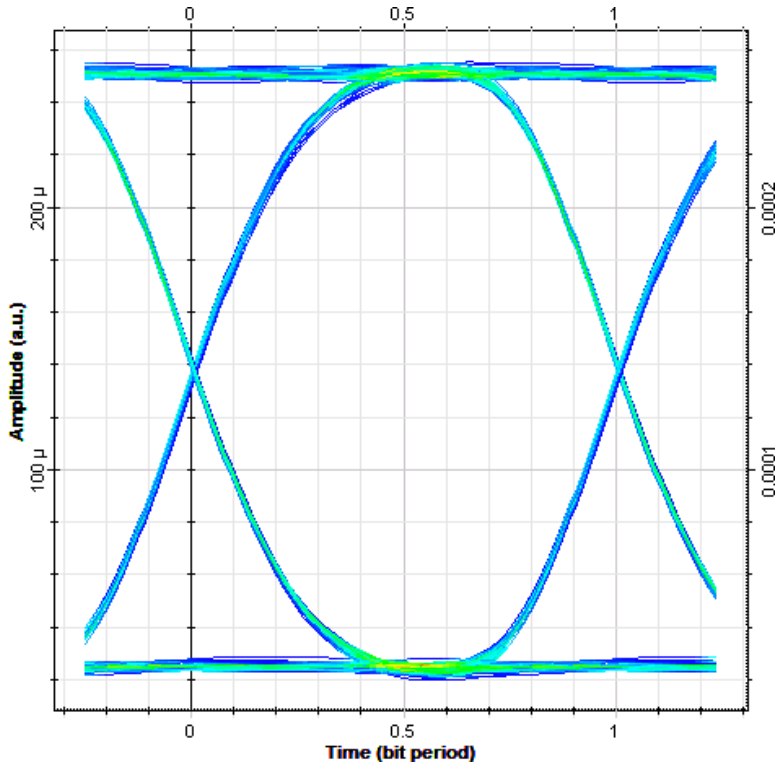

Figure 8.18: Eye diagram of fog simulation at 1550 nm and 5 m - 0 minute.

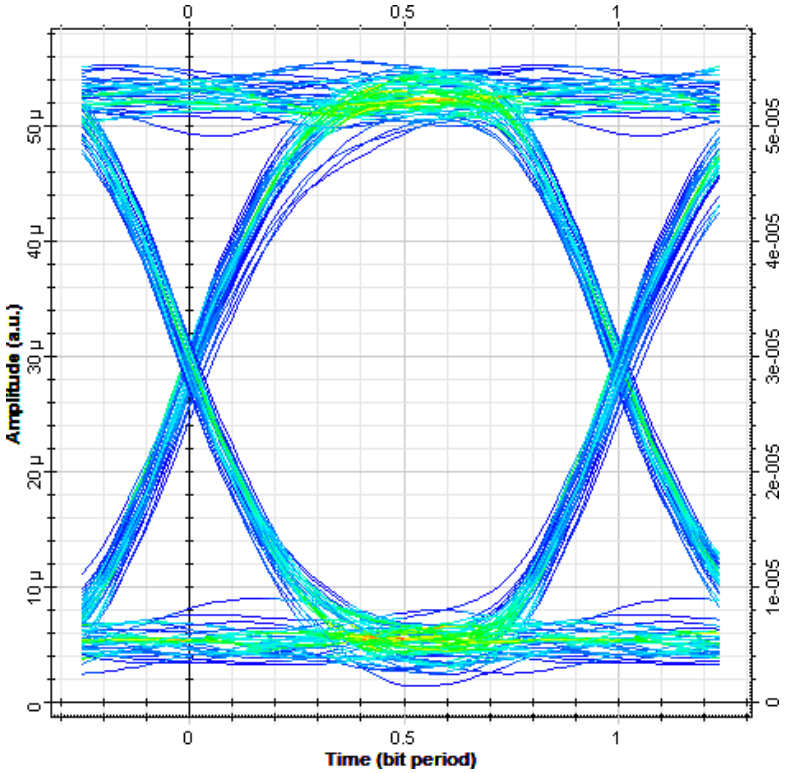

Figure 8.19: Eye diagram of fog simulation at 1550 nm and 5 m - 20 minute.

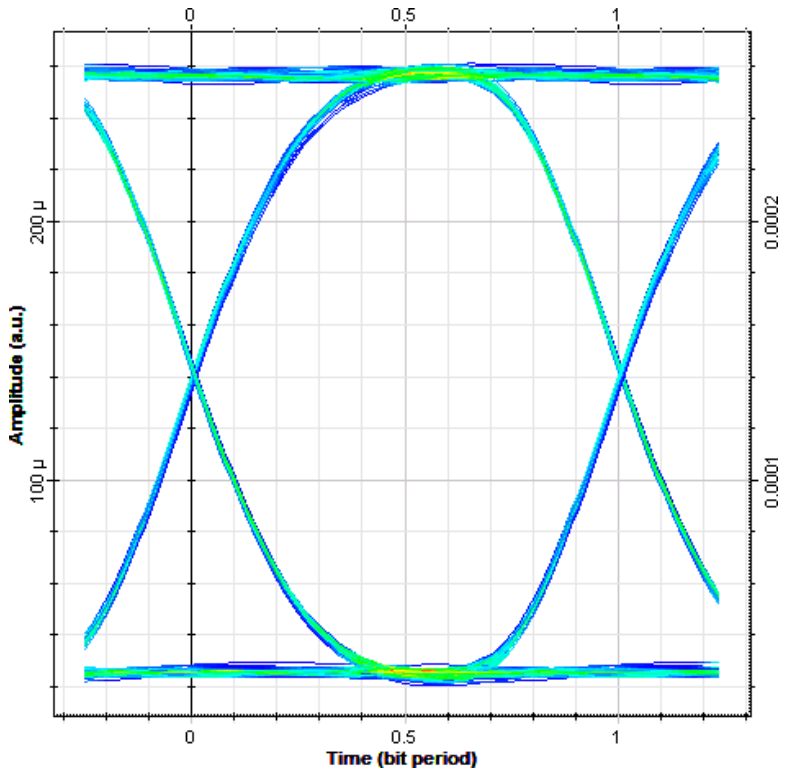

Figure 8.20: Eye diagram of fog simulation at 1550 nm and 5 m - 60 minute.

9 Conclusion

The main subject of this thesis is the free space optics link. In theoretical part of this work, I have described all the essential characteristics of the free space optics link and how particular atmospheric effects influences these links. Also these undesirable effects using practical and software simulations were described.

To perform practical simulations of atmospheric effects, experimental workplace suitable for measurements has been created. I have designed special simulation box where it was possible to simulate atmospheric conditions. This box now allows the simulation of three kinds of conditions - velocity turbulence, thermal turbulence and effects of a fog. The box is designed for measurements in two distances of influenced environment - 2.5 m and 5 m. For measurements were chosen the most widely used wavelengths 850 nm and 1550 nm. The third source was used in visible spectrum - 632.8 nm.

By practical measurements it was found that the velocity turbulence does not affect or has a very little influence on the fluctuations of optical power. In contrast of velocity turbulence the thermal turbulence is strongly influenced by the fluctuations of optical power. Additionally it was found that the effects are spectrally dependent. The largest effect of thermal turbulence was found at wavelength of 632.8 nm. At wavelength of 850 nm was the effect significantly smaller. Fluctuations of optical power at wavelength of 1550 nm were even more than two times lower than at the 632.8 nm. In case of fog effects further interesting results were obtained. Effect of fog is also spectrally dependent. The maximum attenuation caused by fog was approximately the same as at wavelengths of 632.8 nm and 850 nm but at 1550 nm was attenuation more than two times lower. The shape of curves due to fog effect is also interesting. At wavelength of 632.8 nm was strong attenuation evident within first minutes of measurement caused by mixing dense and sparse areas of fog. An effect at the wavelength of 850 nm was slightly smaller. Behavior of the laser source at wavelength of 1550 nm is quite different. Attenuation in first minutes of measurement caused by mixing areas of fog was very small. Because of this communication probably would work.

Measured data of fog effects were used in the software simulation part. The question was if the connection is able to reliably communicate in the circumstances. Analyzing BER parameter, eye diagram and Q Factor was found that links at 632.8 nm and 850 nm would work reliably in the last minutes of measurement when the fog was almost dissipated. The connection at wavelength of 1550 nm would function reliably over the entire period of measurement and at both distances. These results demonstrate that the laser source of 1550 nm (compared to 632.8 nm and 850 nm) is the most resistant source against atmospheric conditions.

In the future it would be appropriate to test more wavelengths for even better overview. It would be also possible to extend the simulated distance using mirrors. In the future works the box could be improved to simulate rain and other effects. Simulation boxes created in this work also served to other students for their thesis such as simulation of airflow and influence of the atmospheric conditions on the modulation types.

References

[1] POPOOLA, Wasiu Oyewole. *Subcarrier Intensity Modulated Free-Space Optical Communication Systems*. Newcastle, 2009. Academic Thesis. University of Northhumbria at Newcastle. Online: http://nrl.northumbria.ac.uk/1939/1/popoola.wasiu_phd.pdf.

[2] ANDREWS, Larry C. a Ronald L. PHILLIPS. *Laser Beam Propagation through Random Media*. 2nd ed. Bellingham, Wash.: SPIE Press, 2005, xxiii, 782 p. ISBN 08-194-5948-8.

[3] MAJUMDAR, Arun K. a Jennifer C. RICKLIN. *Free-space Laser Communications: Principles and Advances*. Editor Arun K Majumdar, Jennifer C Ricklin. New York: Springer, 2008, x, 417 s. ISBN 978-0-387-28652-5

[4] GARLINGTON, Tom, Joel Babbitt MAJ a George LONG. *Analysis of Free Space Optics as a Transmission Technology*. U.S. Army Information Systems Engineering Command, 2005. Online: http://www.scribd.com/doc/52063844/48702278-Analysis-of-Free-Space-Optics-as-a-Transmission-Technology-Mar05

[5] BASS, Michael. *Handbook of Optics: Atmospheric Optics, Modulators, Fiber Optics, X-Ray and Neutron Optic*. Third Edition. New York: McGraw-Hill, 2010. ISBN 978-007-1633-147.

[6] DORDOVA, Lucie a Otakar WILFERT. Comparison of Turbulent Attenuation Determined. In: *Conference on Lasers & Electro Optics & The Pacific Rim Conference on Lasers and Electro-Optics, 2009*. CLEO/PACIFIC RIM '09. IEEE: Shanghai. 2009, pp. 1-2. ISBN 978-1-4244-3829-7. DOI: 10.1109/CLEOPR.2009.5292493.

[7] GREENLER, Robert. *Rainbows, Halos, and Glories*. Cambridge: Cambridge University Press, 1980. ISBN 05-213-8865-1.

[8] WILFERT, Otakar. *Optoelektronika*. Brno University of Technology, Faculty of Electrical Engineering and Communication, Department of Radio Electronics. 2010. Online: http://bad.unas.cz/Optoelektronika_S.pdf

[9] GEBHART, M., E. LEIGEB, S. Sheikh MUHAMMAD, B. FLECKER a C. CHLESTIL. *Measurement of Light Attenuation in Dense Fog Conditions for FSO Applications*. Atmospheric Optical Modeling, Measurement, and Simulation. 2005, s. 12. DOI: 10.1117/12.614830. Online: http://dx.doi.org/10.1117/12.614830

[10] BRÁZDA, Vladimír. *Šíření optického signálu v atmosféře.* Pardubice, 2011. Diploma thesis. University of Pardubice. Supervisor: doc. Ing. Ondřej Fišer, CSc. Online: http://dspace.upce.cz/bitstream/10195/39296/1/BrazdaV_Sireni%20optickeho_OF_2011.pdf

[11] LAZARIDIS, Giorgos. *Pulse Position Modulation and Differential PPM*. PCBHeaven [online]. 2011 [cit. 2013-03-10]. Online: http://bit.ly/160Bpgv

[12] POLANSKÝ, David. *Koherence laserového svazku v turbulentní atmosféře.* Brno, 2011. Diploma thesis. Brno University of Technology, Faculty of Electrical Engineering and Communication, Department of Radio Electronics. Online: http://www.vutbr.cz/www_base/zav_prace_soubor_verejne.php?file_id=37916

[13] BÁRTA, Miroslav. *Vliv atmosférických turbulencí na optický svazek*. Brno, 2009. Diploma thesis. Brno University of Technology, Faculty of Electrical Engineering and Communication, Department of Radio Electronics. Supervisor: Ing. Lucie Dordová. Online: http://www.vutbr.cz/www_base/zav_prace_soubor_verejne.php?file_id=14957

[14] BARCÍK, Peter. *Rozložení relativní variance optické intenzity ve svazcích.* Brno, 2012. Diploma thesis. Brno University of Technology, Faculty of Electrical Engineering and Communication, Department of Radio Electronics. Supervisor: Ing. Lucie Hudcová, Ph.D. Online: http://www.vutbr.cz/www_base/zav_prace_soubor_verejne.php?file_id=51377

[15] AUBRECHT, Ondřej. *Studium profilu strukturního parametru indexu lomu v atmosféře.* Brno, 2012. Diploma thesis. Brno University of Technology, Faculty of Electrical Engineering and Communication, Department of Radio Electronics. Supervisor: Ing. Lucie Hudcová. Online: http://bit.ly/10mJCGX.

[16] FRISCH, A.S. a G.R. OCHS. A Note on the Behavior of the Temperature Structure Parameter in a Convective Layer Capped by a Marine Inversion. *Journal of Applied Meteorology*. 1975, Vol. 14, Iss. 3, pp. 415-419. ISSN 0021-8952. DOI: http://dx.doi.org/10.1175/1520-0450(1975)014<0415:ANOTBO>2.0.CO;2.

[17] MUHAMMAD, Sajid Sheikh. *Investigations in Modulation and Coding for Terrestrial Free Space Optical Links*. Graz, 2007. Dissertation. Graz University of Technology. Supervisor: Univ. Professor Dipl. Ing. Dr. Otto Koudelka.

[18] POPOOLA, Wasiu O. a Zabih GHASSEMLOOY. BPSK Subcarrier Intensity Modulated Free-Space Optical Communications in Atmospheric Turbulence. *Journal of Lightwave Technology*. 2009, pp. 967-973. Vol. 27, Iss: 8, ISSN 0733-8724. DOI:10.1109/JLT.2008.2004950.

[19] MATLAB version R2012a. Natick, Massachusetts: The MathWorks Inc., 2012.

List of Figures

List of Tables

List of Appendices

Part of this thesis is the CD with electronic appendices.

Appendix A - Additional Tables

Table A.1: Optical power on output of simulated channel in simulation of fog.

Wavelength	**632.8 nm**		**850.0 nm**		**1550.0 nm**	
Distance	**2.5 m**	**5.0 m**	**2.5 m**	**5.0 m**	**2.5 m**	**5.0 m**
Time	**Optical Power (W)**					
0 min.	$1{,}94E^{-7}$	$4{,}64E^{-8}$	$6{,}91E^{-9}$	$8{,}70E^{-9}$	$1{,}09E^{-4}$	$1{,}38E^{-4}$
5 min.	$1{,}73E^{-7}$	$4{,}13E^{-8}$	$5{,}49E^{-9}$	$9{,}76E^{-9}$	$1{,}74E^{-5}$	$6{,}91E^{-5}$
10 min.	$2{,}18E^{-7}$	$4{,}43E^{-8}$	$6{,}91E^{-9}$	$1{,}55E^{-8}$	$1{,}38E^{-5}$	$4{,}36E^{-5}$
15 min.	$6{,}13E^{-7}$	$5{,}21E^{-8}$	$1{,}09E^{-8}$	$3{,}09E^{-8}$	$1{,}32E^{-5}$	$3{,}31E^{-5}$
20 min.	$2{,}18E^{-6}$	$1{,}31E^{-7}$	$2{,}75E^{-8}$	$6{,}91E^{-8}$	$1{,}38E^{-5}$	$2{,}88E^{-5}$
25 min.	$1{,}09E^{-5}$	$2{,}61E^{-7}$	$6{,}91E^{-8}$	$1{,}38E^{-7}$	$1{,}55E^{-5}$	$2{,}95E^{-5}$
30 min.	$4{,}34E^{-5}$	$7{,}35E^{-7}$	$1{,}95E^{-7}$	$3{,}09E^{-7}$	$2{,}18E^{-5}$	$3{,}38E^{-5}$
35 min.	$1{,}09E^{-4}$	$1{,}65E^{-6}$	$4{,}36E^{-7}$	$6{,}91E^{-7}$	$4{,}39E^{-5}$	$4{,}16E^{-5}$
40 min.	$2{,}74E^{-4}$	$3{,}69E^{-6}$	$1{,}23E^{-6}$	$1{,}55E^{-6}$	$1{,}09E^{-4}$	$5{,}36E^{-5}$
45 min.	$4{,}87E^{-4}$	$8{,}25E^{-6}$	$3{,}88E^{-6}$	$3{,}09E^{-6}$	$2{,}75E^{-4}$	$5{,}61E^{-5}$
50 min.	$1{,}09E^{-3}$	$1{,}65E^{-5}$	$1{,}38E^{-5}$	$6{,}91E^{-6}$	$5{,}49E^{-4}$	$9{,}32E^{-5}$
55 min.	$1{,}94E^{-3}$	$3{,}28E^{-5}$	$7{,}75E^{-5}$	$1{,}38E^{-5}$	$8{,}30E^{-4}$	$1{,}20E^{-4}$
60 min.	$2{,}74E^{-3}$	$5{,}21E^{-5}$	$8{,}70E^{-4}$	$1{,}95E^{-5}$	$1{,}10E^{-3}$	$1{,}41E^{-4}$

Table A.2: Coefficients of regression curves used in processing of fog measurements.

Wavelength	Distance	Used polynomial model
632.8 nm	2.5 m	p_1 = -6.38e-10 (-6.495e-10, -6.265e-10) p_2 = 1.555e-07 (1.531e-07, 1.58e-07) p_3 = -1.498e-05 (-1.518e-05, -1.477e-05) p_4 = 0.000706 (0.0006974, 0.0007147) p_5 = -0.0158 (-0.016, -0.01561) p_6 = 0.1135 (0.1113, 0.1158) p_7 = -0.2179 (-0.2297, -0.2062) p_8 = 57.95 (57.93, 57.97)
632.8 nm	5.0 m	p_1 = 9.621e-09 (9.421e-09, 9.821e-09) p_2 = -1.822e-06 (-1.858e-06, -1.786e-06) p_3 = 0.0001271 (0.0001246, 0.0001296) p_4 = -0.003666 (-0.003748, -0.003583) p_5 = 0.02083 (0.01952, 0.02215) p_6 = 0.09769 (0.08864, 0.1067) p_7 = 52.5 (52.48, 52.52)
850.0 nm	2.5 m	p_1 = -1.386e-05 (-1.393e-05, -1.379e-05) p_2 = 0.001608 (0.0016, 0.001617) p_3 = -0.0701 (-0.07044, -0.06976) p_4 = 0.5669 (0.5618, 0.5719) p_5 = 55.6 (55.58, 55.62)
850.0 nm	5.0 m	p_1 = 2.187e-07 (2.149e-07, 2.224e-07) p_2 = -3.481e-05 (-3.537e-05, -3.425e-05) p_3 = 0.002132 (0.002101, 0.002162) p_4 = -0.06245 (-0.06317, -0.06172) p_5 = 0.2051 (0.1981, 0.2121) p_6 = 54.86 (54.84, 54.88)
1550.0 nm	2.5 m	p_1 = -3.386e-08 (-3.42e-08, -3.353e-08) p_2 = 6.525e-06 (6.464e-06, 6.586e-06) p_3 = -0.0004745 (-0.0004787, -0.0004703) p_4 = 0.01645 (0.01631, 0.01659) p_5 = -0.2972 (-0.2994, -0.295) p_6 = 2.715 (2.7, 2.73) p_7 = 13.76 (13.73, 13.79)
1550.0 nm	5.0 m	p_1 = 0.0001586 (0.0001575, 0.0001598) p_2 = -0.02114 (-0.02124, -0.02103) p_3 = 0.6934 (0.6907, 0.6961) p_4 = 13.06 (13.04, 13.08)

Appendix B - Selected Photos of Workplace Realization

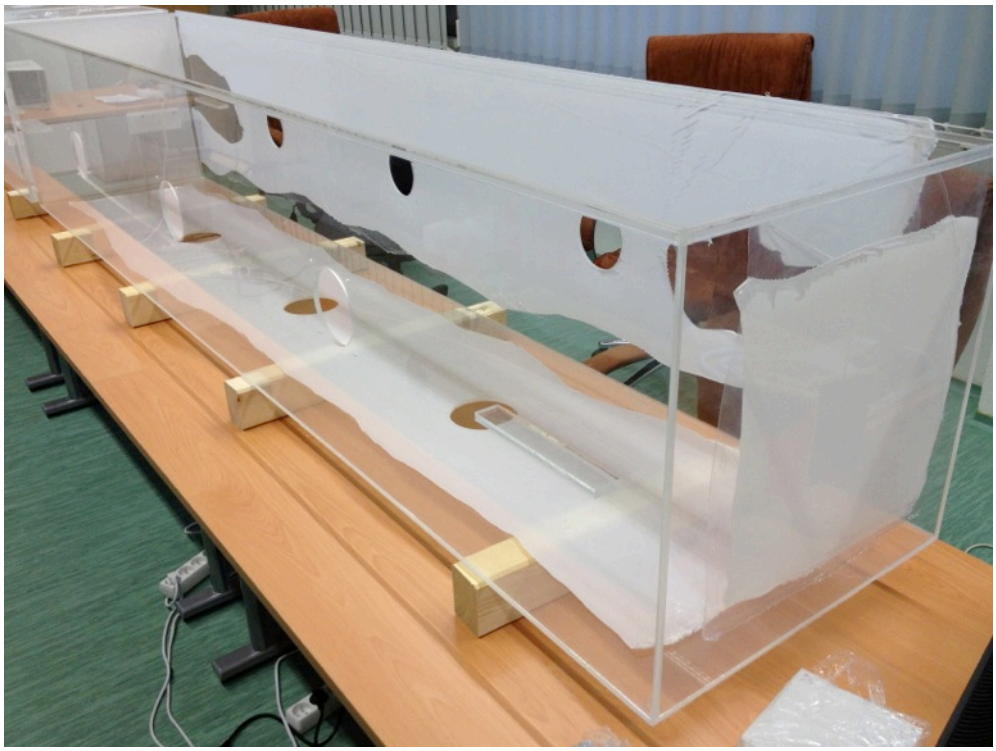

Figure B.1: Box wrapped in sheets immediately after production.

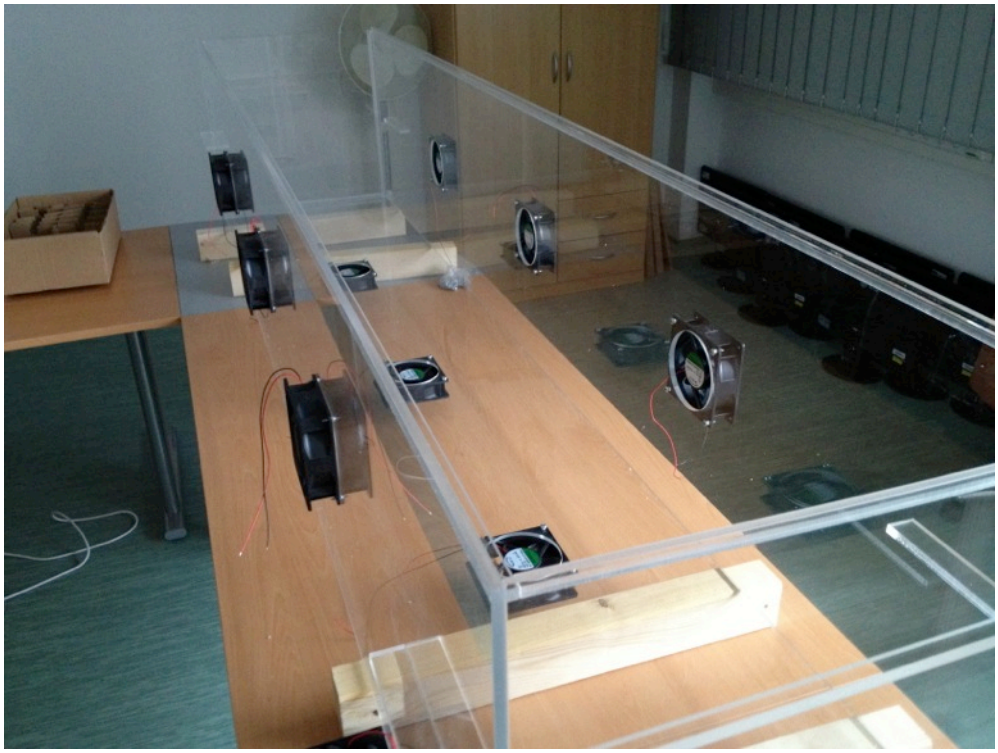

Figure B.2: Installation of fans (without the upper lid).

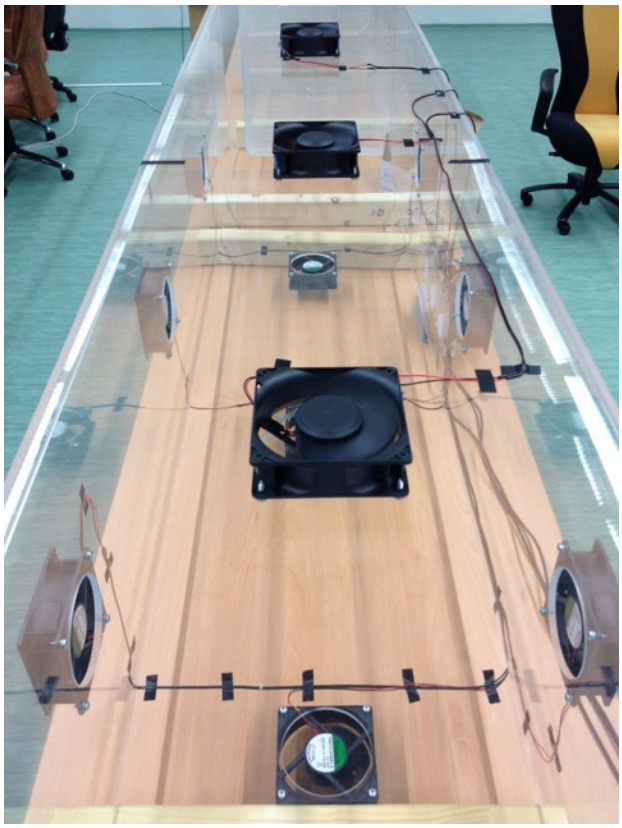

Figure B.3: Test of fans functionality.

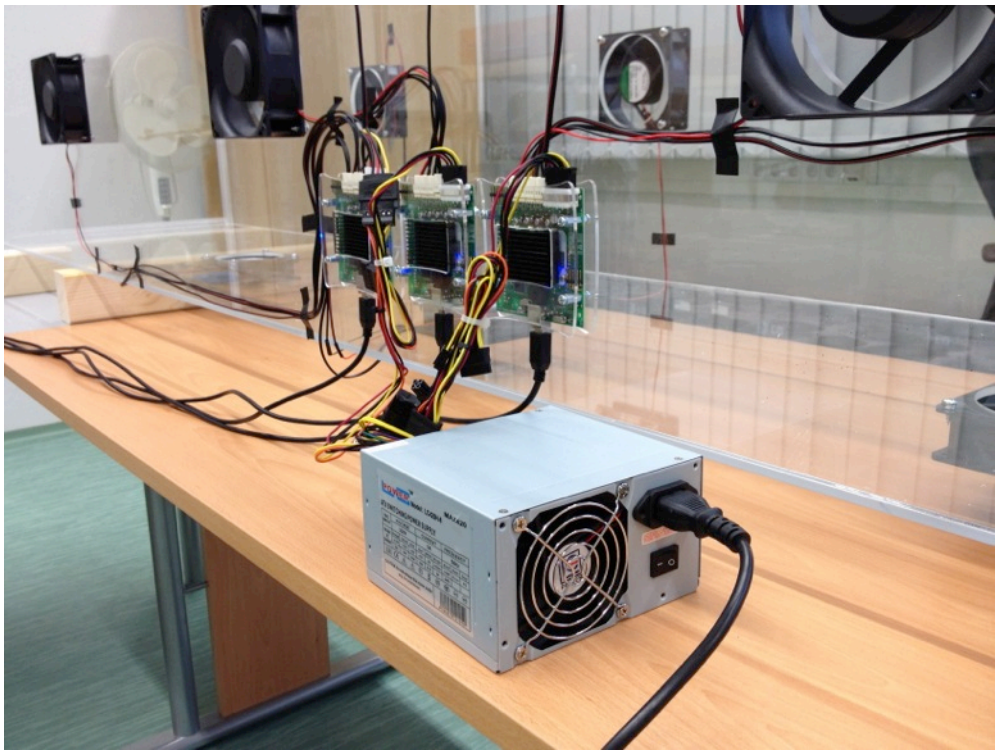

Figure B.4: Setting of fan control units.

Figure B.5: Box completely closed with caps (in the background with fans).

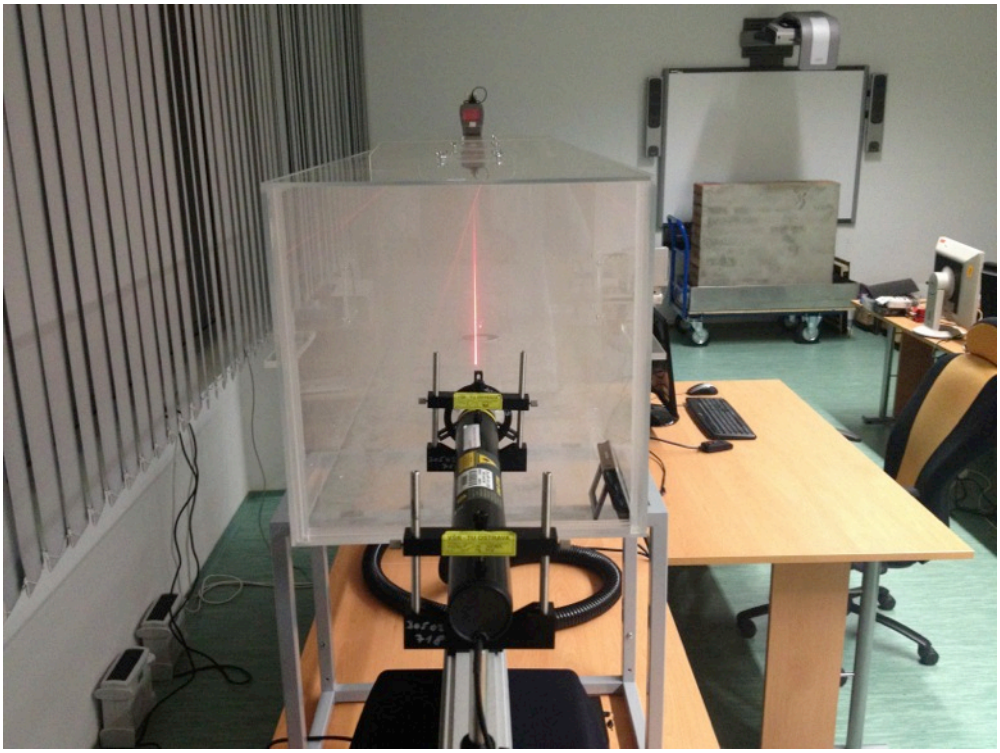

Figure B.6: Laser source at wavelength of 632.8 nm during first tests with fog.

Figure B.7: Laser source at wavelength of 632.8 nm during first tests with fog.

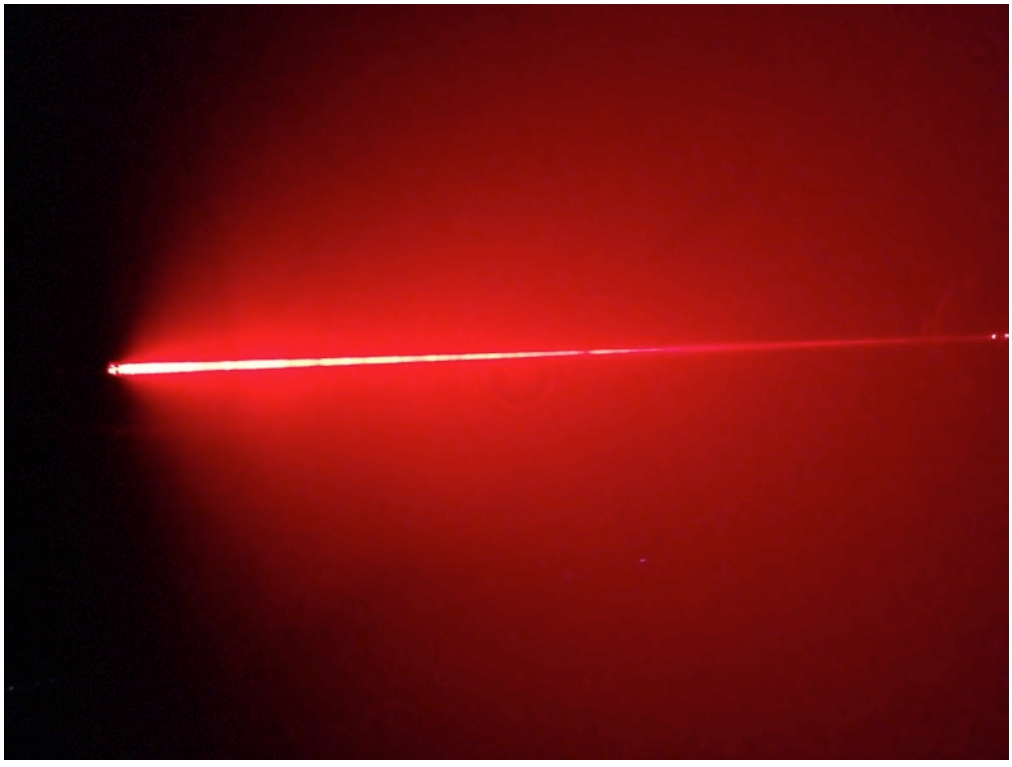

Figure B.8: Light scattering at 632.8 nm during measurement of fog.

Figure B.9: Controllers of laser diode at 850 nm.

Figure B.10: Used optical power meters (measuring at three wavelength simultaneously).

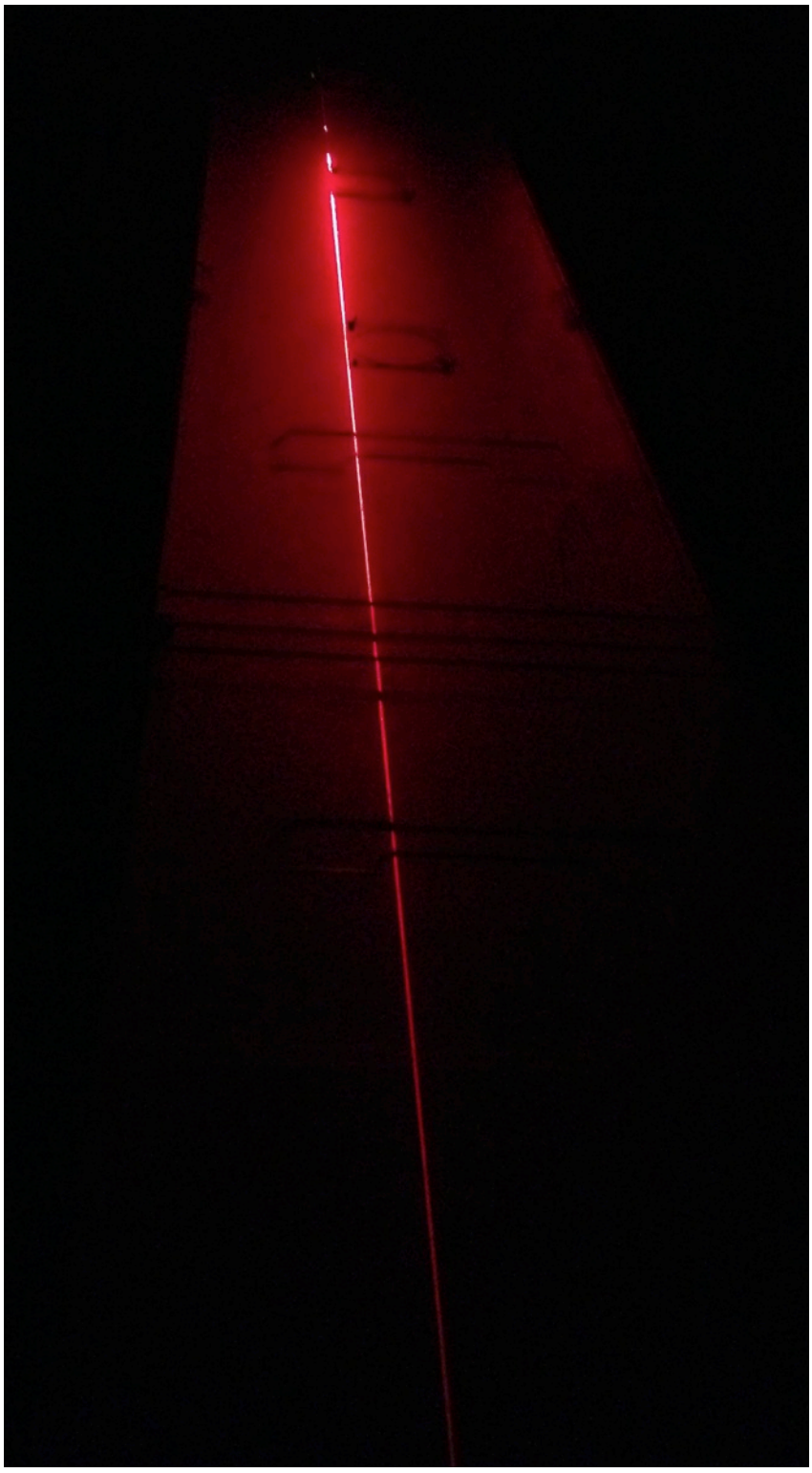

Figure B.11: Effects of fog on light at 632.8 nm during measurement.